PION PRODUCTION IN NEUTRON - PROTON COLLISIONS IN THE NEIGHBORHOOD OF 1.6 BEV/C

BY JAMES E. PARKER MICHIGAN STATE LIBRARIES

3 1293 01764 0115

This is to certify that the

thesis entitled

PION PRODUCTION IN NEUTRON-PROTON COLLISIONS IN THE NEIGHBORHOOD OF 1.67 BEV/C

presented by

James Evans Parker

has been accepted towards fulfillment of the requirements for

PhD degree in Physics

Major professor

Date Feb- 11, 1963

O-169



ABSTRACT

PION PRODUCTION IN NEUTRON-PROTON COLLISIONS IN THE NEIGHBORHOOD OF 1.6 BEV/C

by James E. Parker

A study has been made of single pion production by neutrons on protons in a hydrogen bubble chamber. The momentum spectrum of incident neutrons has a peak at 1.6 bev/c with a full width of 0.7 bev/c in the laboratory system. The angular and laboratory kinetic energy distributions of the final state nucleons show the peripheral nature of the interaction. Good agreement was obtained when the data were compared with the peripheral interaction theory of Selleri and Ferrari using a cutoff function. The effective mass distributions show the presence of the 3,3 isobar and indicate that using experimental cross-sections and angular dependence for the scattering vertex gives a slightly better agreement than using a simple Breit-Wigner resonance. Laboratory kinetic energy distributions show that a cutoff function which reduces the cross-section at high momentum transfer is necessary.

Approved: Inch Mallan

PION PRODUCTION IN NEUTRON-PROTON COLLISIONS IN THE NEIGHBORHOOD OF 1.67BEV/C

Ву

James E. Parker

A THESIS

Submitted to

Michigan State University
in partial fulfillment of the requirements

for the degree of

DOCTOR OF PHILOSOPHY

Department of Physics and Astronomy

926783

ACKNOWLEDGEMENTS

The author would like to express his gratitude to Professor J. Ballam and to J. H. Scandrett for their help and guidance during the experimental work and during the writing of the thesis; to Drs. R. K. Adair, L. B. Leipuner, W. Chinowsky, and other members of the bubble chamber group for the use of the chamber and the genereous loan of their film; to Dr. G. B. Collins and the members of the Cosmotron staff for the operation of the accelerator; to Robert Lawrence, Jennifer Lee, and Nancy Sweet and others for assistance in scanning and measuring the film and drawing many of the figures; to Drs. G. Kalbfleish and M. Horowitz for giving him copies of the ATHOS program; to Leonard Harding for handling the computational material at the University of Michigan; and to Dr. F. Selleri for his comments and suggestions with regard to the theoretical curves. He would especially like to express his thanks to the National Science Foundation for financial support of the work.

TABLE OF CONTENTS

Abstract	i
Acknowledgements	ii
I. Introduction	1
II. Description of the experiment	6
III. Measurement and selection of events	ç
IV. Results and interpretation	
A. The pp π^- events	16
B. The four body events	22
V. Figures	24
VI. Appendix: description of programs	
A. Track fitting program	112
B. Kinematic testing program	118
C. The peripheral model program	120
References	127

LIST OF FIGURES

1.	Diagrams representing pion production in nucleon-nucleon	
	collisions.	24
2.	Beam design.	25
3.	Typical picture.	26
4.	Neutron beam direction cosines.	2
5.	- 8. Standard deviation of circle fit.	28
9.	Measurement of back fiducial mark.	32
10.	Momentum spectrum of $oldsymbol{\pi}^{oldsymbol{-}}$ beam particles.	32
11.	Momentum spectrum of .45 bev kinetic energy positive pions.	34
12.	Momentum spectrum of .60 bev kinetic energy positive pions.	35
13.	- 22. Initial Q value.	36
23.	Fractional change in momentum made by QEVAL.	46
24.	Neutron lab momentum of pp $oldsymbol{\pi}^{oldsymbol{-}}$ events.	4
25.	Neutron center of mass momentum of $pp\pi^-$ events.	48
26.	Scatter plot of Y and Z direction cosines of the beam particle	
	of apparent pp $m{\pi}$ events whose adjusted beam angle was greater	
	than 5°.	2,9
27.	- 31. Proton center of mass momentum.	50
32.	-36. Proton lab kinetic energy.	5
37.	- 41. Proton center of mass angular distribution.	60
42.	- 46. M* of p π^- combinations.	6.
47.	- 51. Angular distribution of pion in M* system.	70
52.	- 56. Pion lab kinetic energy.	7
57.	- 61. Pion center of mass momentum.	80
62.	- 66. Pion center of mass angular distribution.	8
67.	Elastic and charge exchange scattering cross-section for	
	π p scattering as a function of the invariant mass of the pair	•90
68.	Peripheral diagrams for the pp $m{\pi}^-$ events.	9:
69.	Contributions to the kinetic energy spectrum.	92
70.	Comparison of cross-section of the reactions n+p \rightarrow p+p+ π	
	and $p+p \rightarrow p+p+\pi^0$ at .97 bev.	9.
71.	Comparison of ${\rm M}^{\hskip-1.5pt \star}$ spectrum from peripheral model and from phase	
	space with resonance.	9.
72.	Incident lab momentum of pn $\pi^+\pi^-$ events.	9:
73.	- 75. Nucleon lab momentum.	96
76.	- 78. Nucleon center of mass angular distribution.	99

79.	- 84. M*	of nucleon-pion combinations.	102
85.	- 87. M*	of pion-pion combination.	108
88.	Incident	lab neutron momentum of pp $ar{\pi}ar{\pi}^{\circ}$ events.	111
A1.	Geometry	for finding points in the chamber from measured	
	points.		116
A2.	Geometry	of the circle fitting proceedure.	117

I. INTRODUCTION

Although much work has been done on pion production in p-p interactions (1-7), not much has been done with n-p interactions except those involving incident protons on neutrons in complex nuclei. Probably the greatest reason for this is the inherent difficulties in working with a neutral beam of particles. Those experiments which have dealt with incident neutrons on protons (8-10) have resulted in few events and the energies of the incident neutrons of these events were spread over a rather wide range. Hence the detailed analysis of momentum and angular distributions of the final particles at a given energy were statistically inconclusive. In this experiment we have obtained a larger number of events and are able to sub-divide the events into slices of incident energy and still maintain statistical significance.

The earliest theory dealing quantitatively with pion production is the statistical model due to Fermi. (11) In this model he considers that since the interaction is so strong the incident particles come together inside an interaction volume and quickly attain a sort of thermodynamic equilibrium between the various possible final states. Such final states are limited by the conservation rules such as conservation of energy, momentum, charge, baryons, etc. The system then proceeds into one of the possible outgoing channels with a probability proportional to the available volume in phase space. Branching ratios of the possible final states are predicted as well as the spectra of the variables characterizing the final particles. Put another way, the model assumes that the matrix element coupling initial and final states for a given reaction is constant. This theory is called the statistical model and the spectra of variables predicted by it are referred to as "phase space" curves.

As early experimental information was obtained it became apparent that the statistical model as it stood was an oversimplification. Irregularities in the momentum and energy spectra of final particles were observed which were not predicted. Even the multiplications of final state particles were not accurately predicted. It became apparent that final state interactions must taken into account.

In the early and middle 1950's there was considerable effort to incorporate the effects of final state interactions into the theory starting with the work of Watson (12). The assumptions generally made in this early theory were that the final state forces play no important role in the primary interaction which causes the interaction between the incident particles, but the reaction is then distorted by the short range forces between the final particles before they leave the region of their mutual interaction. Introducing into the theory the principles of conservation of isotopic spin and of parity and applying the rules of conservation of angular momentum and of the Pauli Principle placed severe restrictions on the final states allowed. The effects of the known forces between nucleons and the very strong T = 3/2, J = 3/2 resonance between pion and nucleon were introduced into the theory and the result was to effectively distort the phase space available to final particles. Reviews of the development and application of this early theory are contained in articles by Rosenfeld and by Gell Mann and Watson (13).

The development of theory in this manner finally led to the "isobar" model of Lindenbaum and Sternheimer (14). In this theory the interaction is assumed to proceed as a two step process: the formation of one or two isobars followed by the subsequent decay of the isobar into pion and nucleon. See figure 1a. Hence they use a two body phase space factor multiplied by the cross-section for formation of the isobar and a factor determined by the kinematics of the decay of the isobar. The isobar predominately responsible for pion production at moderately low energies (< 1.5 bev) is the isobar with effective mass 1.237 bev corresponding to the 3/2.3/2 resonance in pion-nucleon scattering. The angular distribution of isobar formation was considered in two cases: isotropic and only forward and backward in the center of mass system. The pions were assumed to be emitted isotropically in the isobar center of mass system. As better resolution along with additional data at higher energies were obtained, two additional resonances were observed in the T = 1/2 state in pion-nucleon scattering. These resonances at about 600 mev and 880 mev are not as strong and are at a much higher energy than the 3/2 resonance at about 190 mev. The effects of these higher resonances have been incorporated into the isobar model, and in an attempt to account for multiple pion production it is assumed that the higher isobars can decay into one of the lower isobars by emitting a pion as well as by decaying directly to pion and nucleon. The model has been extended to include pion-nucleon interactions as well. Discussion of the application of the isobar model is contained in many articles of the past few years. (15) In particular a fairly extensive bibliography of recent work is contained in Fickinger, et al of this reference.

Although the isobar model has been fairly successful in predicting some of the features of pion production; certain of the features, such as strong forward-backward peaking of the nucleons and a strong tendency toward small momentum transfer to the nucleons, (5-7,16,17) suggests a more direct interaction model, namely the peripheral model. Several authors have written theoretical papers or discussed experimental results in connection with such a peripheral model. (18-24) The work of Selleri in collaboration with several people (25) is of particular interest. model which he proposes is a direct interaction model in that in the inelastic scattering of any particle by a nucleon, the process is dominated by the exchange of a single virtual particle from the cloud of the nucleon and the scattering of the incident particle by this virtual particle. See figure 1b. We are interested here in pion production in n-p interactions where the exchanged particle is a pion, although other processes may be treated as well. The symbols labeling the diagram in figure 1b will be used to represent the 4-momentum of the particles, but when the energy component is used explicitly an additional zero subscript indicates energy and the symbol in the diagram represents the 3-momentum. In terms of the S matrix Selleri writes:

 $S_{fi} \sim \langle q_2 | j(0) | p_2 \rangle \Delta_F (\Delta^2) \langle q_3 q_1 | j(0) | p_1 \rangle$ where the operator j(0) is the current operator for the virtual particle defined by the equation of its field $\Phi(x)$: $(P_1 P_2) \Phi(x) = i(x)$ and

defined by the equation of its field $\phi(x)$: $(\square - \mu^2) \phi(x) = j(x)$, and Δ_F' is its propagation function. The vertex function $\langle q_2 | j(0) | p_2 \rangle$ is a function only of the 4-momentum transfer; $\Delta^2 = (p_2 - q_2)^2$, and represents the emission of the pion from the lower vertex. The vertex function $\langle q_3 q_1 | j(0) | p_1 \rangle$ is proportional to the analytic continuation of the matrix element for the process $k+p_1 \rightarrow q_3+q_1$, and represents the interaction between the incident particle and the virtual particle at the upper vertex.

In more explicit terms Selleri has developed from the theory the general partial cross-section:

$$d\sigma = \frac{G^{2}}{(2\pi)^{2}F} \frac{\Delta^{2} + (m_{2} - M_{2})^{2}}{(\Delta^{2} + \mu^{2})^{2}} K^{2}(\Delta^{2}) K^{2}(\Delta^{2}) \omega^{4} \frac{p_{i}^{Q}}{g_{3}^{Q}} \frac{d\sigma_{i}}{d\Omega} (\omega, \cos\theta_{i}^{Q}, \Delta^{2}).$$

$$\cdot \delta^{4} (P_{f} - P_{i}) \frac{d_{g_{i}}^{3} d_{g_{2}}^{3} d_{g_{3}}^{3}}{g_{10} g_{20} g_{30}},$$

where G^2 is a coupling constant, $F = \left\{ (p_1 \cdot p_2)^2 - M_1^2 M_2^2 \right\}^2$, ω is the invariant mass of particles q_1 and q_3 , the superscript Q implies evaluation in the q_1,q_3 center of mass system, and $\frac{d\sigma_1}{d\Omega}$ is the differential cross-section for the process $k+p_1 \rightarrow q_3+q_1$. The factors K and K' are the form factors for the lower vertex and of the propagator defined so that $K(-\mu^2) = K'(-\mu^2) = 1$. This is a rigorous formula but cannot be applied without the dependence upon Δ^2 of the form factor terms K and K' and the partial cross-section term $\frac{d\sigma_1}{d\Omega}$. The approximation valid for small Δ^2 (pole approximation) consists of putting in $\Delta^2 = -\mu^2$ in K and K' and in $\frac{d\sigma_1}{d\Omega}$. In $\frac{d\sigma_2}{d\Omega}$ the Δ^2 dependence enters practically only through the angle. The expression then reduces to:

$$d\sigma = \frac{G^{2}}{(2\pi)^{2}F} \frac{\Delta^{2} + (m_{2} - M_{2})^{2}}{(\Delta^{2} + \mu^{2})^{2}} \omega^{2} \frac{k_{i}^{Q}}{g_{3}^{Q}} \frac{d\sigma_{i}}{d\Omega} (\omega, \cos \theta_{i}^{Q}).$$

$$\cdot \delta^{4} (P_{f} - P_{i}) \frac{d^{3}g_{i}}{g_{10}} \frac{d^{3}g_{2}}{g_{20}} \frac{k_{3}^{Q}}{g_{3}}.$$

In the simplest application the pole approximation is used. Several comparisons of the predictions of this theory with experiment have been made ⁽²⁶⁾ and the results have been remarkably good. The more general theory not limited to small momentum transfer has been applied by Ferrari and Selleri and indications are that the one pion exchange model is valid at large momentum transfers. They have also attempted to extract a tentative behavior of the pionic form factor. See the second reference in (20).

A further advantage to the theory of Selleri is that it predicts absolute cross-sections. In other theories there are adjustable parameters such as the interaction volume in the statistical model and the isobar model. In the isobar model there are other parameters which have to be fixed from phenomenological arguments, such as the angular dependence of isobar production and the probabilities of formation and decay of the higher isobars. In the Selleri theory the partial cross-section entering into the upper vertex can be measured by other means in the case of N-N interactions. The model is also based on a very descriptive picture of the interaction.

Until now only the p-p experiments have been compared with this theory. The n-p experiments have resulted in too little data to be able to subdivide the events into small slices of incident energy and still maintain statistical significance. There are enough data in this experiment to allow such subdivision. We have been able to break the bulk of our data into 50 mev/c slices of incident center of mass momentum and still have over 200 events in each slice.

• The second second

.

II. DESCRIPTION OF THE EXPERIMENT

The experimental design has been described by Adair (26) but will be sketched here also. See figure 2. The external proton beam of the Cosmotron was brought to a focus by three 8" x 32" quadrupole magnets and then refocussed by two 12" x 40" quadrupoles onto a steel target (pion target). Negative pions at about 40 from the proton beam were focussed by a series of quadrupoles and bending magnets onto a polyethylene target (theta target). The beam was originally set up to investigate K_2^0 interactions and decays. At the theta target interactions such as π^- + (n or p) \longrightarrow (Λ° or Σ) + K° + pions give some neutral K's going toward the chamber. The K's produced at about 6° from the pion beam reached the chamber located at ten feet from the theta target. At this distance practically all of the K_1^0 part of the K⁰'s has decayed out of the beam leaving K₂⁰'s. Inherent in a neutral beam of this sort is a rather large background of neutrons as can be seen from the large number of proton recoils in a typical picture. See figure 3. These neutrons are produced by the pion beam in the theta target principally by pi-nucleon elastic and inelastic collisions. The neutrons produced will have a spread in momentum due to the spread in pion momentum and the Fermi momentum of the target nucleons as well as from the inelastic scatters.

Average external protons were about $7x10^9$ per pulse giving about $2.5x10^5$ pions at 1.6 bev/c \pm 7 percent on an area of about 50 cm² at the theta target. From the number of decays of K_2^0 into 3 pions Adair (26,27) estimates the number of K_2^0 's in the chamber to be about 1.5 per pulse. The target is located in the entrance of a large sweeping magnet to divert charged particles from the chamber and about 40 gm/cm² of lead were placed behind the theta target to convert gamma rays and sweep out the resulting showers.

The types of events to be expected from the K_2^0 interactions are as follows:

$$\overline{K}^{O} + p \rightarrow \Lambda + (1,2)\pi$$

$$\rightarrow \Sigma + (1,2)\pi$$

$$\rightarrow K^{-} + p + \pi^{+}$$

$$K^{O} + p \rightarrow K^{+} + p + \pi^{-}$$

$$K^{O} + p \rightarrow K^{O} + p$$

•

From the neutrons in the beam one would expect to see interactions of the type:

$$n + p \rightarrow n + n + pions$$

 $\rightarrow n + p + pions$
 $\rightarrow p + p + pions$.

Of these types those with only one charged track cannot be analyzed. Since no five pronged events $(pp\pi^+\pi^-\pi^-)$ were observed in the scanning, it is assumed that very few if any of the three pronged events were three pion production. This leaves us with the reactions:

$$n + p \rightarrow p + p + \pi^{-}$$

$$\rightarrow p + p + \pi^{-} + \pi^{0}$$

$$\rightarrow p + n + \pi^{+} + \pi^{0}$$

All of these types will be three pronged stars in the bubble chamber.

The detector was Adair's 14 inch hydrogen bubble chamber which has a depth of 8 inches. There are two fiducial marks on the inside surface of the front window 10 inches apart and in line with the beam direction. Also there is one such mark in the center of the inside surface of the back window. The chamber was viewed by three cameras equally spaced around a circle of 13 inches diameter 36.5 inches from the front window. The demagnification of the camera system was about 11. The chamber was illuminated by a flash tube at the opposite end of the apparatus and the light was condensed by a large lens behind the rear window to a point in the plane of the cameras so that only scattered light reached the cameras. Thus the tracks are seen as bright tracks on a dark field. The chamber was in a magnetic field of 17.5 kilogauss. Magnetic measurements of the field without the chamber in place were made, and the shape of the field was fitted by the function:

$$B = B_0 + B_z(z-z_0)^2 - B_r(r-r_0)^2$$

where $B_0 = 17.5$, $B_Z = 0.0062319$, and $B_r = 0.0035486$. z_0 and r_0 are the geometrical center of the bubble chamber.

About 39000 pictures were scanned for three pronged stars whose vertices were within a fiducial region of the chamber. The fiducial region was chosen to exclude the edges of the chamber so that events with short tracks which leave the illuminated region of the chamber would not bias the results. A track may also be short because it stops in the chamber. All events that originated within this volume were measured and accounted for. Events that proved to originate

And the second of the second o

within two centimeters of either window were discarded. In the pictures there are a large number of obvious p-p elastic scatters and some π -p scatters. These events could be interpreted as a three pronged event with the negative track going backwards in the lab. In general p-p scatters can be recognized by three heavily ionized tracks and a 90° opening angle in the outgoing state. If there was any doubt that the event was such a scatter it was measured and interpreted anyhow. Such scattering events are easily distinguished after the measurement has been done by the existence of a fairly large momentum going backwards in the lab.

TIT, MEASUREMENT AND SELECTION OF EVENTS

When the film was scanned events were sketched on a special sheet and track numbers were assigned to the three tracks. A note was made if the track either stopped in the chamber or left the front or back window. The film and picture number of the event was also noted on the sheet. Events were then measured on a Hydel film reader, which is a digitized projector. In this machine the film is held flat under vacuum on a glass plate mounted in a heavy base upon which is mounted a Gaertner stage. The stage carries the projector lenses and three small projectors (one for each view) which superimpose a light reticle on the picture. The lead screws of the stage are coupled to Datex digitizers which ultimately cause an I.B.M. card punch to record the measurement. By turning cranks under the viewing screen one can position the stage so that the reticle is superimposed over the point to be measured. The least significant digit of the digitizers represents one micron on the film and the over-all measurement accuracy of the stage is about two microns.

The events were measured in each of the three views. For each view the front fiducial marks were measured on a separate card. Then each track was measured at five roughly equally spaced points starting with the vertex of the event and ending with the end of the track. In certain circumstances however the measurement did not extend to the end of the track. If a track stopped in the chamber its momentum changed appreciably over the length of the track. By measuring many such stopping tracks we found that if about half the range of the track were measured the calculated value of momentum agreed quite well with the range-momentum curves. Thus for stopping tracks we measured only the first half of the track; the whole track was then measured as an extra track in order to measure the range.

It was found that for long tracks with appreciable curvature the error function from the fitting procedure was excessive. This error function represents the scatter of the measured points from the fitted circle. This is caused by the fact that such tracks may be slowing down somewhat over their range and by the fact that the magnetic field is not constant throughout the chamber. We found that by limiting the sagitta of such tracks we were able to improve this situation and still maintain a good measure of momentum. These tracks

were then remeasured in order to measure the visible range.

A final reason for treating tracks in a special manner came from tracks that were too short to give accurate measurements. In order for this not to introduce bias, we measured tracks in the normal fashion if the total range as seen on the viewing screen was larger than a fixed amount. If the track was shorter than that amount it was measured backwards. The reason for this lies in the manner in which first and last points are treated by the computer program. By measuring the track backwards a good measurement was obtained of the endpoint so that the range and angles could be calculated by hand. Most of these events turned out to originate within two centimeters of one of the windows and hence the event was discarded. Most of the events remaining in this category had short stopping tracks and hence the momentum could be read from the range-momentum curves.

After measurement the data was reduced by a computer program written by us for the I.B.M. 709 at the University of Michigan Computing Center. (28) This program fitted the measured points for each track to the best helix in the chamber by a least squares method using data from all three views simultaneously. An error function was derived from the scatter of the measured points from the fitted circle. Angles were computed in a straightforward fashion and momentum was calculated from the radius of the helix and the average magnetic field along the track.

After the helix fitting takes place the program proceeds to attempt a kinematic fit of the event to the possible interpretations having three particles in the final state. The procedure used by this program is to adjust the measured momenta in order to balance energy in such a manner that an error function, (the sum of the squared deviations of the momenta from their original values measured in terms of the probable error in momentum), was minimized. This function was called "chisquare". If this chisquare was not too large and the energy equation was made to balance within one mev, the computer continued with the interpretation and computed center of mass momentum values for the event. If chisquare got too large before the energy equation could be balanced, the interpretation was

deemed incorrect. Up to five iterations of the momentum adjustment were allowed although one was in general enough to either cause chisquare to be too large or to balance energy.

In the case of the four body final state interpretations with an outgoing neutral particle, a special program was written to calculate the momentum of this neutral particle using the equations of energy and momentum balance. In this case less information is available and it is necessary to assume that the beam direction is fixed.

After the results of the track fitting were back from the computer, the film was then rescanned with the computer information at hand. Using the measured values of momenta and the appearance of the tracks of the film, a judgement of the relative ionization of the tracks was made to attempt to determine the identification of the particles. Due to the quality of the pictures the range of ionization was limited so that most of the time one could say only that a track was or was not a pion. Usually this was enough information along with the results of the kinematic test to confidently identify the event as one of the several types. There still remained some events that could not be so identified and several tests were made to help in pinning these down.

In order to determine the source of the incident neutrons we made a scatter plot of the apparent beam direction as measured by the program for good $pp\pi$ events. The program calculates the direction cosines of the beam particle directly from the vector sum of the outgoing particle momenta. The events chosen in this plot were those which fit the pp \overline{n} criteria of kinematics and ionization regardless of beam angle. Figure 4 shows this scatter plot for the region near zero angle. No accumulation of points was observed at any position except as shown which is the direction of the theta target. One might expect the possibility of some neutrons coming through the shielding directly from the pion target but no evidence of this was seen. Using this information we required that the beam particle be within 5° of the x-axis to be acceptable. This criterion may exclude some pp \overline{n} events but should not introduce bias into the resulting sample. Although the geometry implies a beam spread of about 30. 50 was chosen to allow for some random measuring error.

In order to determine the over-all accuracy of the measuring and fitting procedure we studied the variable which I shall call here sig. On the computer pages this is called "standard deviation of circle fit". It is obtained from the scatter of measured points from the fitted circle. We made a histogram of sig for all tracks regardless of other variables (See figure 5.) and separate histograms for tracks of different ranges (See figures 6 - 8.). We found that sig typically was in the neighborhood of 0.01 cm and its spread varied slightly with range. In order to reduce measurement errors we put an upper limit on sig of 0.03 cm, and if it was larger than that amount the track was remeasured. Except in a few cases we were always able to get a satisfactory measurement. In those cases where we failed we could ascribe the difficulty to poor tracks or an unfortunate overlay of some background track or to a slight track deflection. For a track with a sagitta of 0.5 cm and a sig of 0.01 cm one would find a 2 percent probable error in momentum. One can see that for relatively short stiff tracks the relative error in momentum would be larger.

As an internal check of the measuring and calculation procedure we made 200 measurements of the three fiducial marks and calculated the position of the back fiducial mark and the position where a ray going from the back mark would pierce the front window. See figure 9. Of particular interest is the z-coordinate of the back fiducial mark. This measurement gives an average measurement of 20.324 cm where the 8 inch depth is 20.320 cm. The half width of the distribution of about 0.025 cm which agrees with the estimated uncertainty of measurement in the z direction. The corresponding uncertainty in the x and y measurement is about one fifth that of the z measurement or 0.005 cm.

To check the measurement and calculation of momentum directly we made measurements of some beam tracks of charged particles. We measured some negative pion pictures kindly loaned to us by Walker (29) and some positive pions loaned by H. J. Martin and E. D. Alyea of Indiana. Negative pions were at 1.89 bev/c as quoted by Walker and our measurement was 1.925 bev/c or about 1.8 percent high. See figure 10. The spread in the measurement was about that quoted by Walker. This momentum value is quite high and the tracks are quite stiff. The positive pions from Indiana were at 0.6 bev/c and 0.725 bev/c and the results of the measurement are shown in figures 11 and 12 and agree quite well with

.

ξ

the known values.

The kinematic test program is supposed to balance energy and momentum at the same time for the possible mass assignments. Now if one were starting with perfect values of the momenta and angles there would be one and only one satisfactory choice of masses, namely the correct ones. However, since we do not have in each event perfect values, the program adjusts the values of momentum in the best way to balance energy for each mass assignment in turn. One might ask just how sensitive the problem is to discrimination between the various assignments. In order to get some feeling for this we plotted the initial Q values for each mass assignment for those events which were identified as good pp π^- events. The Q value here is defined as the total incident energy in the lab minus the total outgoing energy. In other words these Q values are for the initial values of momentum before any adjustment. See figures 13 - 17. We see that for the correct identification (figure 13) the distribution centers about 5 mev with a spread of about 17.5 mev on either side. The displacement from zero of 5 mev represents our total systematic error. The Q distributions for the $pK^{T}\pi^{T}$ identifications are shown in figures 14 and 15. These are spread out over much larger values and shifted to higher Q values. No negative values were found in the sample taken. One can see that there is only a small overlap of these curves over the similar curve for the pp π^- identification. The similar curves for the pK $^ \pi^$ identifications (figures 16 and 17) show that the distribution is again very wide but covers the zero region and overlaps the $pp\pi^-$ curve entirely. Fortunately this identification can generally be ruled out from track ionization since there must be a positive pion and the negative track must not be a pion. The important point of these curves is that in all cases the wrong identification gives a Q value generally far from zero. Similar distributions were made for those events which were identified as pn $\pi^{\dagger}\pi^{-}$. See figures 18 - 22. Here we see again that the Q values for the 3-body identifications are spread out over a wide range although they overlap the zero region.

A final test of the kinematic fitting program was to examine for a sample of the $pp\pi$ events the relative adjustment of the momentum done by the routine. That is (change of momentum)/(initial momentum). This is shown in figure 23 and indicates that the adjustment is symmetrical about zero and averages about 2 percent.

The criteria for accepting events into one of the various event types were that the ionization of the tracks was consistent with the particle identification, the respective kinematic test indicated consistency with the type, and in the case of the 3-body types the beam angle as calculated from the adjusted momenta was within 50 of the direction of the theta target. As has been mentioned before, the range of ionization on the film was not large and it was not always possible to uniquely identify all of the particles by ionization. Most of the time it was possible to distinguish between pions and other particles. From about .3 bev/c to .95 bev/c the proton ionization is twice minimum or better while the pion ionization is almost minimum. Below .3 bev/c the range-momentum relation begins to be useful in identifying the tracks. In this respect it would not have been possible to always distinguish between the pp π^- events and one of the several pK π types had not the incident momentum of the K 0 's been known. Adair (26) estimated the momentum of the Ko's to be 1050 +/-150 mev/c. whereas the incident neutron momuntum ranged from 1000 mev/c to above 2000 mev/c. See figure 24. Most of the events found had an incident momentum larger than possible for a K^O and could hence be called neutron events. The contamination from the Ko's in the beam will be insignificant in the neutron events and present only at the lowest energies. However the contamination by neutrons in a study of the K⁰'s may be considerable since the neutron spectrum overlaps the K^o spectrum and the number of the neutron interactions is approximately 100 times larger.

Tests were made by running some of the $pp\pi^-$ events through the program for the four body types. We found that about four tenths of the three body events would give reasonable incident momenta for the $pn\pi^+\pi^-$ identifications but only one in a sample of one hundred fit the $pp\pi^-\pi^0$ identification. Fortunately the $pn\pi^+\pi^-$ identification can more often be distinguished by ionization. We therefore feel that any contamination between the types of event is not too serious.

Of the events scanned we selected 3441 to analyze for this paper. From these we identified 2012 as $pp\pi^{-}$, 633 as $pn\pi^{+}\pi^{-}$, and 65 as pp π_{π}^{-0} . This left 791 not counted. In studying these remaining events we found that about 245 of them appeared to be real $pp\pi$ events which were excluded due to a calculated beam angle of larger than 5°. We made a scatter plot of the direction cosines of the beam particle of these events to see if they might indicate a source of neutrons other than the theta target, but they do not. See figure 26. They seem to spray uniformly about the direction of the theta target in azmuth but they do tend to be going slightly upward entering the chamber. Of the remaining 487 events 97 appeared to be ppm events which barely failed the chisquare test that we imposed. Of the remaining 390 events 134 were not identified due to errors in measurement. Of these about 60 percent had tracks that were very short due to leaving the chamber and about 40 percent had tracks that were either fuzzy or obscured by some background track or otherwise hard to measure. Repeated measurement of these events did not improve them. This left 254 events unidentified principally because the ionization was not consistent with any of these types. Table 1 summarizes these results.

Table 1. Classification of the events.

Event type	Number	Percent
pp n	2012	58.4
pn n n n	633	18.4
pp n n	6 5	1.9
$pp\pi^{-}$ but angle larger than 5°	245	7.1
ppm but chisquare larger than 7.8	97	2.8
Errors prevented identification	134	3.9
Otherwise not identified	253	7.6
Total	3441	

IV. RESULTS AND INTERPRETATION

A. THE pp T EVENTS

In order to compare the results of this experiment with the peripheral model we have written a computer program to calculate the expected spectra of various variables. The calculation is based on the very detailed theoretical report by Ferrari and Selleri (21). In this report cross-sections and spectra are presented in a general form and in the "pole approximation" which means when the transfered particle is considered to be real. We have written the program using the pole approximation and have not included any interference terms. The differential cross-section in all final variables reduces to:

$$d\sigma = \frac{G^{2}}{(2\pi)^{2}F} \frac{\Delta^{2} + (m_{2} - M_{2})^{2}}{(\Delta^{2} + M^{2})^{2}} \omega^{2} \frac{P_{i}^{\alpha}}{q_{3}^{\alpha}} \frac{d\sigma_{i}}{d\Omega} (\omega, \cos \sigma_{i}^{\alpha}).$$

$$\cdot \delta^{q} (P_{f} - P_{i}) \frac{d^{3}g_{i}}{g_{10}} \frac{d^{3}g_{2}}{g_{20}} \frac{d^{3}g_{3}}{g_{30}} ,$$

where G is a coupling constant, $F = \{(p_1 \cdot p_1)^2 - {M_1}^2 {M_2}^2\}$, Δ is the 4-momentum transfer (see figure 2), M, m, and μ are the masses of incident, outgoing, and transfered particles, ω is the invariant mass of the q_1q_3 system, the Q superscripts imply evaluation in the rest system of q_1 and q_3 , the δ -function brings about over-all 4-momentum conservation, and σ_i is the cross-section for the process:

$$P_1 + k \rightarrow q_1 + q_3.$$

In order to evaluate the spectrum of any variable one must integrate this equation over the proper variables. A change of variables is made to a set of variables which includes the one whose spectrum is desired, then the resulting equation is integrated over all other variables. Ferrari and Selleri have given expressions for the spectrum of lab and center of mass energy and of center of mass angular distribution of particles \mathbf{q}_1 and \mathbf{q}_2 which are in a form for easy computation.

In the above expression for the differential cross-section notice that all of the quantities are straightforward kinematical quantities except $\frac{4\sigma}{4\pi}$. Our computer program is written so that the part which calculates this factor is a separate subroutine and can easily be changed. We have written several forms of this subroutine:

one inserts for the cross-section a Breit Wigner type of resonance multiplied when necessary by an angular part (eg. 1 + 3cos0) which would use in the case of n-p inelastic scatter the value and width of the resonance in pi-nucleon scattering. We have also written a subroutine which does a linear interpolation in energy on tables of the cross-section or the coeficients in the power series of cos0 up to cos50 for the differential cross-section. The values for the coeficients as a function of energy were obtained from a thesis by Wood (30) and a few low energy points were obtained from Goodwin, et al, (31). Hence we are able to calculate the spectra from the peripheral model using the actual experimental cross-section for the upper vertex as a function of the energy and angle.

We have also written a routine which inserts a cutoff function of the form $e^{-\Delta^2}$ into the calculation in order to compare the pole approximation with a non-pole approximation. Spectra will be presented using the pole approximation with the experimental partial cross-section, the cutoff function with the experimental partial cross-section, and the cutoff function with a Breit Wigner resonance for the partial cross-section.

To facilitate comparison with this theory we have subdivided our experimental data into slices of incident energy. The subdivision was made in 50 mev/c slices of incident center of mass momentum as shown in table 2.

Table 2. Subdivision of the $pp \pi^{-}$ data.

Slice	Lab Momentum		C. of M. Momentum	No. of Events
	From	To Cente	r From To Center	
1	1.28	1.43 1.35	0.55 0.60 0.575	361
2	1.43	1.58 1.50	0.60 0.65 0.625	339
3	1.58	1.75 1.67	0.65 0.70 0.675	378
4	1.75	1.92 1.84	0.70 0.75 0.725	294
5	1.92	2.10 2.01	0.75 0.80 0.775	152
Total				1524

Momenta are in bev/c.

The total elastic and charge exchange cross-sections for \overline{m} p scattering are shown in figure 67. The upper limits of M* for the five slices of the data are shown and indicate that only the lowest peak corresponding to the 3,3 resonance in the pi-nucleon system is involved in these data. There may be some effect due to the broader peak in the elastic cross-section at 1.5 bev in the higher slices but it will not be discernible as such from the general shape of the curves—since it is so broad and the higher slices only approach this peak.

In the pp π final state the protons of course are indistinguishable. Also either the proton or the neutron can scatter from the pion in the cloud of the other nucleon. Hence there are two possible diagrams for this reaction (See figure 68.), and in both cases either proton must be counted. In diagram 1 the probability of the emission of the π^0 is half that of the π^- in diagram 2, but the charge exchange cross-section is approximately twice the elastic cross-section so that both diagrams contribute about equally.

We have also used the ATHOS program from Berkeley, Calif. to calculate invariant phase space curves for comparison. In all of the curves to be presented for the $pp\pi^-$ data the peripheral model curves are drawn with a solid line and the phase space curves are shown dashed. In some cases the phase space curves alone are shown, in which case they are still dashed. Ordinates on the graphs are twice the number of events for all curves except those describing the pion distributions, in which case ordinates are the number of events.

Center of mass momentum distributions of the protons are shown in figures 27 - 31 and compared with the peripheral model and the statistical model. One can see that the agreement with the peripheral model is fairly good from slice to slice with the exception of slice 1. This trend will be seen in other variables also and might have been anticipated since the kinematical limit of M* for slice 1 is barely over the peak in the cross-sections as seen in figure 67. The spread in incident energy within the slice may even affect the shape of this curve.

Lab kinetic energy distributions of the protons are shown in figures 32 - 36. Again comparison between the data, the peripheral model, and phase space is shown. The general features of the peripheral model are low energy peaking and a rather broad flat distribution toward higher values before dropping down to zero at the upper limit. The low energy peak comes from p2 in diagram 1 and from p1 in diagram 2. See figure 69. The proton p2 is the proton resulting from the stationary proton in the bubble chamber which has emitted a pion and recoils. Its low kinetic energy distribution indicates the predominance of low momentum transfer in these peripheral interactions. The proton p₁ here results from the pion in the cloud of the passing nucleon scattering the stationary bubble chamber proton. Its low energy distribution simply reflects the difference in mass between the pion and the proton. The distribution from proton p2 in diagram 2 contributes a broad distribution which causes the shoulder at the high end of the curves. This also indicates low momentum transfer to the spectator nucleon. Proton p₁ in diagram 1 contributes a broad lump which fills in the center of the distribution. As before, slice 1 does not show enough structure to warrant discussion but the agreement with the peripheral model is seen in the higher slices as the departure from the statistical model becomes more pronounced.

Center of mass angular distributions of the protons are shown in figures 37 - 41. Comparison with the peripheral model ²¹ shows excellent agreement for all slices.

The invariant mass, M*, of the $p\pi^-$ pairs is shown in figures 42 - 46. M* is the total energy of the two particles in the rest system of the pair. The effect of the 3,3 resonance between the pion and the proton can be seen clearly in all slices as a peak at M* = 1.237 bev. Again the agreement with the peripheral model is good.

Figures 47 - 51 show the angular distribution of the pion in the rest system of the $p\pi^-$ pair. The θ = 0 direction of this system is the direction of motion of the isobar from the center of mass system of the event. This angular distribution does not reflect directly the angular distribution of the four pronged vertex in diagrams 1 and 2. In the experimental distributions no structure is seen except an isotropic distribution.

For completeness, distributions of lab kinetic energy of the pions are shown in figures 52 - 56. Also pion center of mass momentum distributions are shown in figures 57 - 61, and center of mass angular distributions are shown in figures 62 - 66. Phase space curves are also shown for the lab and center of mass energy distributions. The angular distributions show an isotropic distribution.

Finally we compared the results of this experiment with n+p interactions with the p+p interactions of Barnes, et al ⁽⁶⁾ at 970 mev. In the present experiment there is no good way of estimating the total flux of neutrons in the chamber in order to get absolute cross-section values. However in the p+p experiment the total flux of protons was known and such cross-section values were obtained for the final state pp π^0 , which is similar to our pp π^- state. Now the incident p+p system is always in a T = 1 state while the n+p system is in the T = 1 state half the time and the T = 0 state half the time. Assuming that in both cases the reaction N+N \rightarrow N+N+ π goes by way of the 3,3 resonance in the pi-nucleon system, isotopic spin arguments predict that the ratios of the final states from these reactions will be as follows:

$$n+p \rightarrow n+(p+\pi^{0}) : n+(n+\pi^{+}) : p+(n+\pi^{0}) : p+(p+\pi^{-}) ::$$

$$2/12 : 1/12 : 2/12 : 1/12 ;$$
and
$$p+p \rightarrow n+(p+\pi^{+}) : p+(n+\pi^{+}) : p+(p+\pi^{0}) ::$$

$$9/12 : 1/12 : 2/12 .$$

Noting that the final state $pp\pi^0$ should occur twice as often as the $pp\pi^-$ state by these arguments, we normalized our $pp\pi^-$ data to the total p+p cross-section and then compared our data with one half of the $pp\pi^0$ spectrum of lab kinetic energy. See figure 70. The similarity of magnitude of the two histograms merely indicates that the $pp\pi^0$ cross-section is the proper fraction of the total cross-section, but the similarity of shapes of the two histograms is good evidence for the validity of charge independence.

It is also interesting to note the similarity in the shape of the curves of M^* obtained from the peripheral model and from phase space with a resonance between pion and nucleon folded in. In the

ATHOS program there is a subroutine, ARAMIS, which does the phase space with resonance. We have used this routine, and figure 71 shows the comparison with the peripheral model. The curves shown are for an incident momentum in the lab of 1.67 bev/c. Comparison at other energies show a similar picture. Both models are roughly similar, as would be expected, but the peaks of the two curves occur at slightly different points and the peripheral model gives a little higher shoulder at the upper end of the spectrum.

B. THE FOUR-BODY EVENTS.

In the case of four particles in the final state with one of them neutral the problem of balancing energy and momentum is not overdetermined, as it is with the three body events. In order to find the missing momentum, we had to assume the direction of the incident particle, assign all masses, and find the incident momentum as well as the component of momentum of the missing particle parallel to the incident direction. The transverse component of the missing momentum is equal and opposite to the transverse component of the sum of the three visible momenta. The two remaining unknown quantities, the parallel component of the missing momentum and the incident momentum, can be solved from the remaining momentum equation and the energy equation. The method used was an iterative one. The first guess for the parallel component of missing momentum was zero, and the resulting energy unbalance was calculated. If the energy unbalance was larger than 1 mev. Newton's method was used to reduce this unbalance. A maximum of ten passes through the loop was imposed, and in all cases where this maximum was exceeded the values of incident momentum were too large to be printed.

The spectrum of incident momentum for the $pn\pi^{T}\pi^{-}$ events is shown in figure 72. Now if the neutrons incident upon the chamber are caused by the pions in the beam interacting with nucleons in the theta target, then this spectrum extends much too high. Accounting for the spread of seven percent in the pion momentum and the Fermi momentum of nucleons in the target, the maximum incident momentum should be about 2.1 bev/c. Figure 72 shows that the spectrum spills over to well above this maximum. I feel that this is mainly due to the restrictions in the kinematic fitting problem coupled with the uncertainty on the measured momenta. If one were to plot the unbalance of energy as a function of incident momentum, he would find that at high values of momentum the curve levels and approaches a constant value. The important difference is that the slope of the curve is smaller on the high side of amy zero point than it is on the low side. The effect is that random errors in the measured quantities will tend to distort the shape of the momentum spectrum to the high side.

In figures 73 - 75 we have the nucleon lab momentum spectra. Here we see that there is a strong tendency to have fast protons and slow neutrons in the lab. This will be reflected also as a strong assymmetry in the center of mass angular distributions of protons and neutrons as seen in figures 76 - 78. The very high piling up of neutrons in the backward direction is not understood.

Plots of the invariant mass of pairs of particles are shown in figures 79 - 87. We see that there is no evidence for any resonance effects at all, neither in the nucleon-pion pairs nor in the pion-pion pairs. Thresholds for 0, 1, and 2 isobar production are about 1.22, 1.66, and 2.12 bev/c incident momentum; hence there should not be any double isobar production, but could be some single isobar production. Nevertheless no evidence of the isobar is seen.

Several attempts were made to select events from the total sample of $pn^+\pi^-$ events in order to find any hidden evidence of the isobar. Events with nucleon angles very close to forward or backward were culled out of the sample, but no isobar was seen. Also no isobar was seen looking at charged tracks only, which should eliminate any effect of the fitting procedure which might mask the isobar.

Since there were so few pp $\pi^-\pi^0$ events, we could not subdivide them into reasonable slices of energy. The spectrum of incident momentum is shown in figure 88, and shows the same tendency to spill over to high values as does the pn $\pi^+\pi^-$ momentum spectrum. Again no evidence of isobar formation was seen for these events.

In all probability the difficulty with these data is due to the fact that the problem is just barely determined, and the data are not too useful. We present it here for completeness, and it is not to be taken as evidence for the lack of isobar formation.

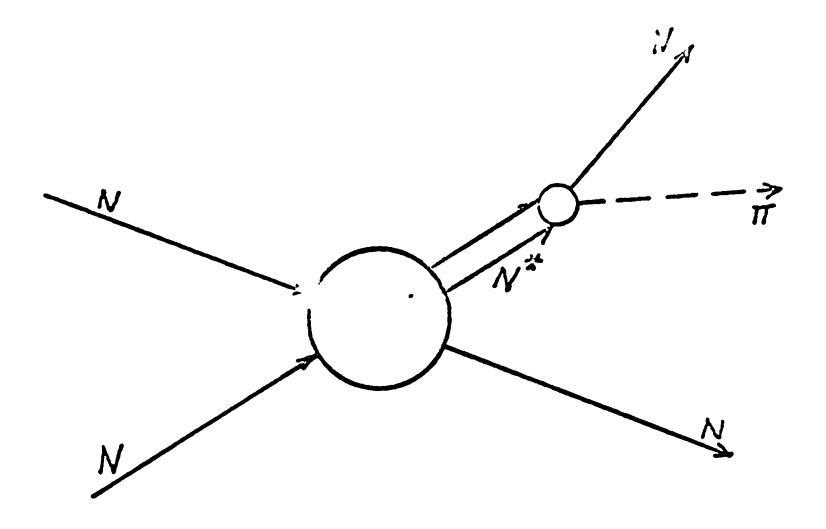


Figure 1a. Diagram representing pion production in nucleon-nucleon collisions in the isobar model.

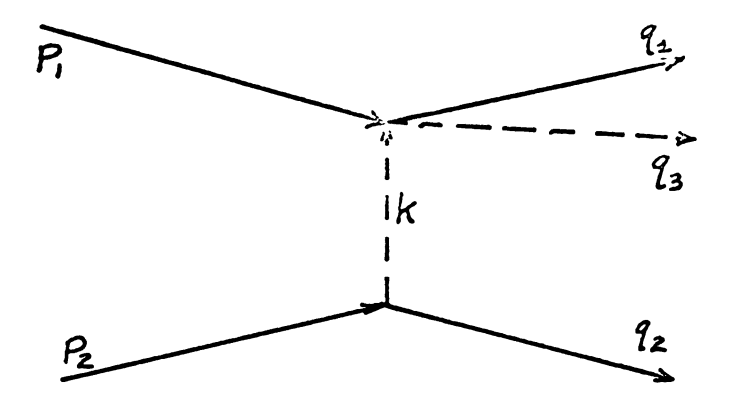
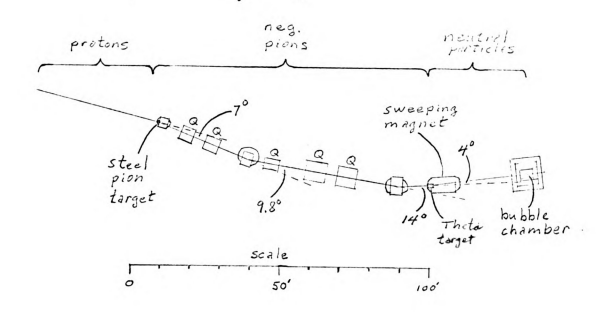


Figure 1b. Diagram representing pion production in nucleon-nucleon collisions in the peripheral model.



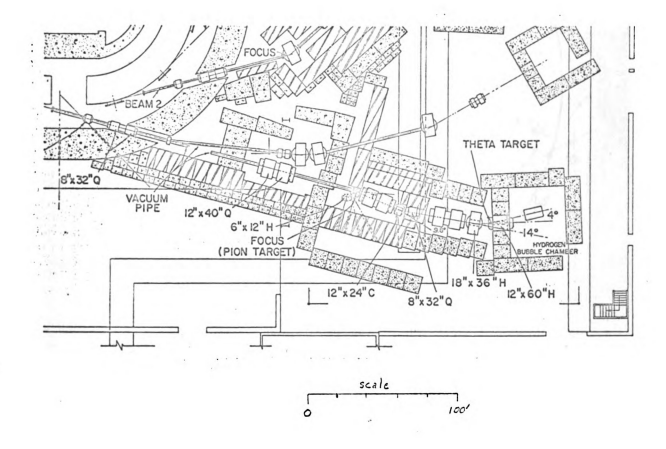


Figure 2. Beam Design.

Shaded blocks are heavy concrete; cross-hatched blocks are steel. Drawing obtained from reference 26.

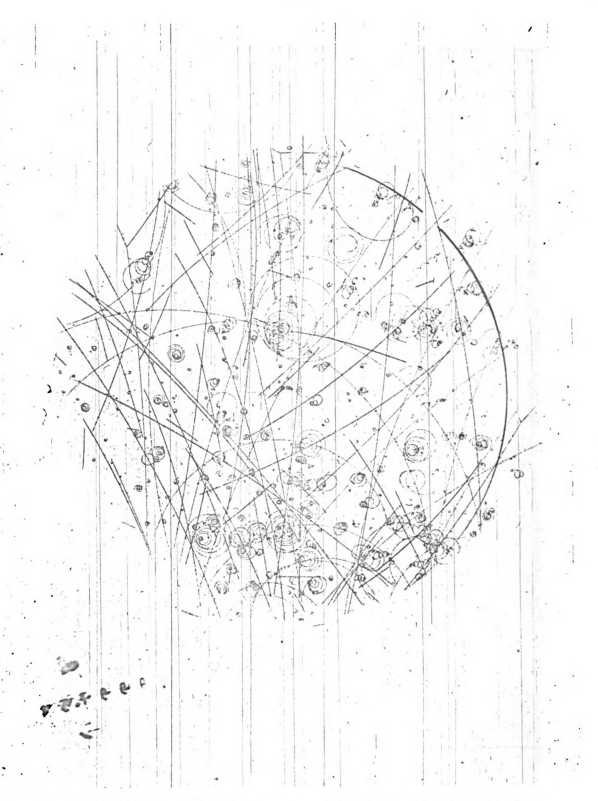


Figure 3. Typical picture. An event originates just above the lower fiducial mark.

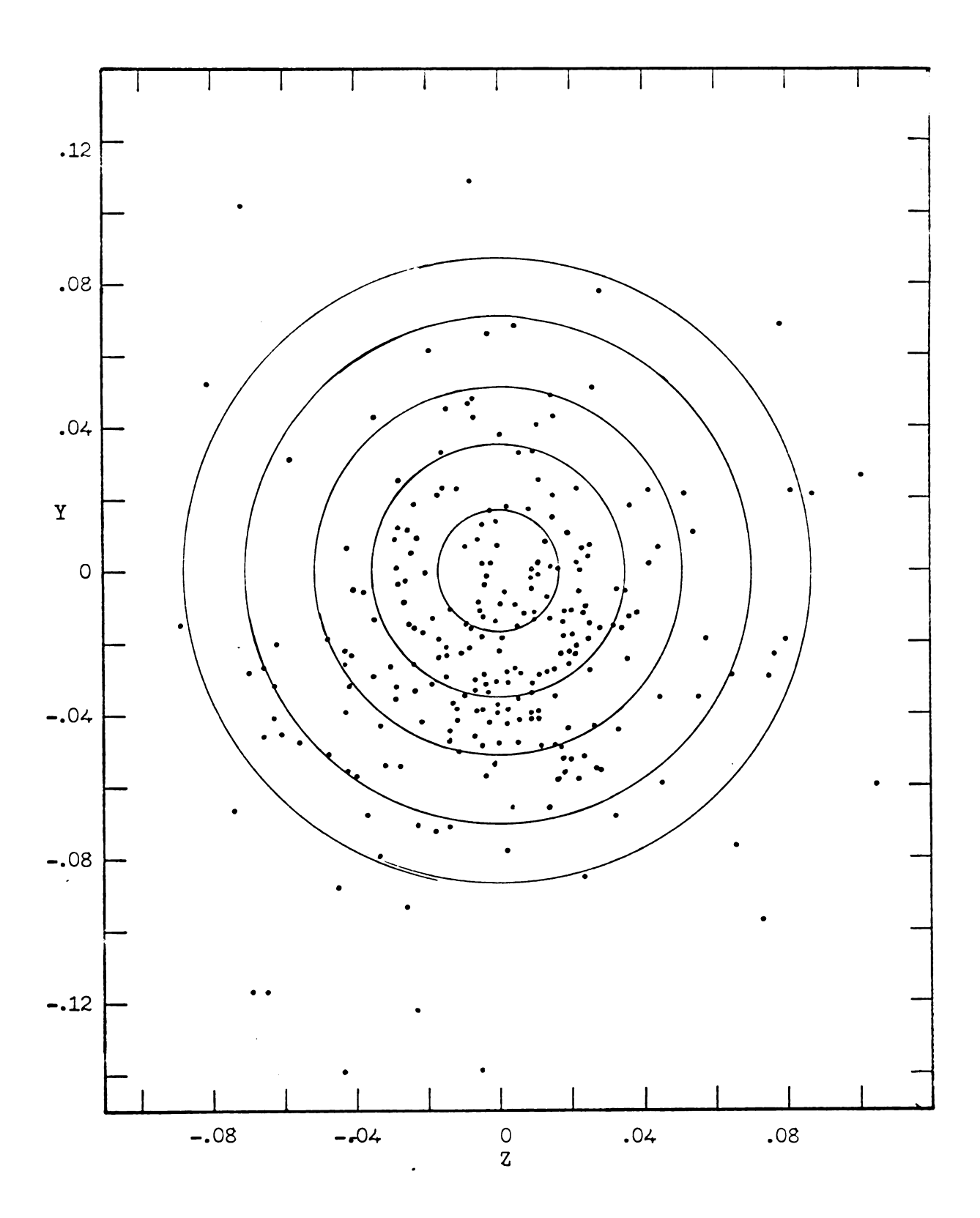


Figure 4. Neutron beam direction cosines.

Circles are one degree apart.

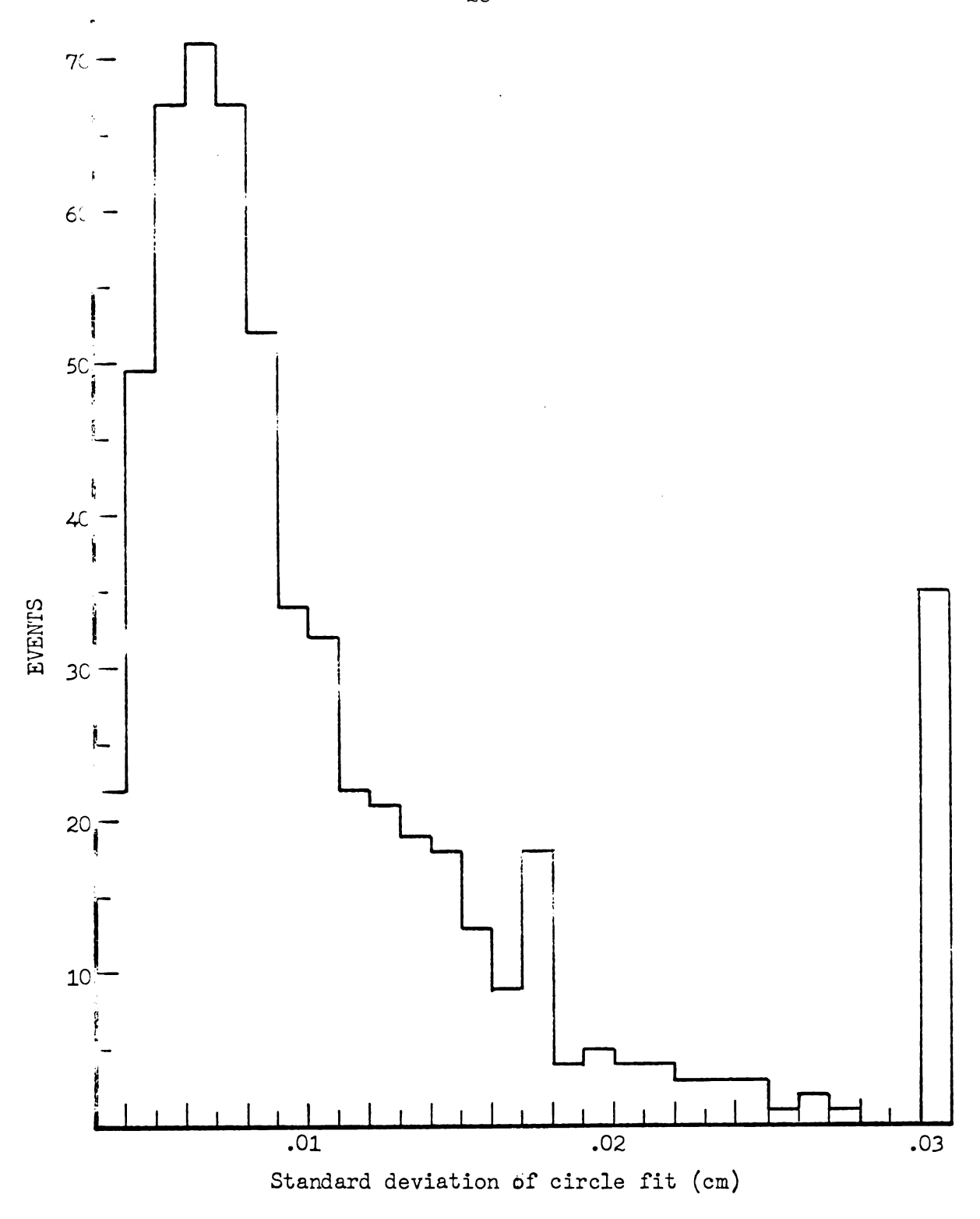


Figure 5. Standard deviation of circle fit for tracks of all ranges.

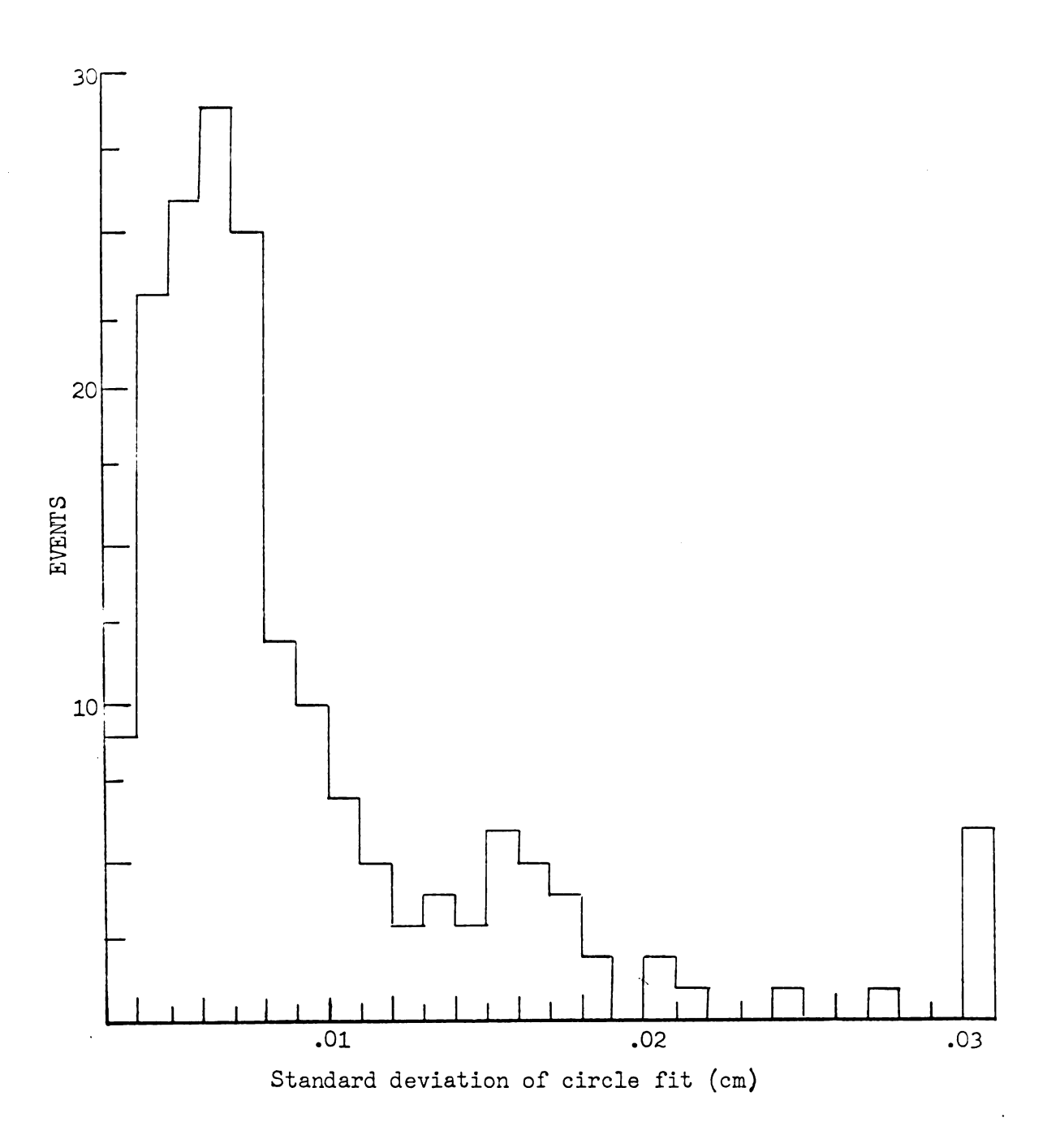


Figure 6. Standard deviation of circle fit for tracks with range between 0 and 10 cm.

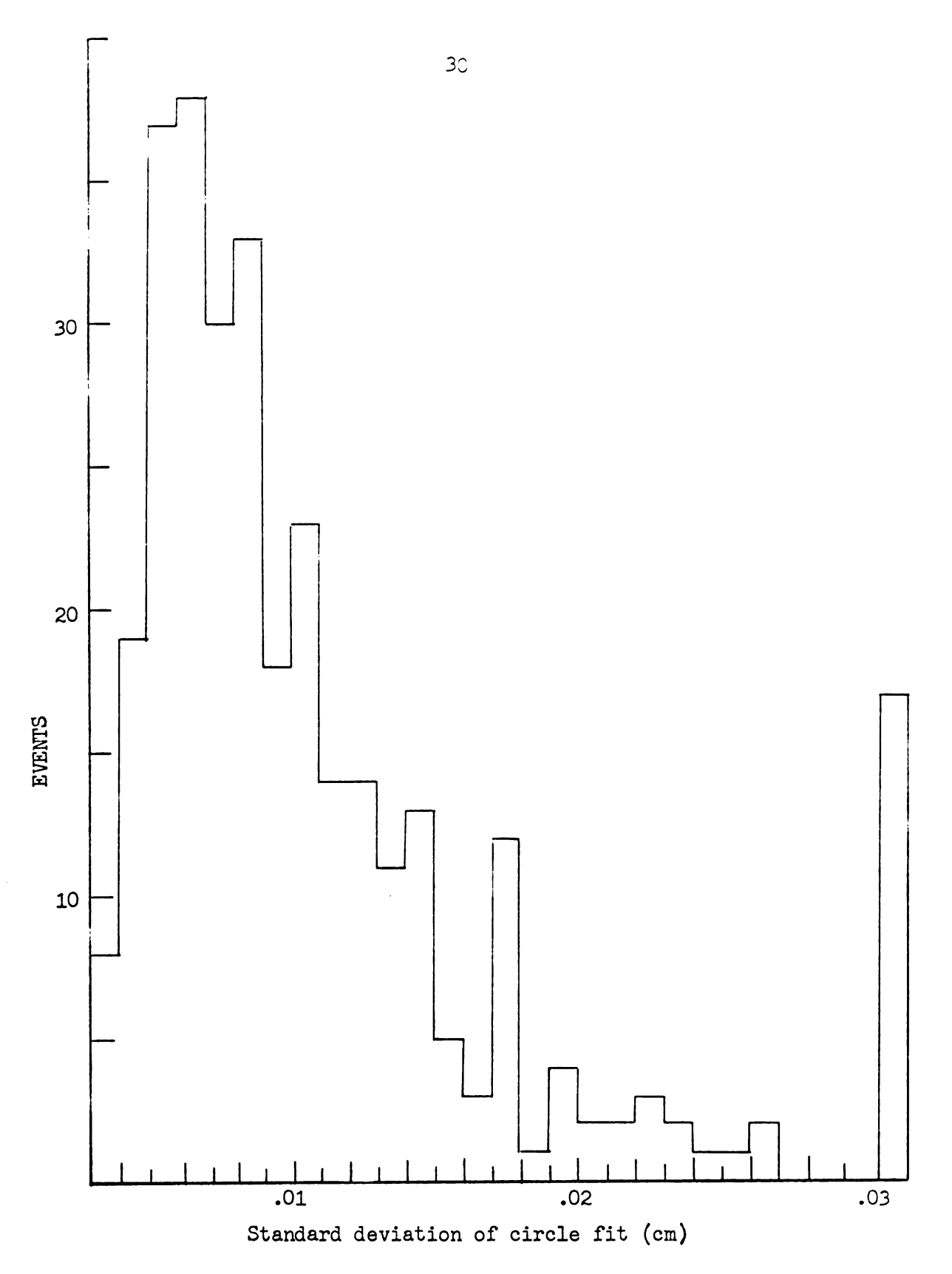


Figure 7. Standard deviation of circle fit for tracks with range between 10 and 20 cm.

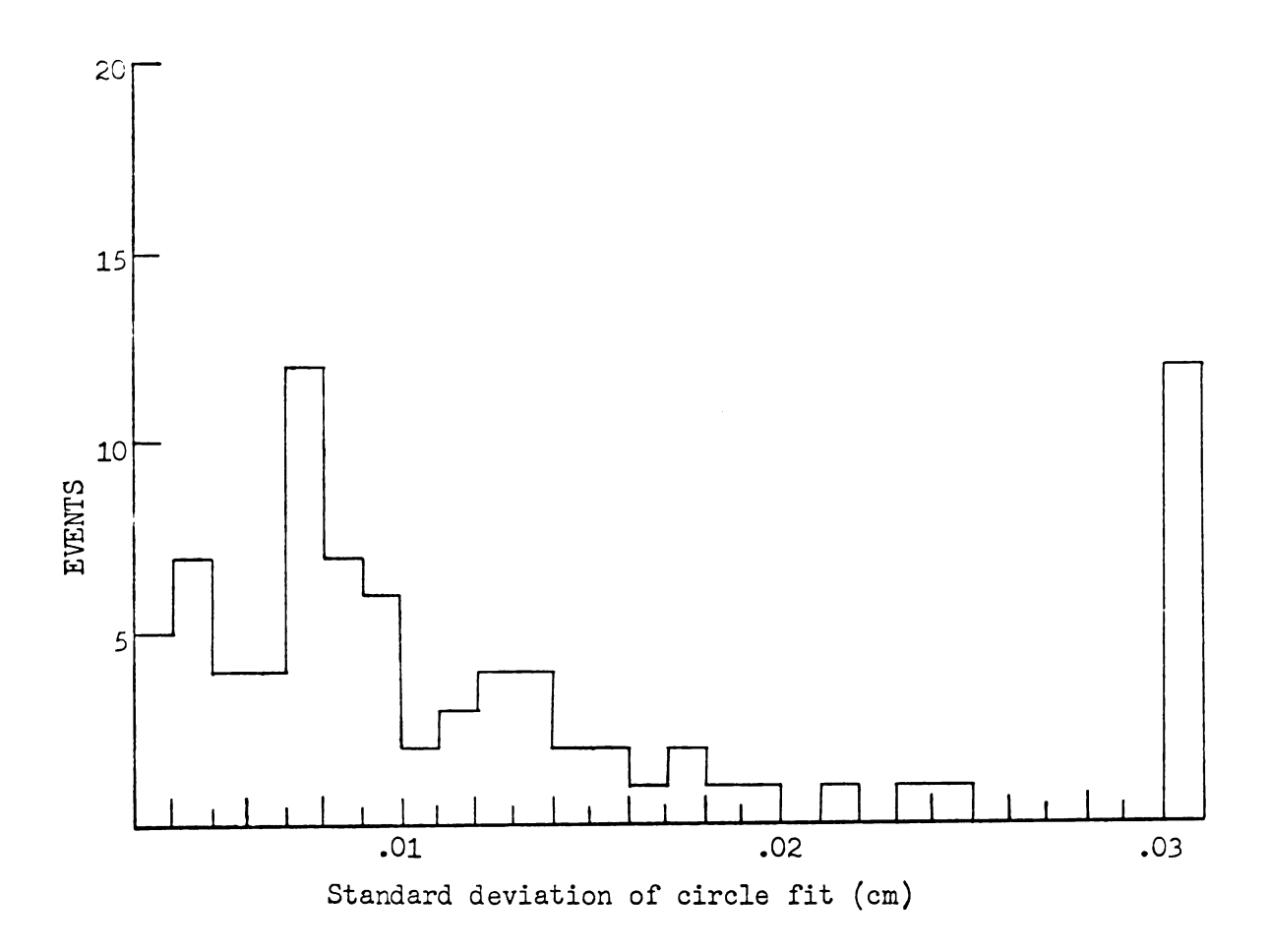


Figure 8. Standard deviation of circle fit for tracks with range greater than 20 cm.



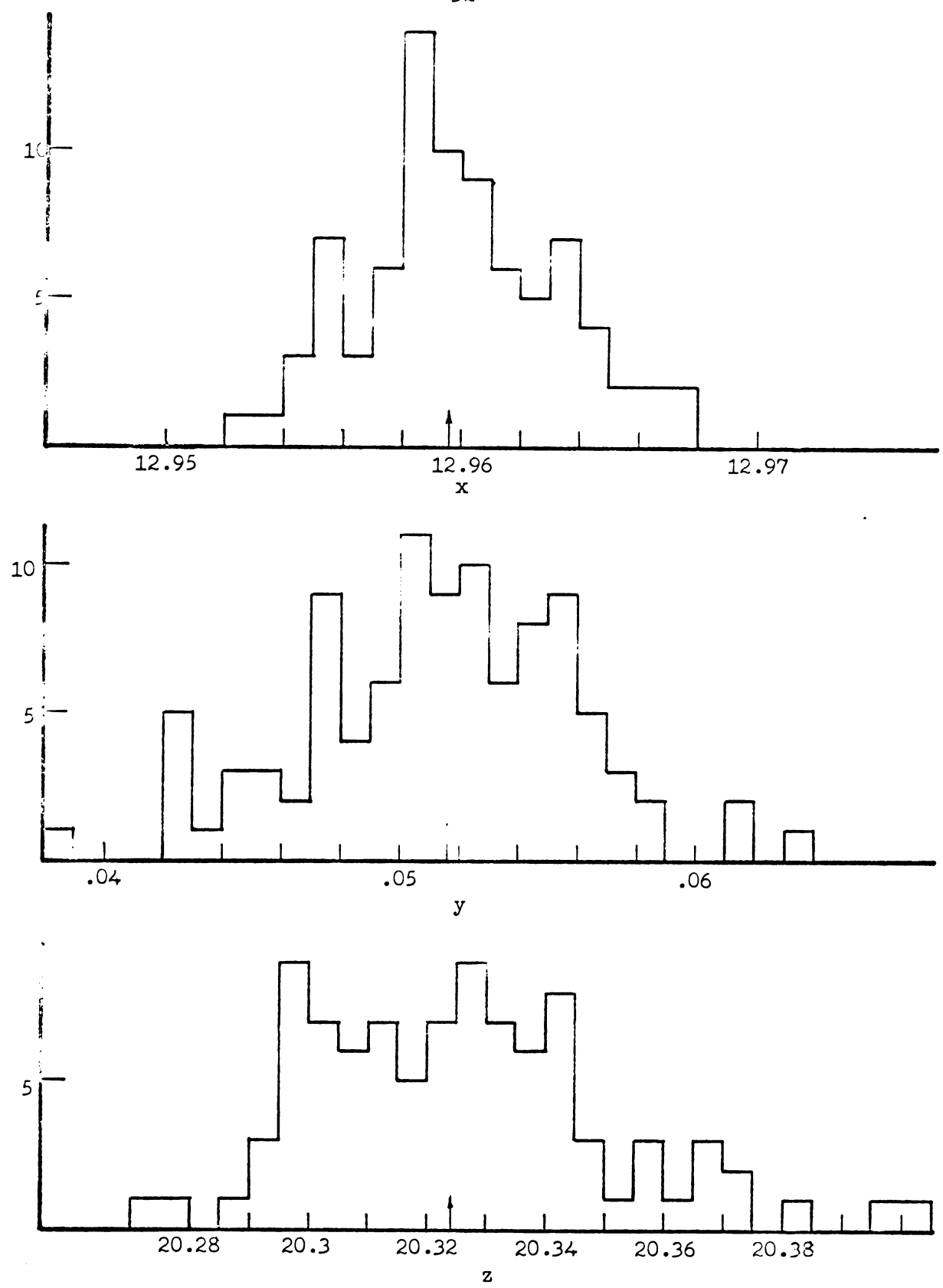


Figure 9. Measurement of back fiducial mark. Position is in centimeters. Note that the scale of the z plot is coarser by a factor of five than that of x and y.



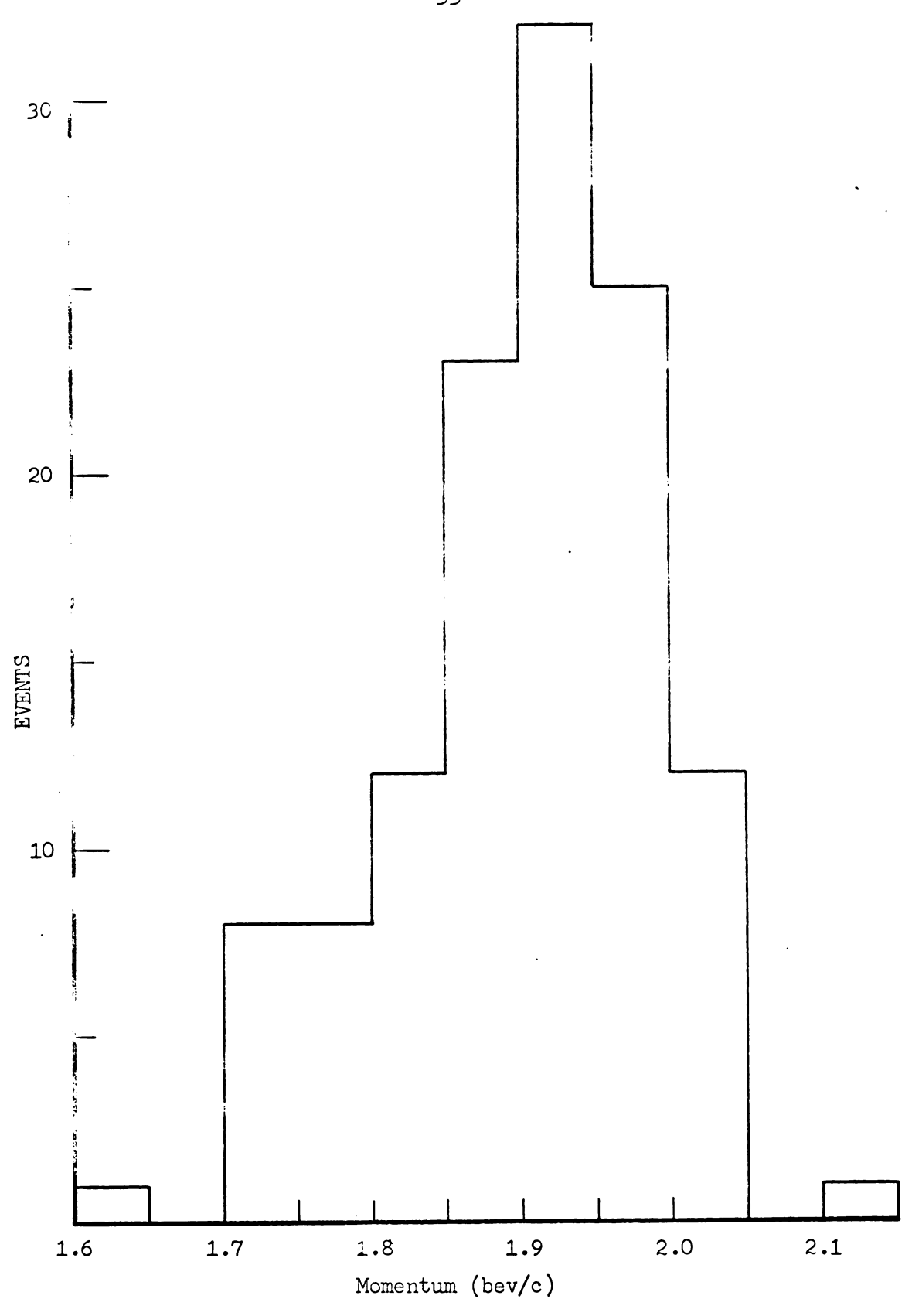


Figure 10. Momentum spectrum of π^- beam particles.

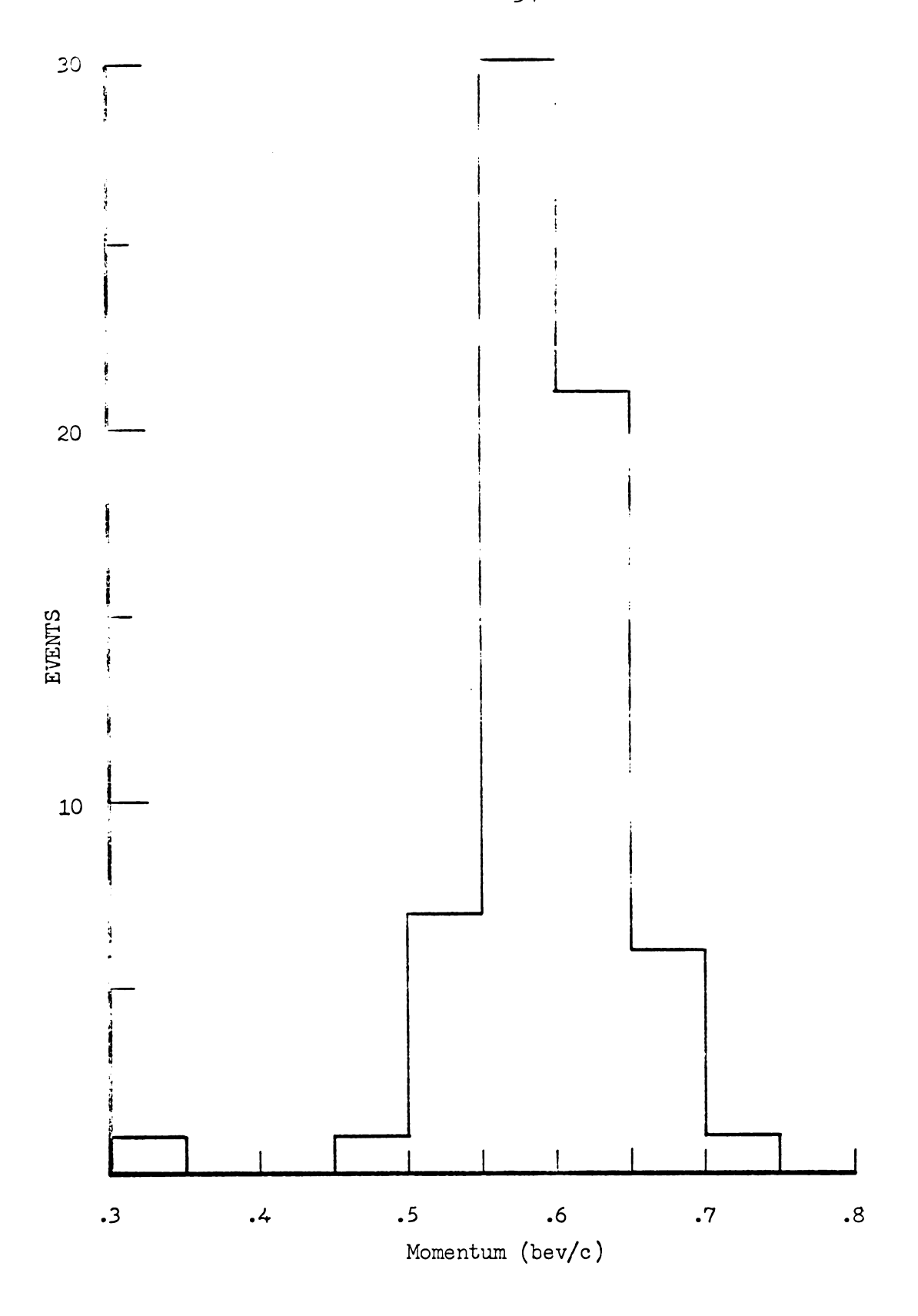


Figure 11. Momentum spectrum of .45 bev kinetic energy positive pions.

Momentum is .6 bev/c.

•

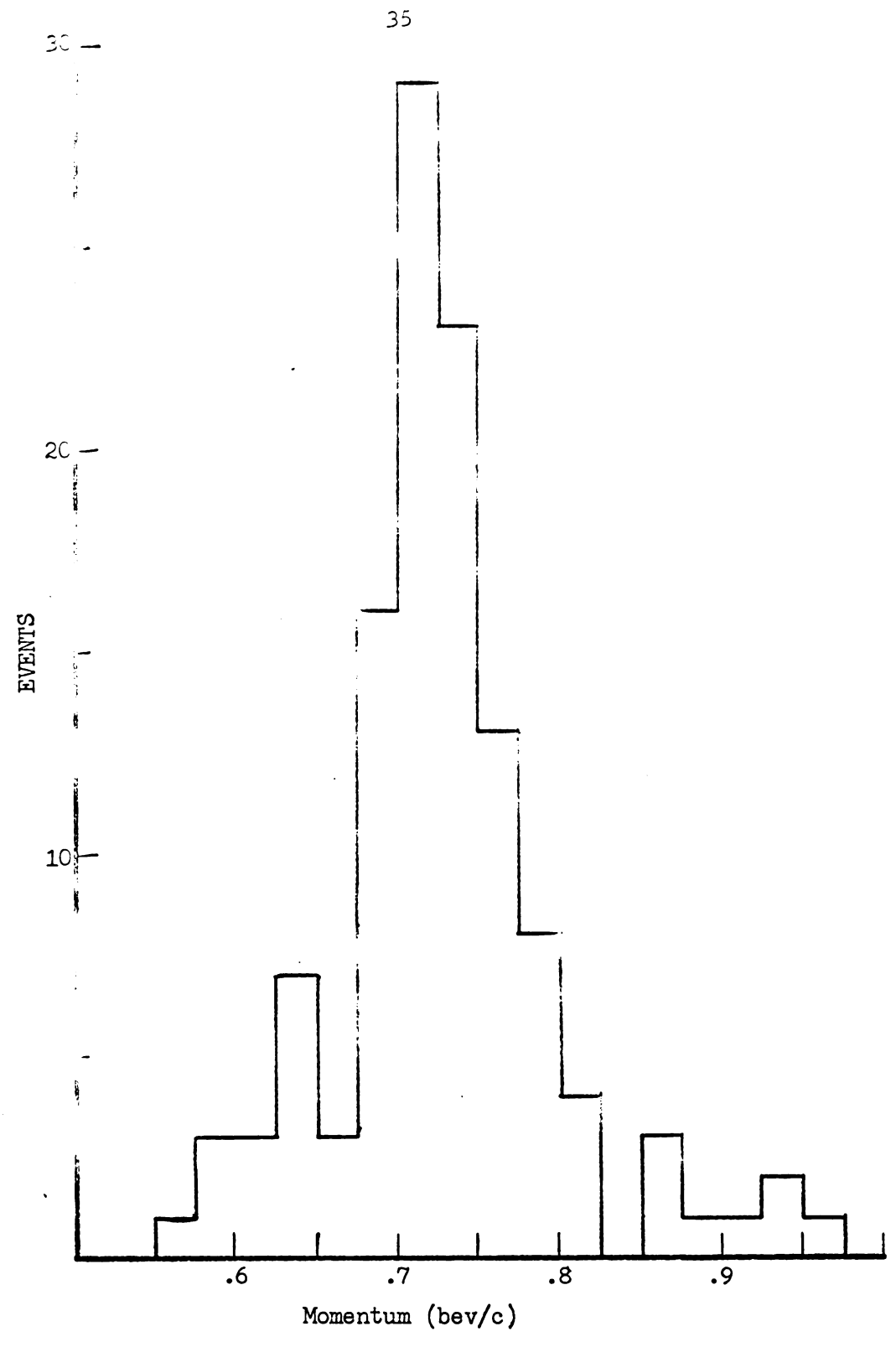


Figure 12. Momentum spectrum of .6 bev kinetic energy positive pions. Momentum is .725 bev/c.

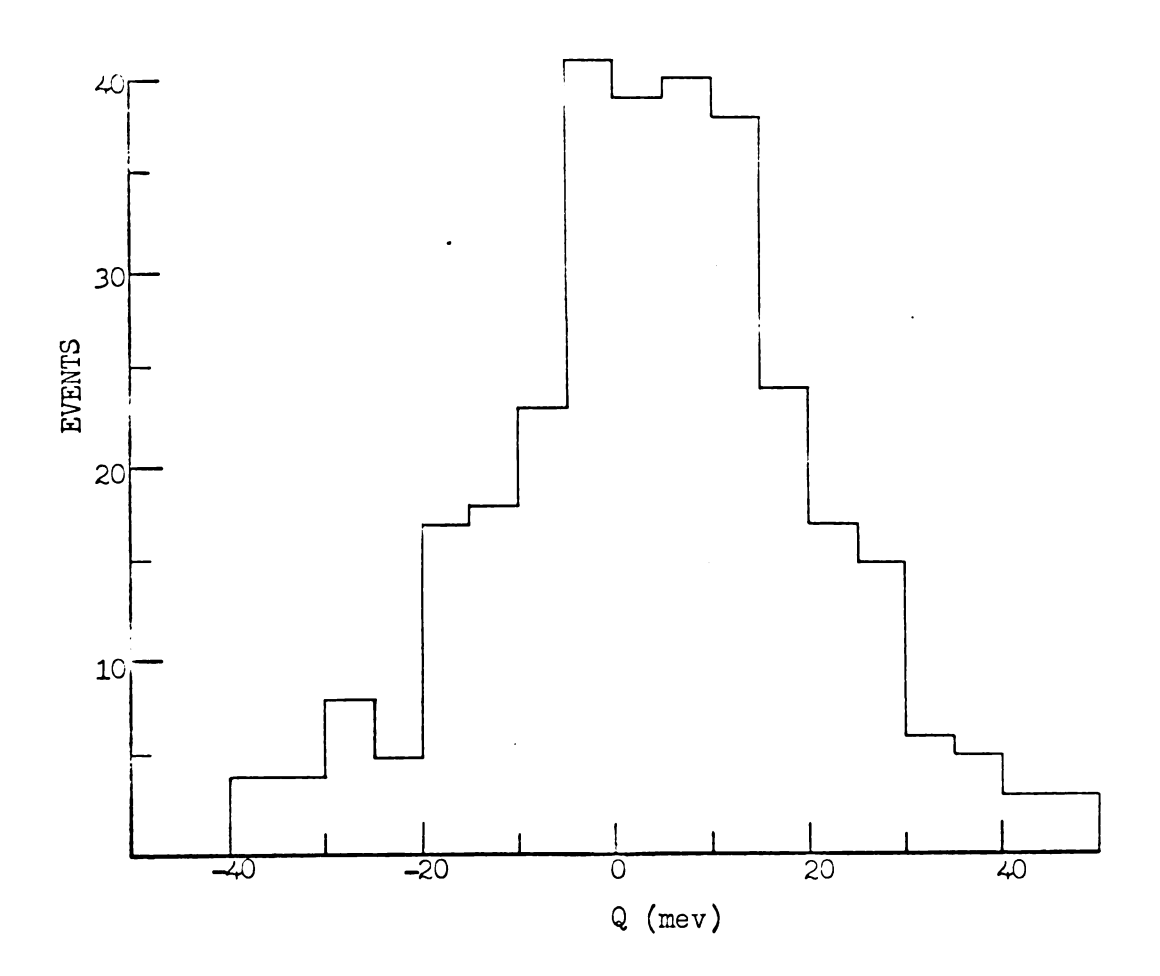
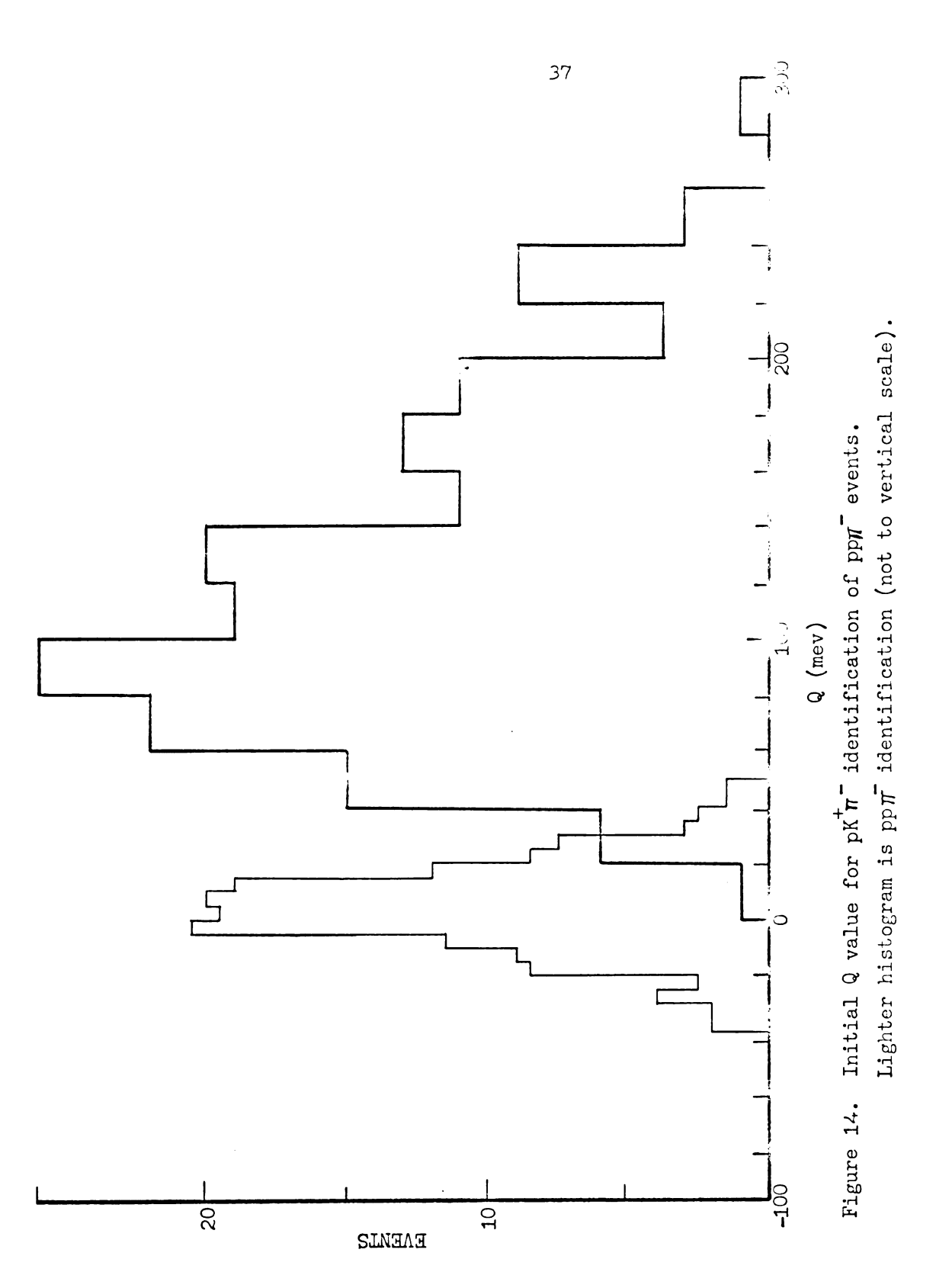
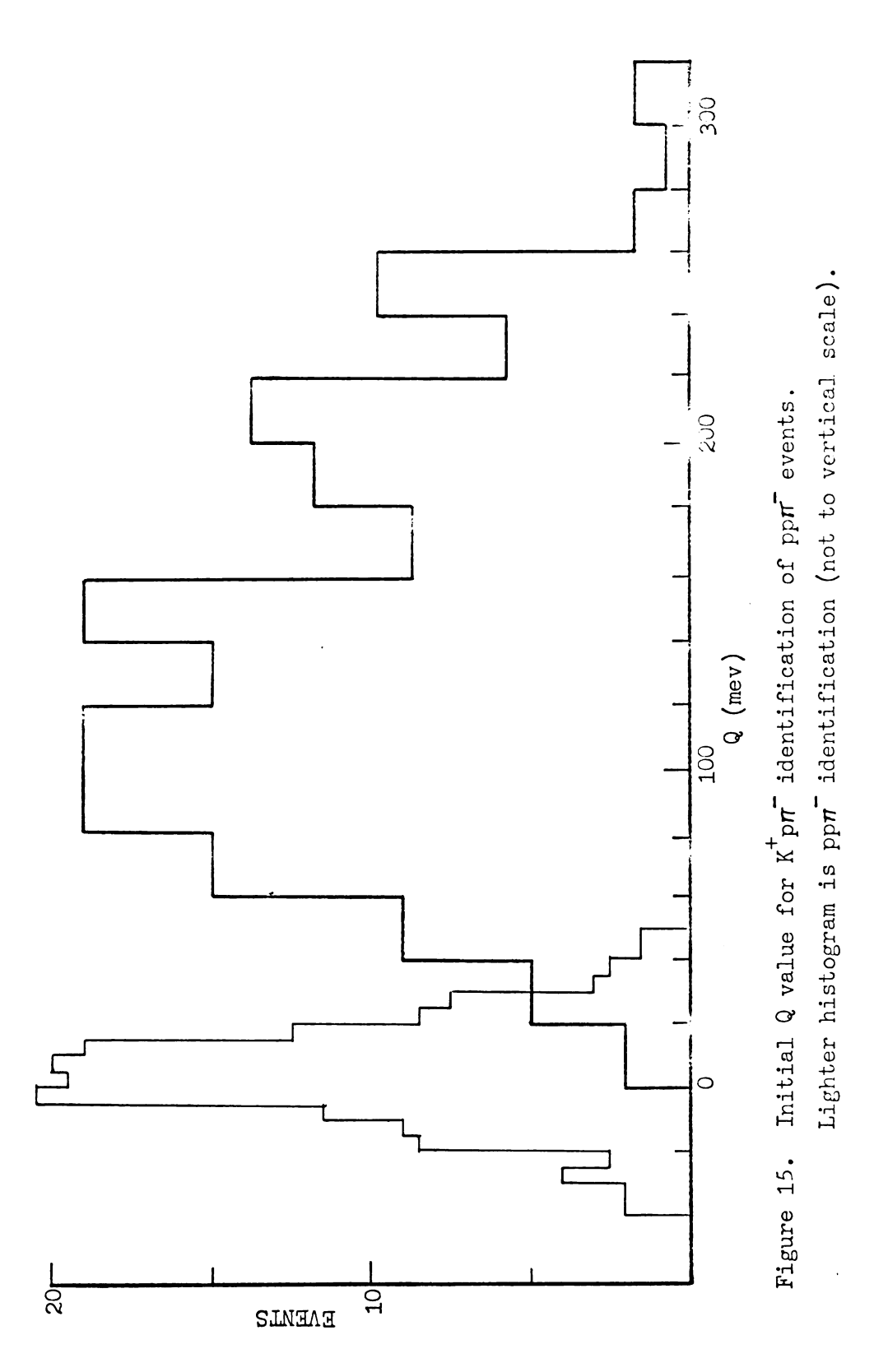
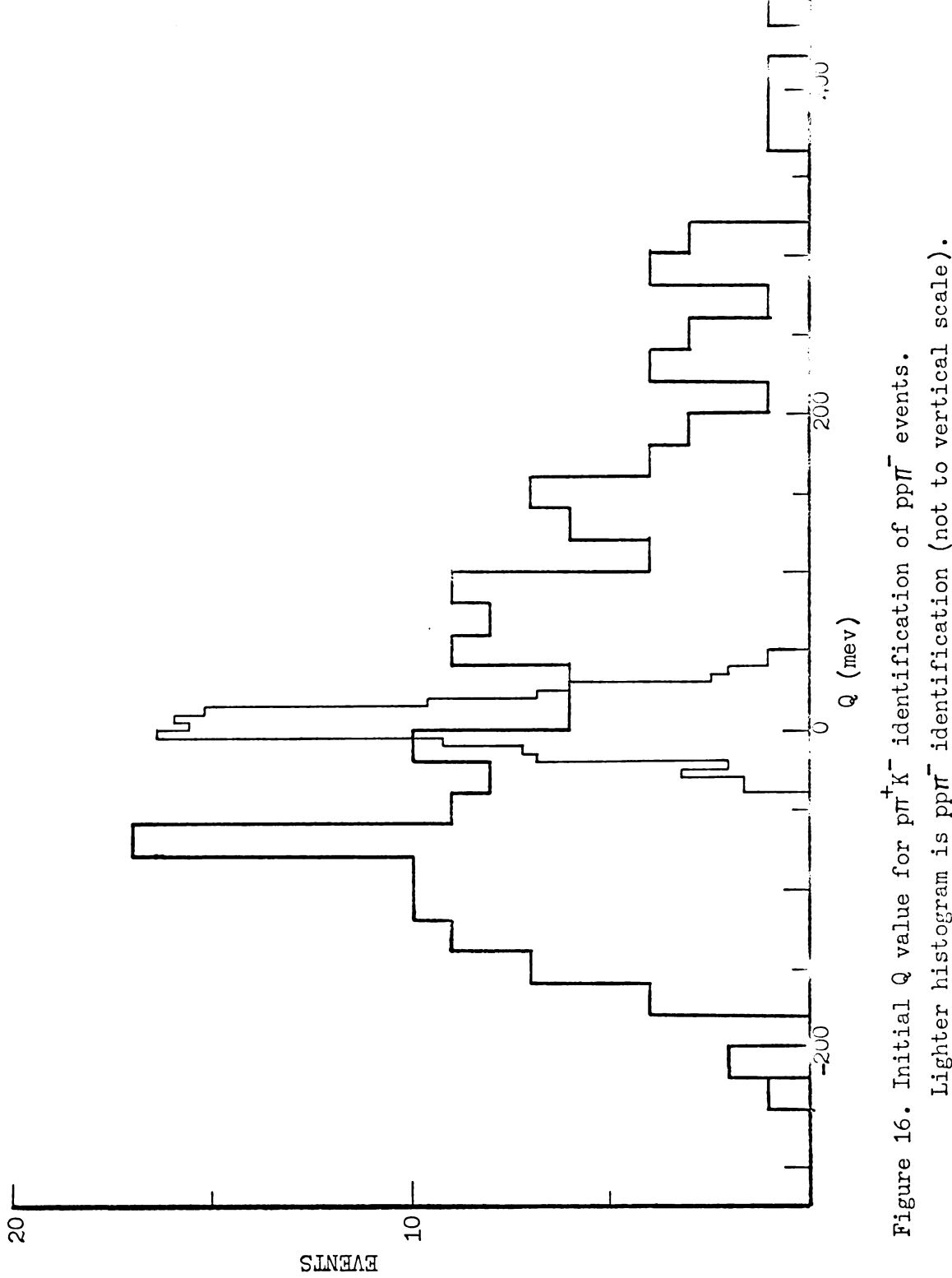


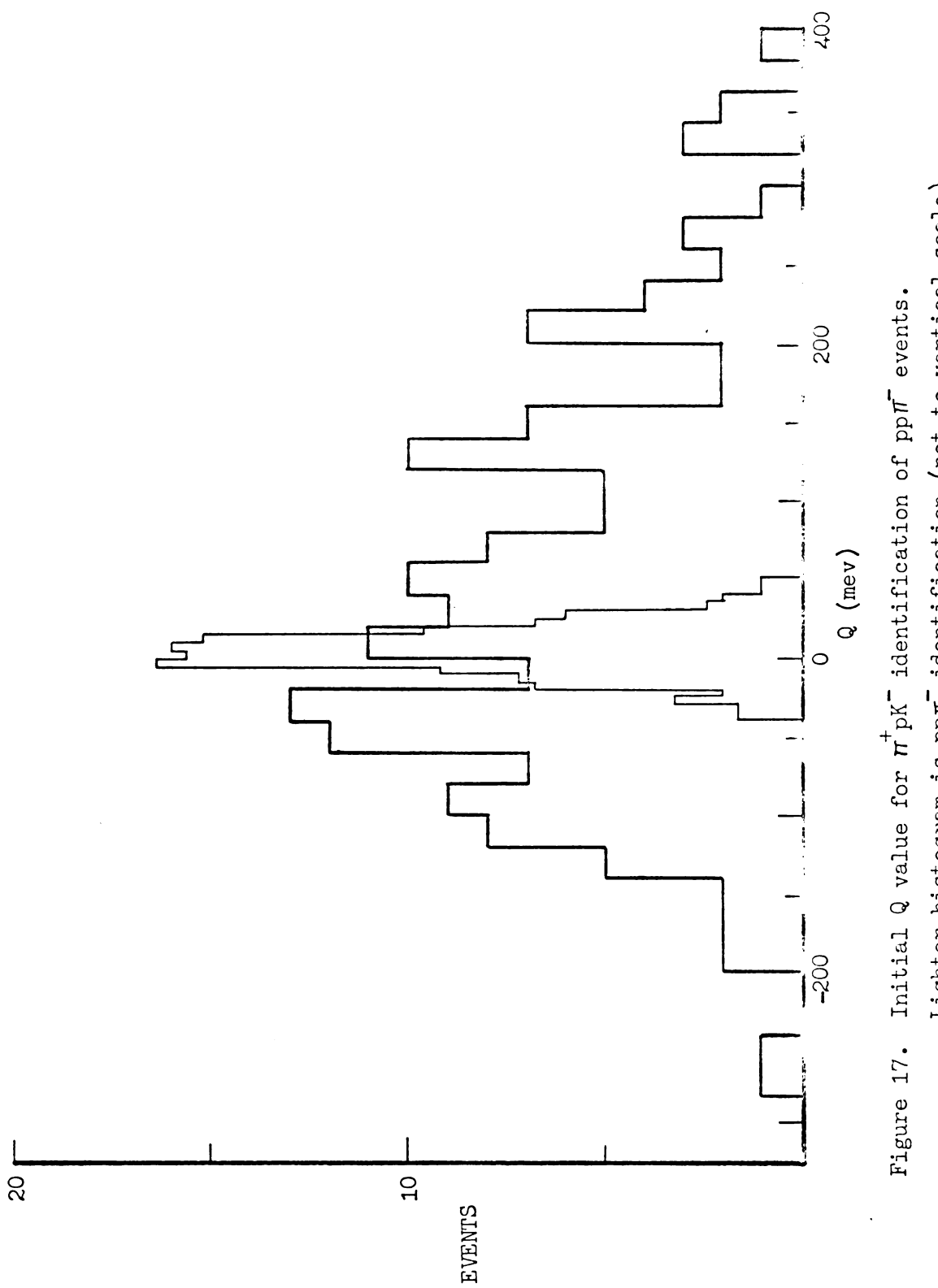
Figure 13. Initial Q value of pp- identification of pp- events.



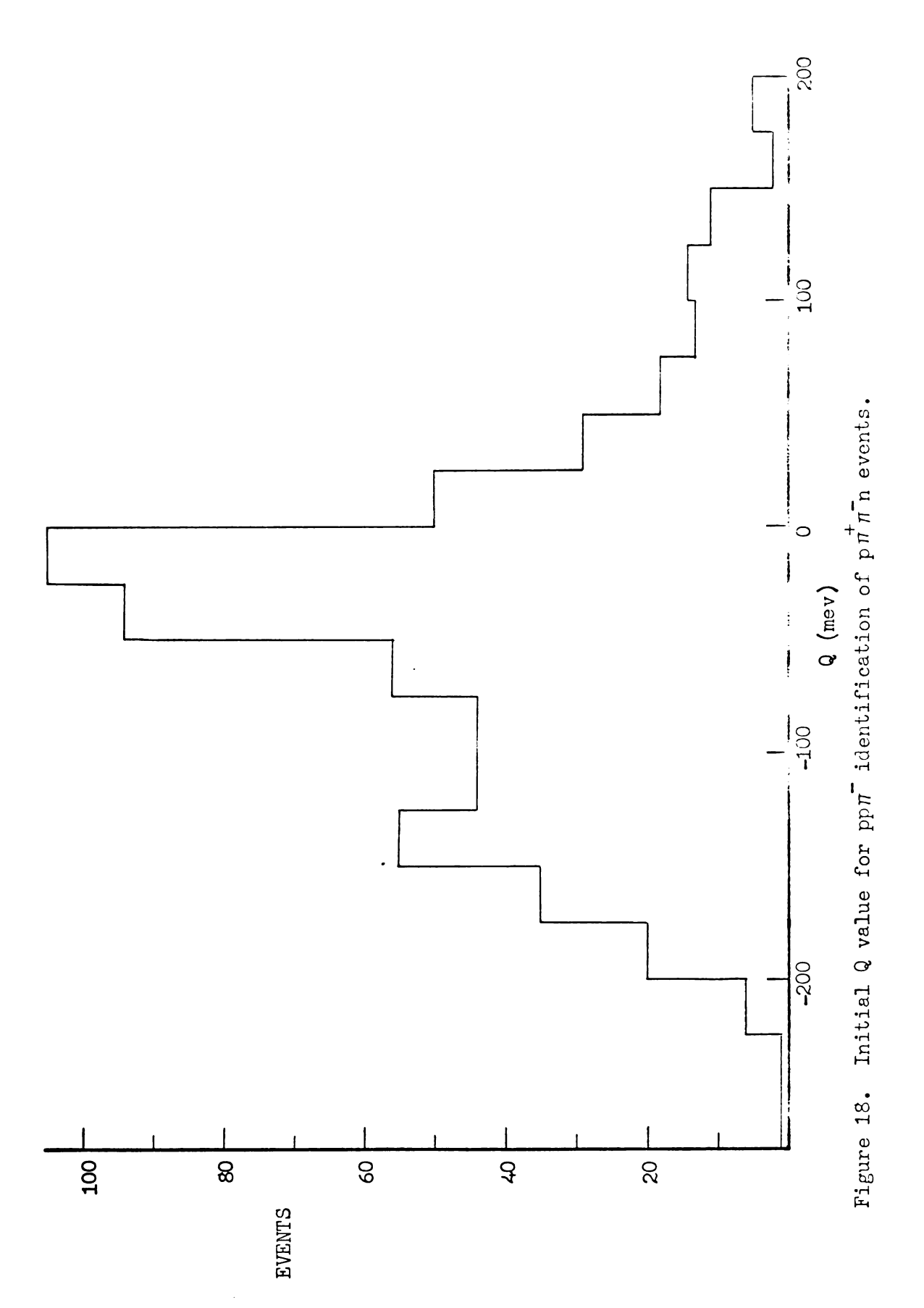




Lighter histogram is $\mathrm{pp}\pi^-$ identification (not to vertical scale).



Lighter histogram is ppm identification (not to vertical scale).



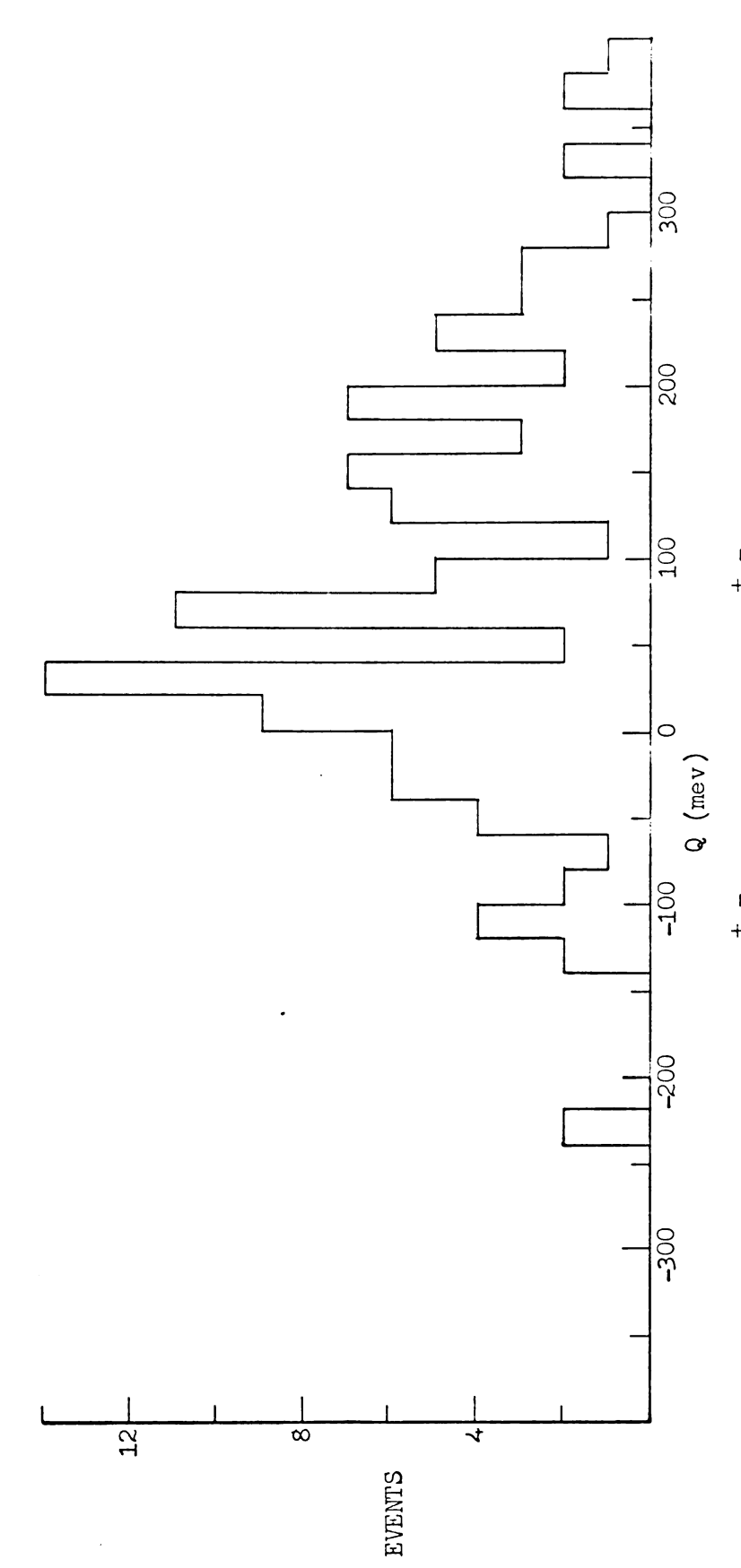
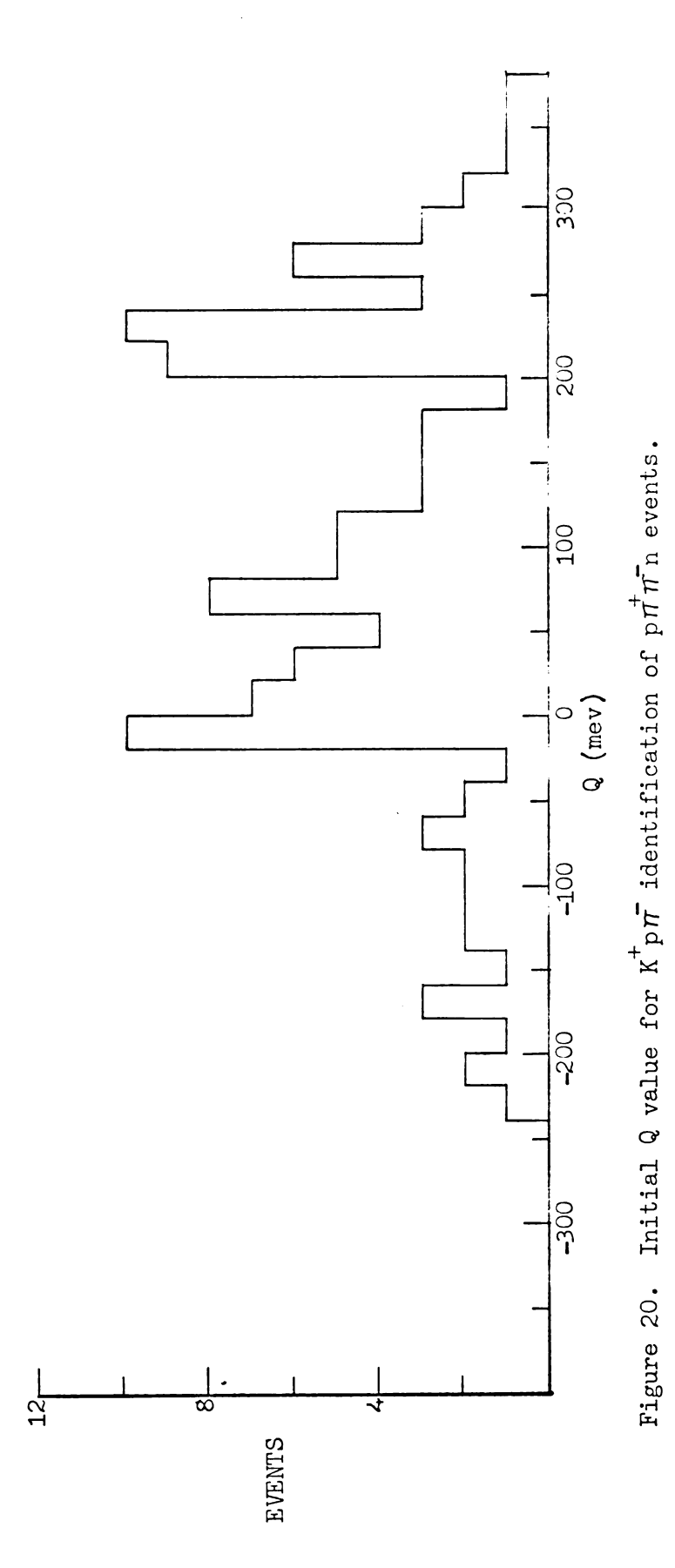
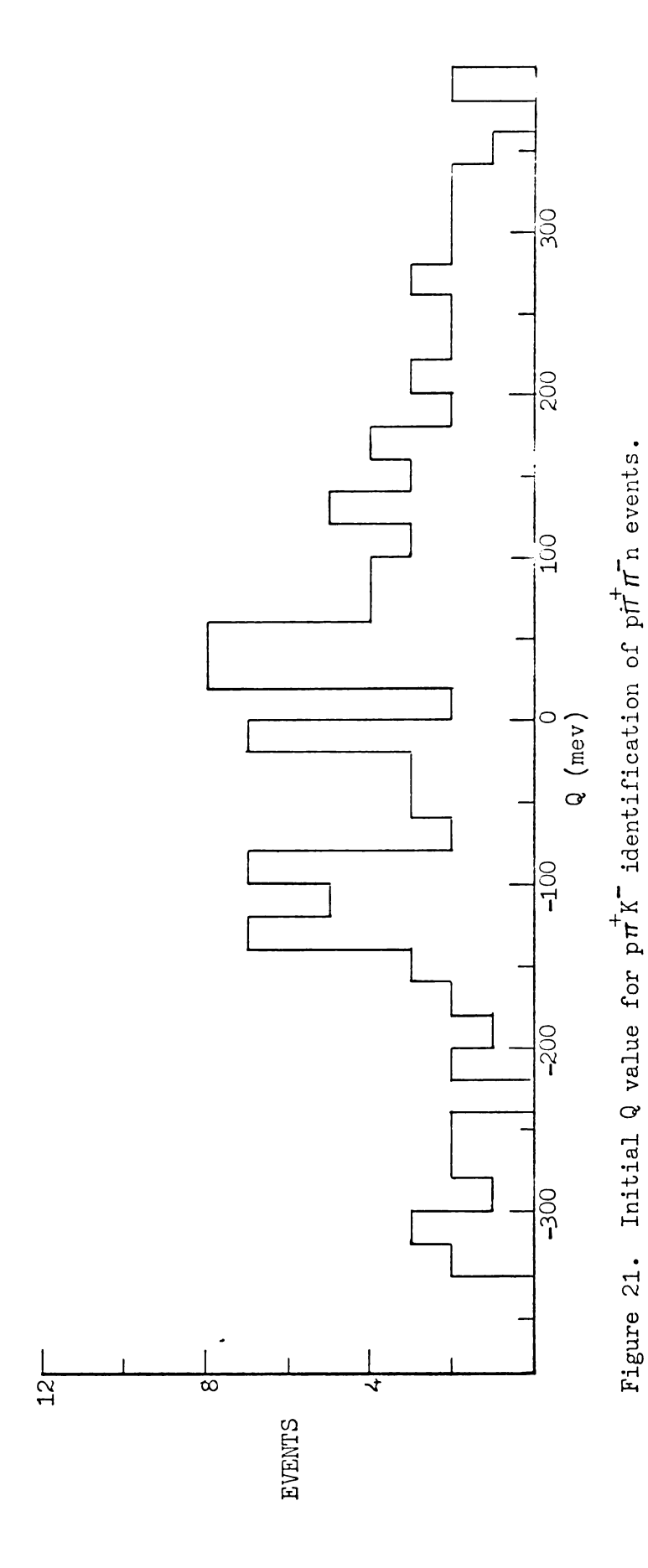
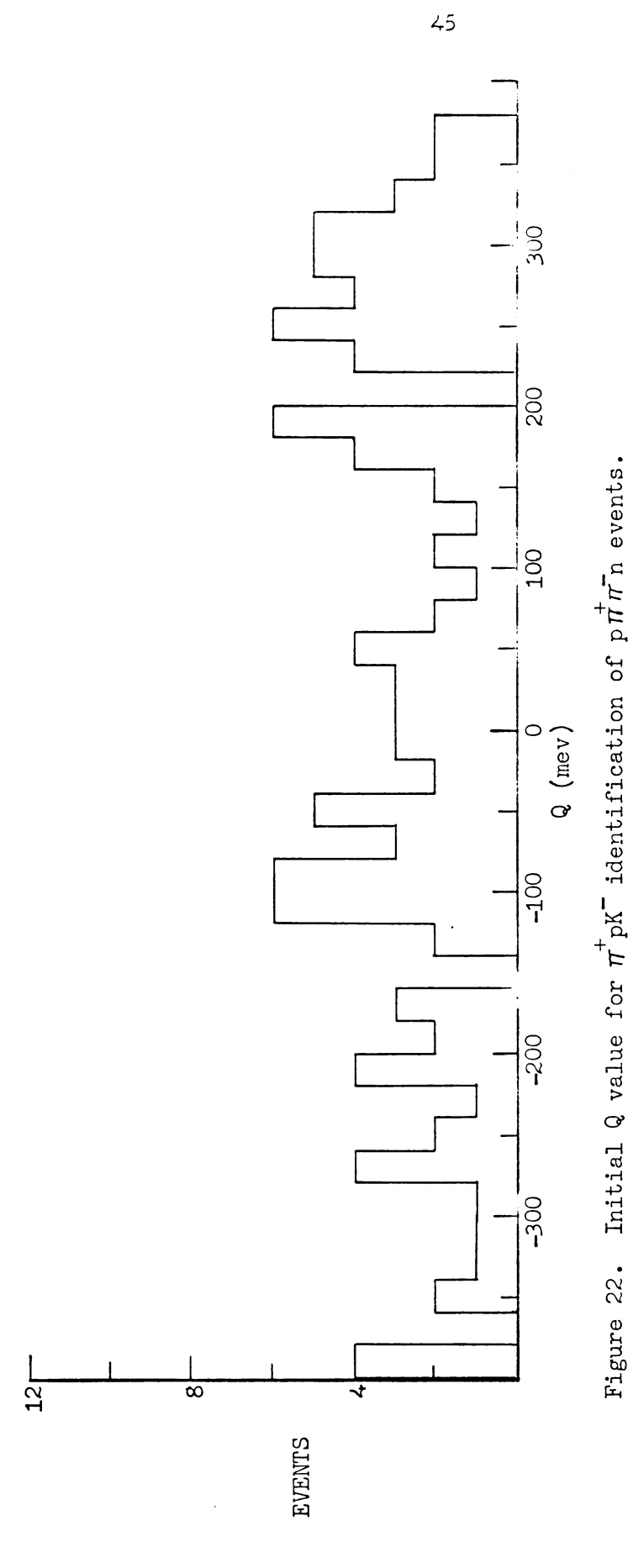


Figure 19. Initial Q value for $pK^{+}\pi^{-}$ identification of $p\pi^{+}\pi^{-}$ n events.







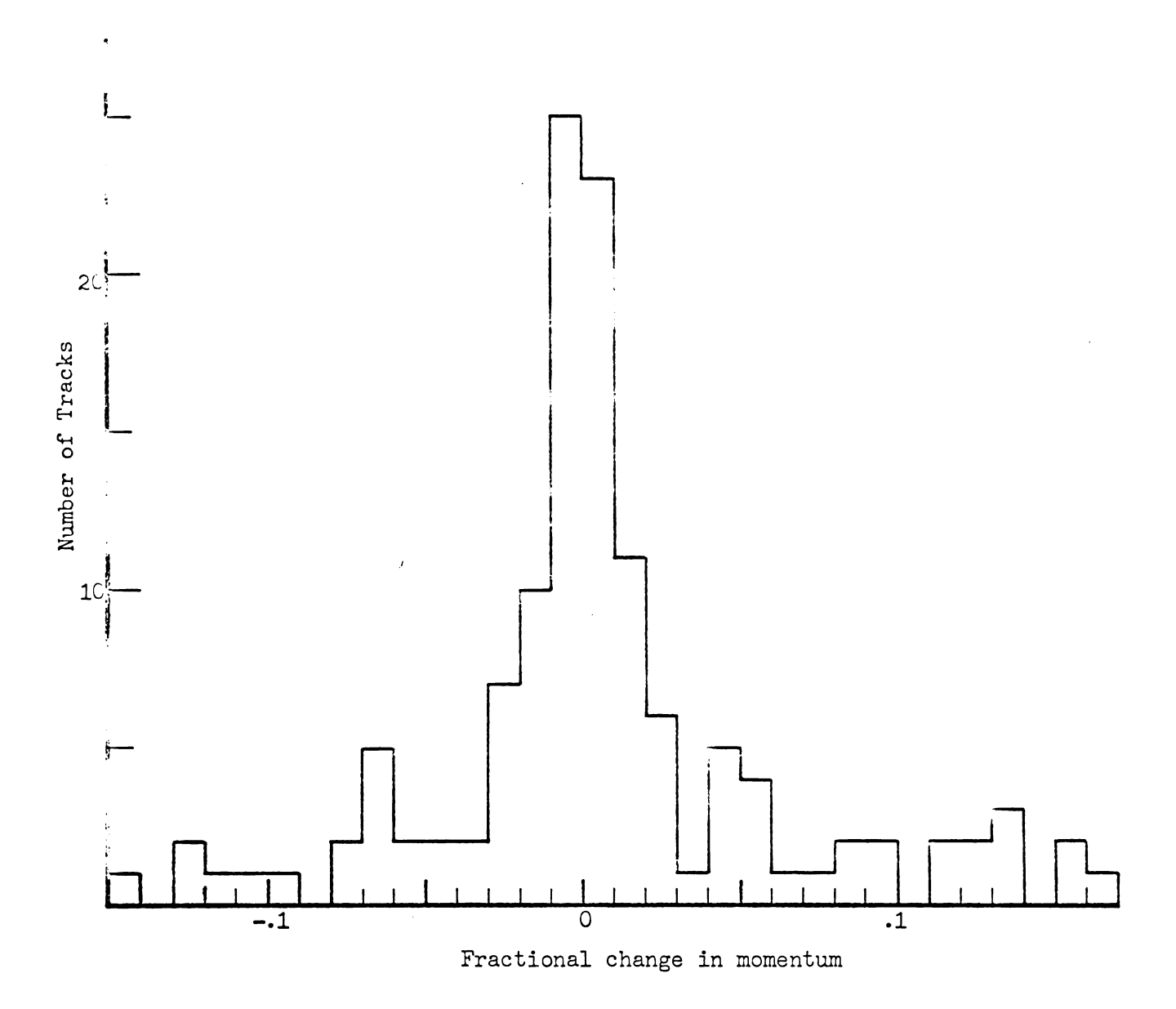


Figure 23. Fractional change in momentum made by QEVAL.

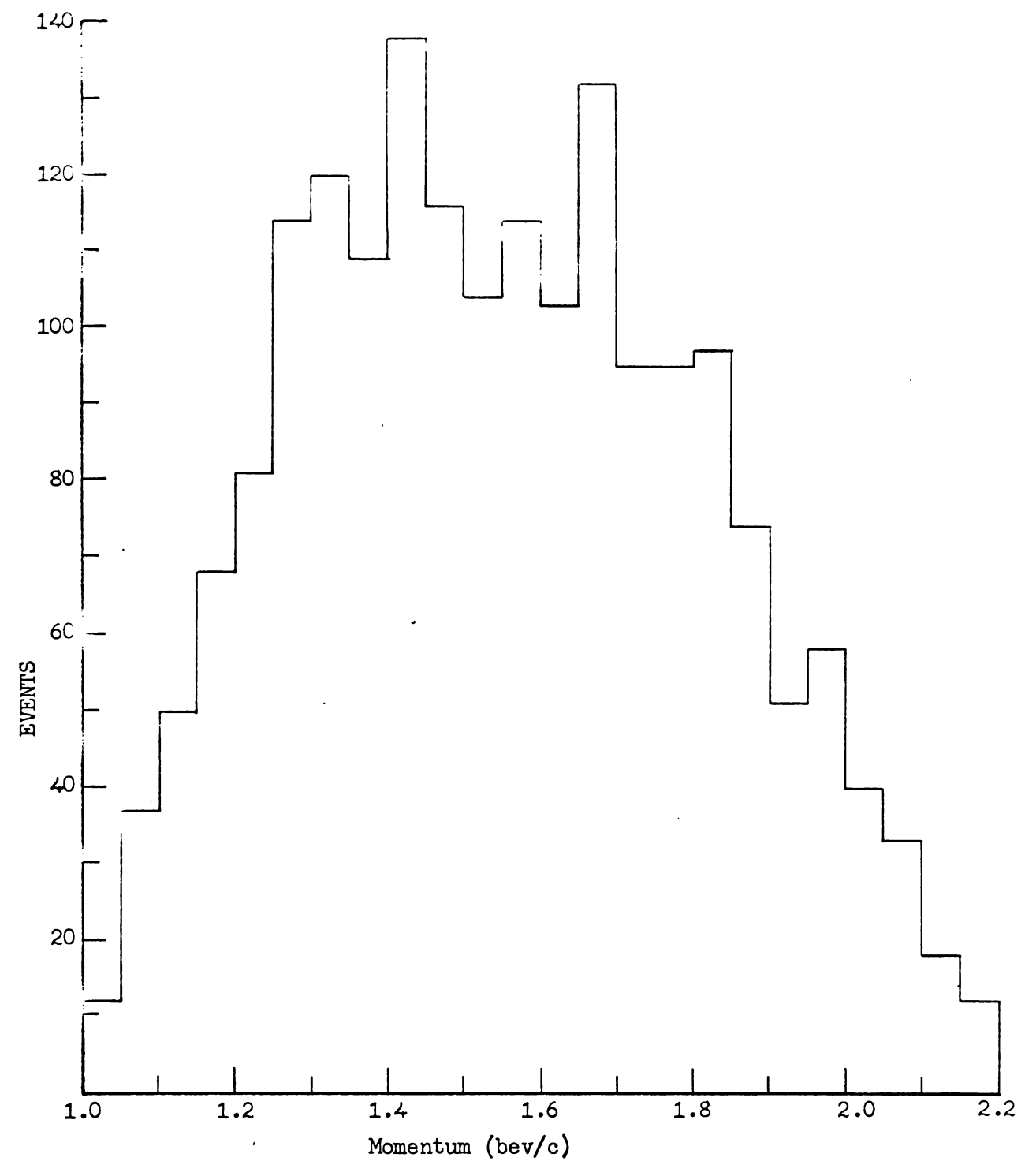


Figure 24. Neutron lab momentum of $pp\pi^-$ events.

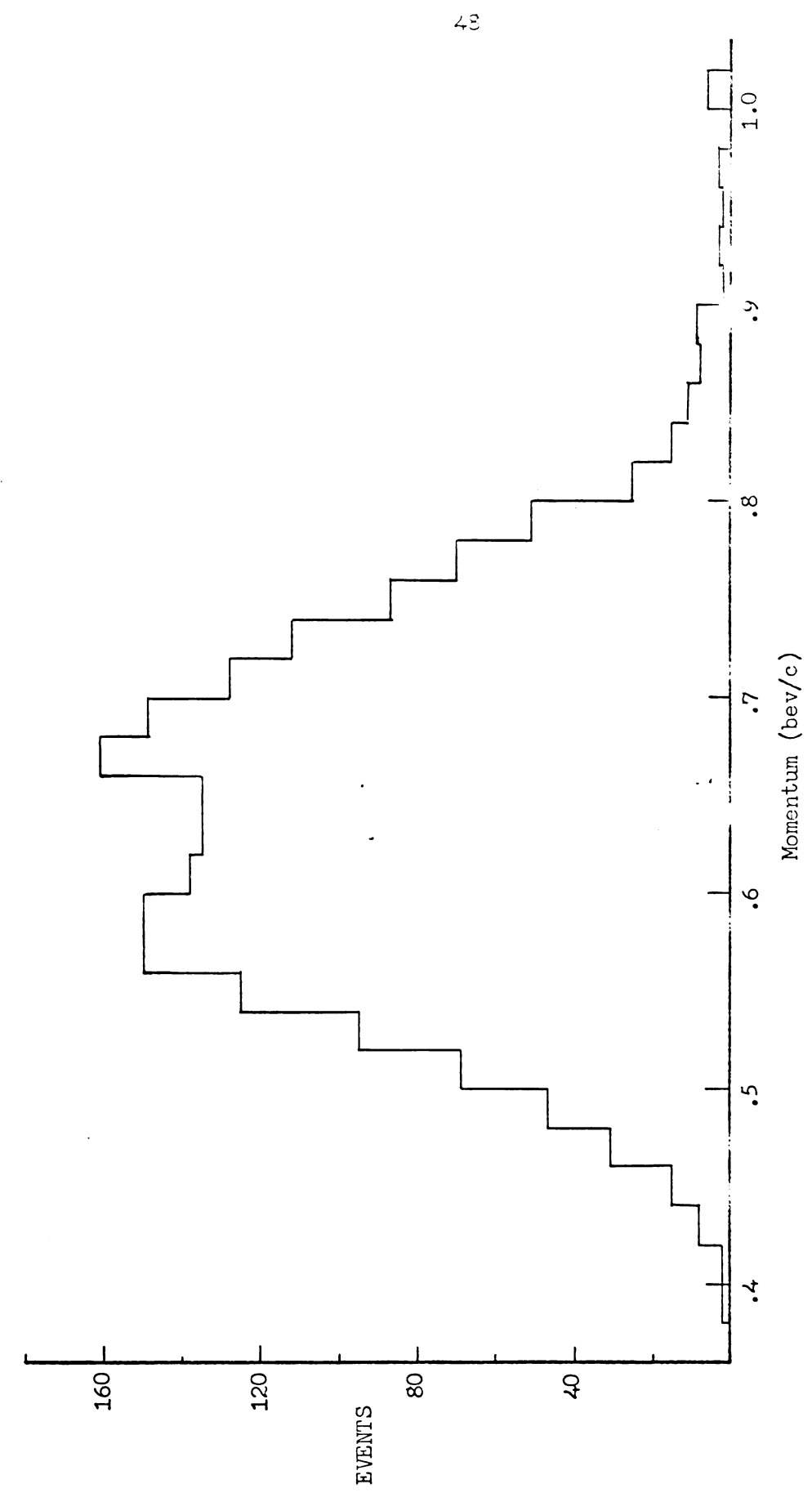


Figure 25. Neutron center of mass momentum of ppm events.

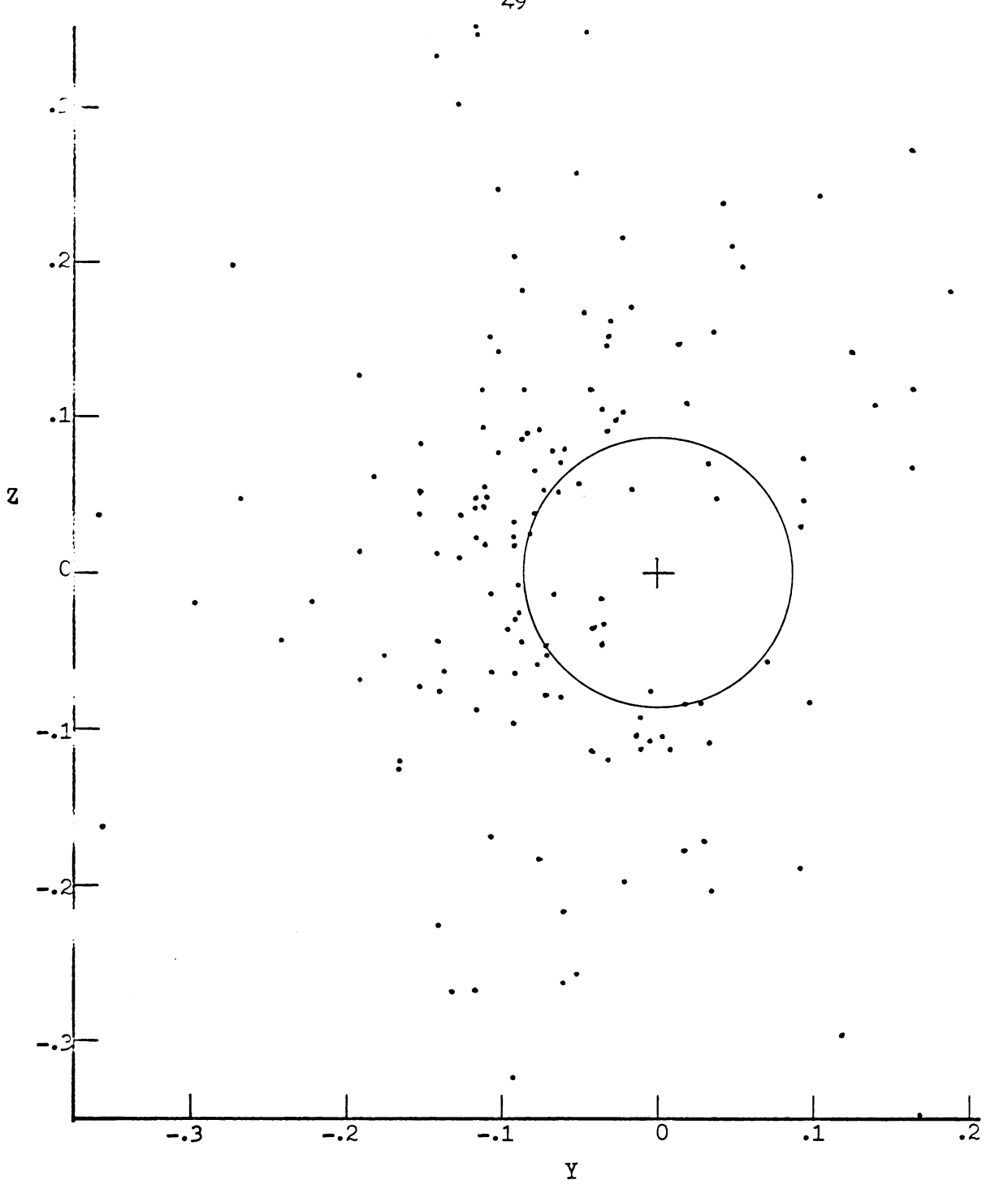


Figure 26. Scatter plot of Y and Z direction cosines of the beam particle of apparent ppm events whose adjusted beam angle was greater than 5°. The circle represents 5°.

The minus Y direction is up, and the plus Z direction is toward the back window.

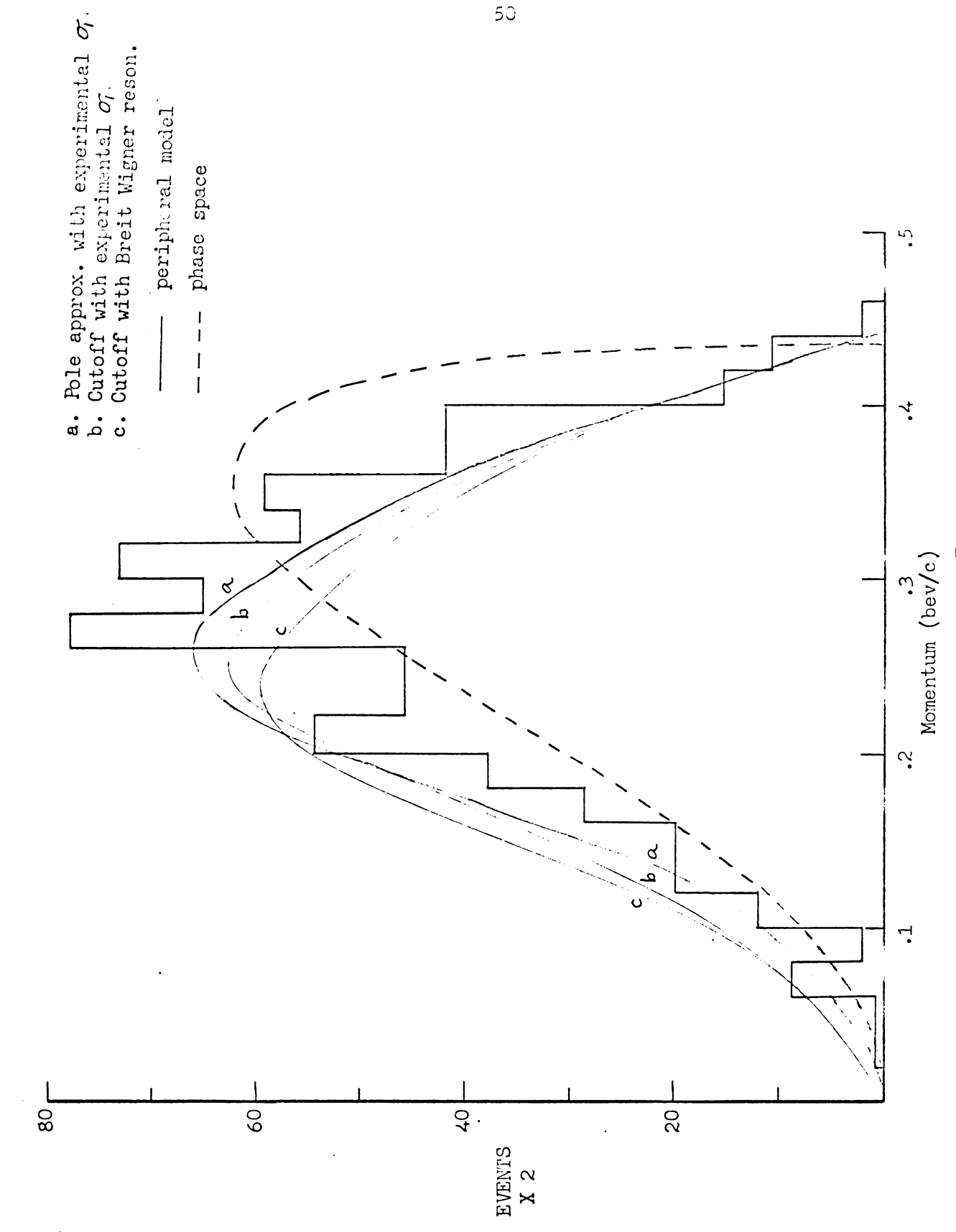


Figure 27. Proton center of mass momentum: 361 pp \vec{r} events with 1.28 < P₀ < 1.43 bev/c.

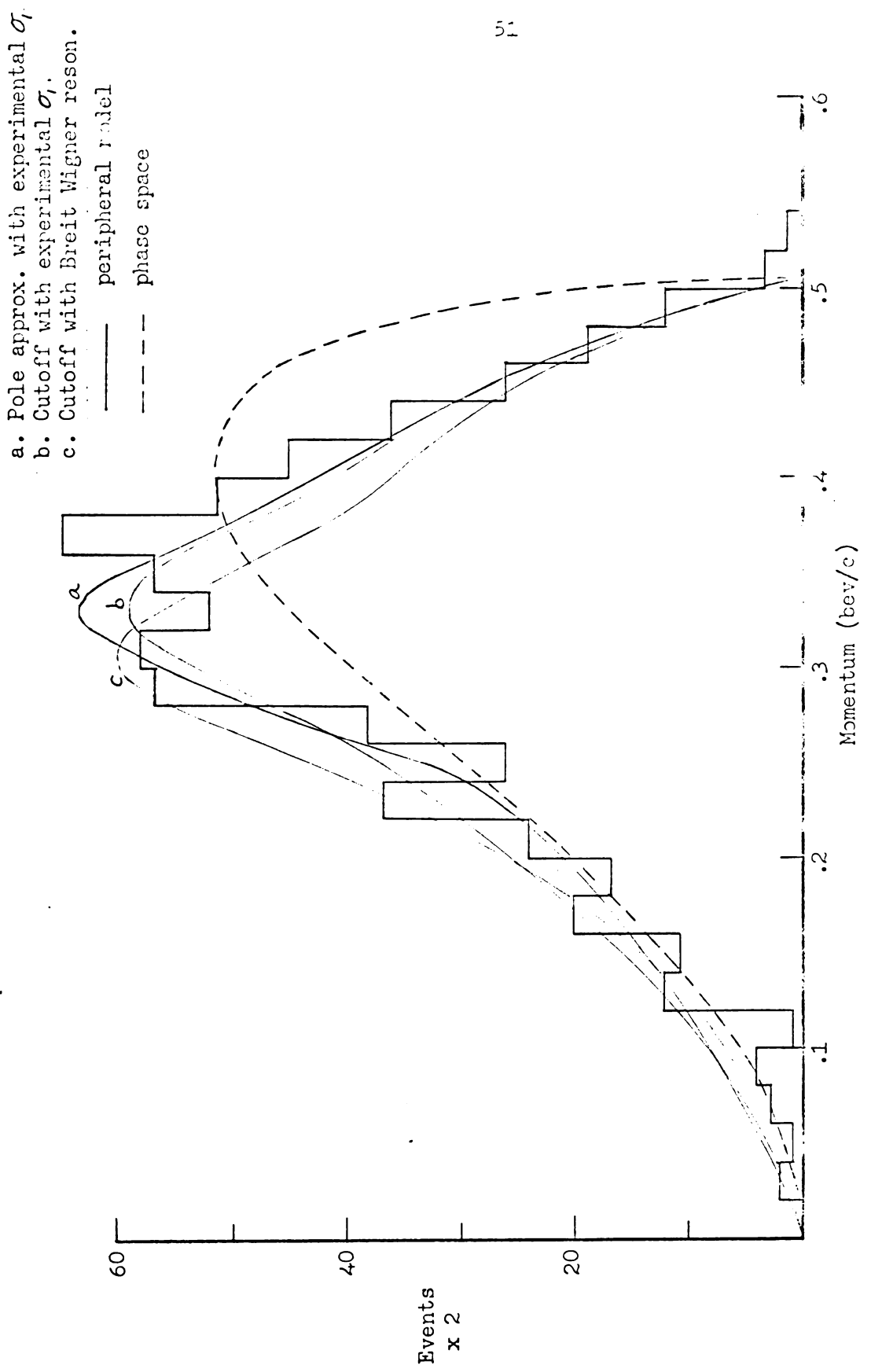


Figure 28. Proton center of mass momentum: 339 pp \vec{n} events with 1.43 < Po < 1.58 bev/c.

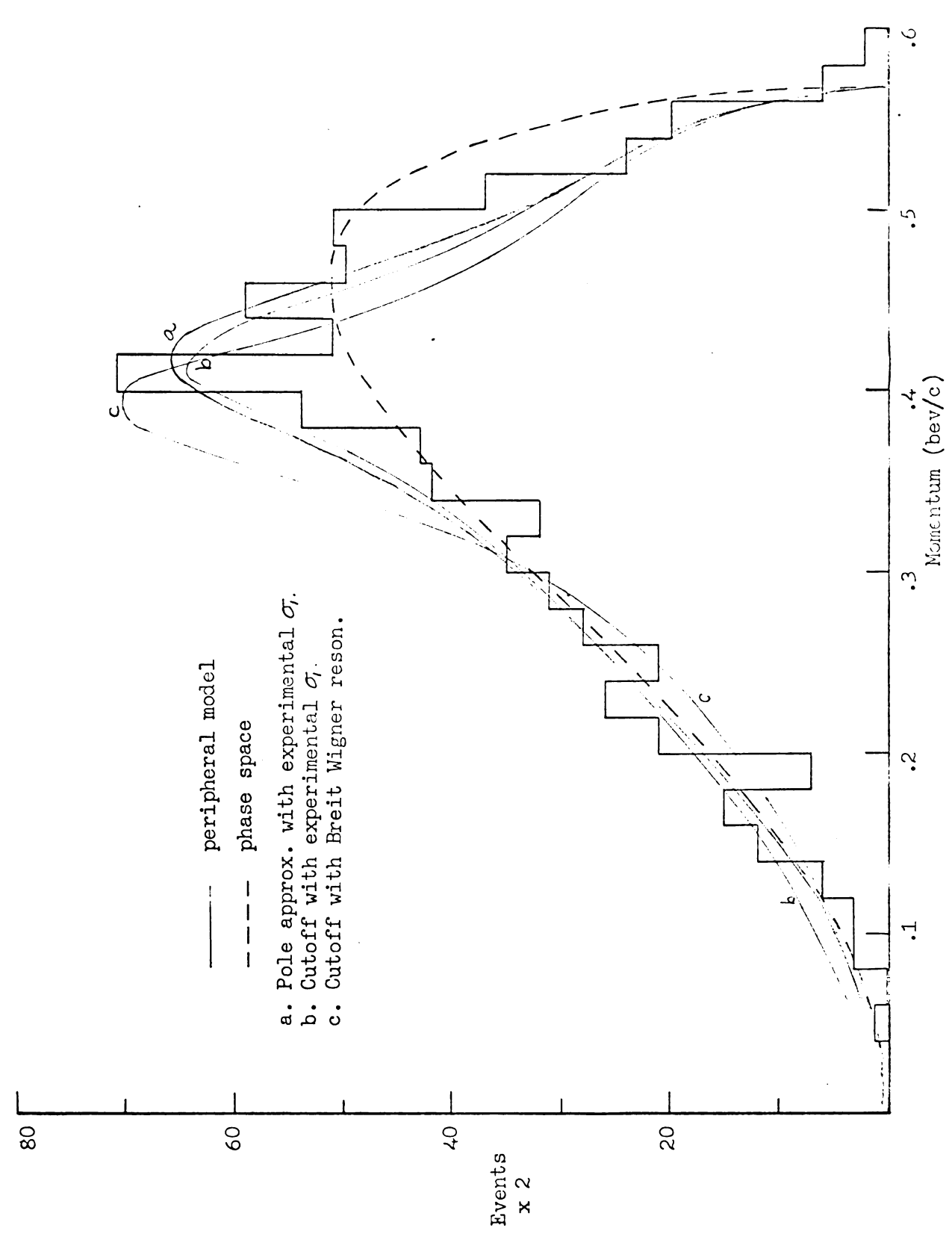


Figure 29. Proton center of mass momentum: 378 pp \vec{r} events with 1.58 < P₀ < 1.75 bev/c.

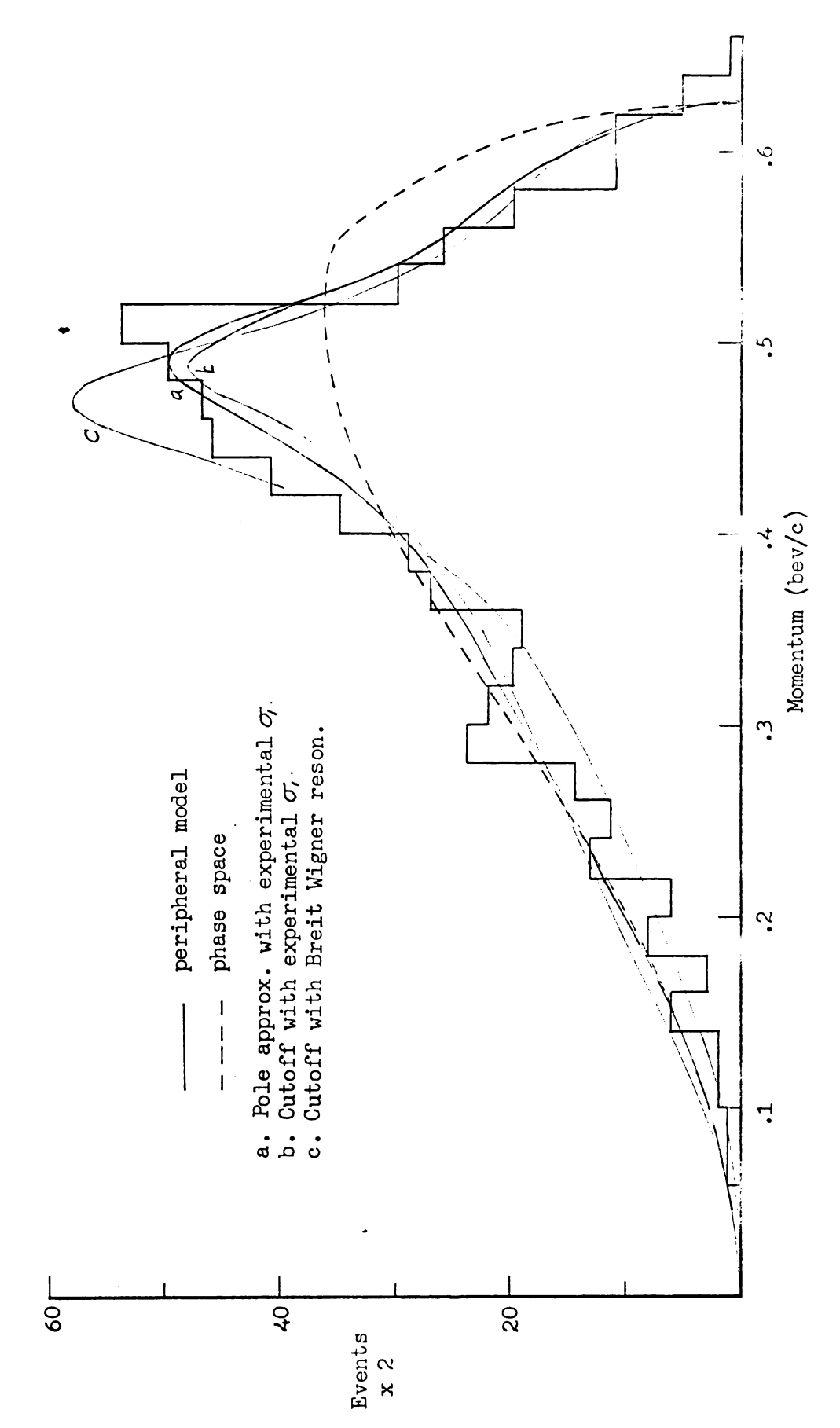


Figure 30. Proton center of mass momentum: 294 pp \vec{r} events with 1.75 < P_0 < 1.92 bev/c.

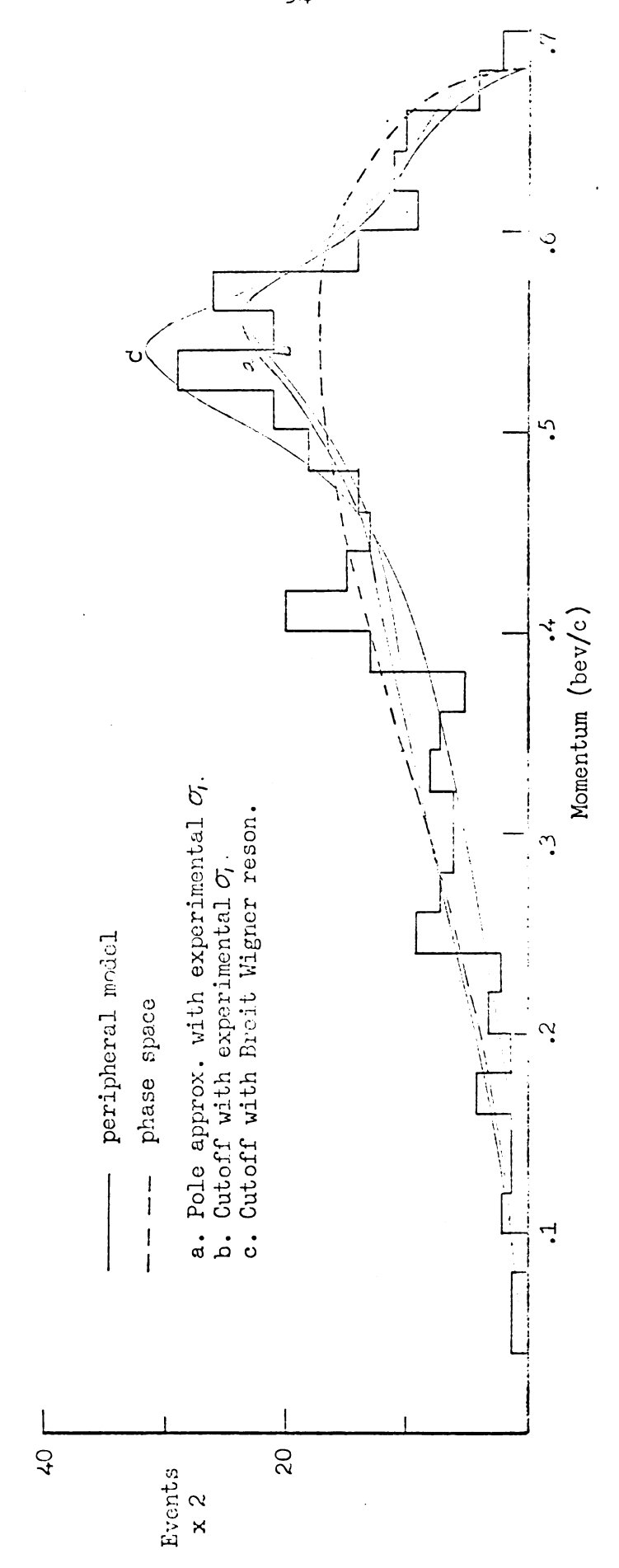


Figure 31. Proton center of mass momentum: 152 pp \vec{r} events with 1.92 < P_0 < 2.10 bev/c.

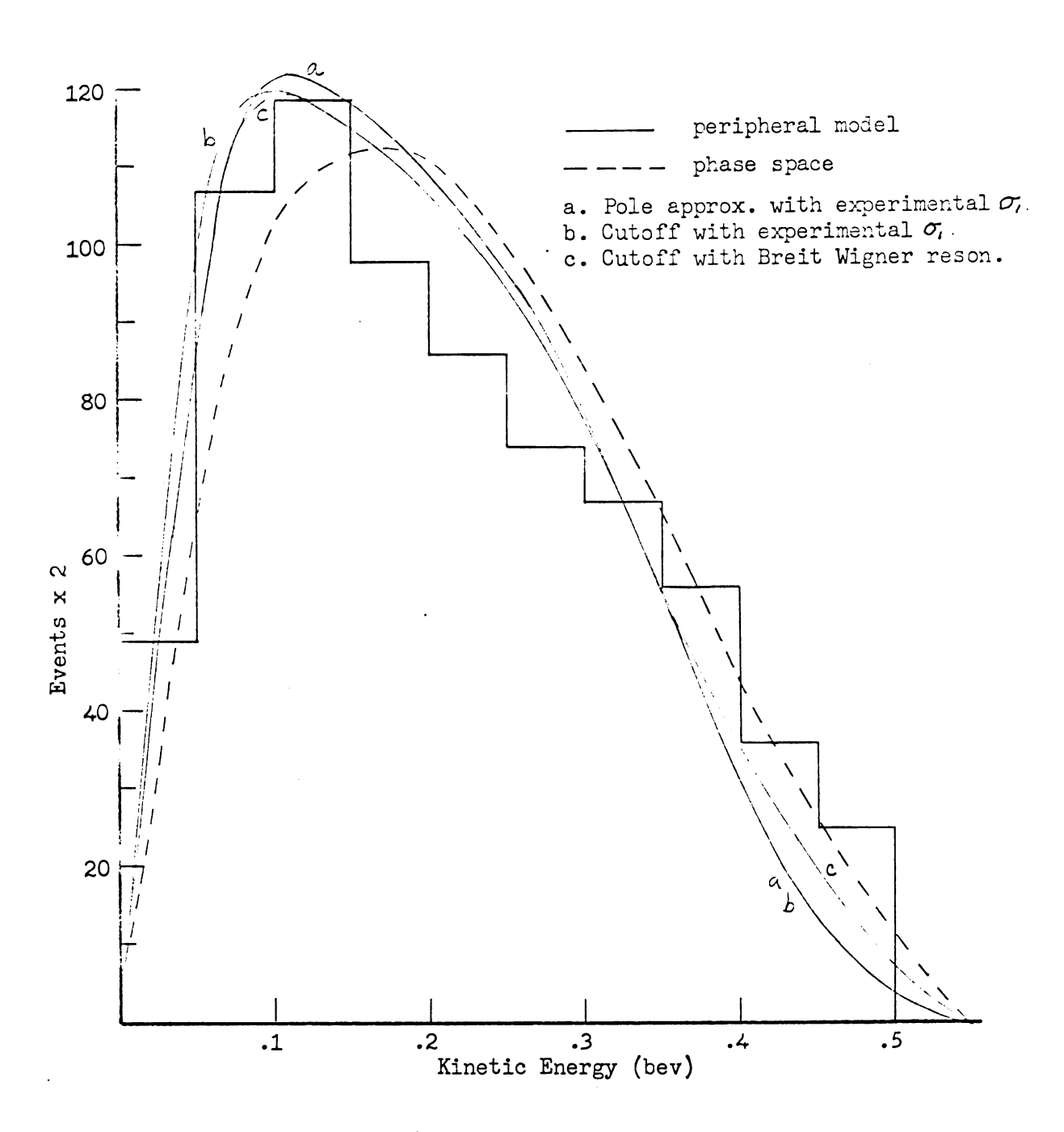


Figure 32. Proton lab kinetic energy; 361 pp π^- events with 1.28 < Po < 1.43 bev/c.

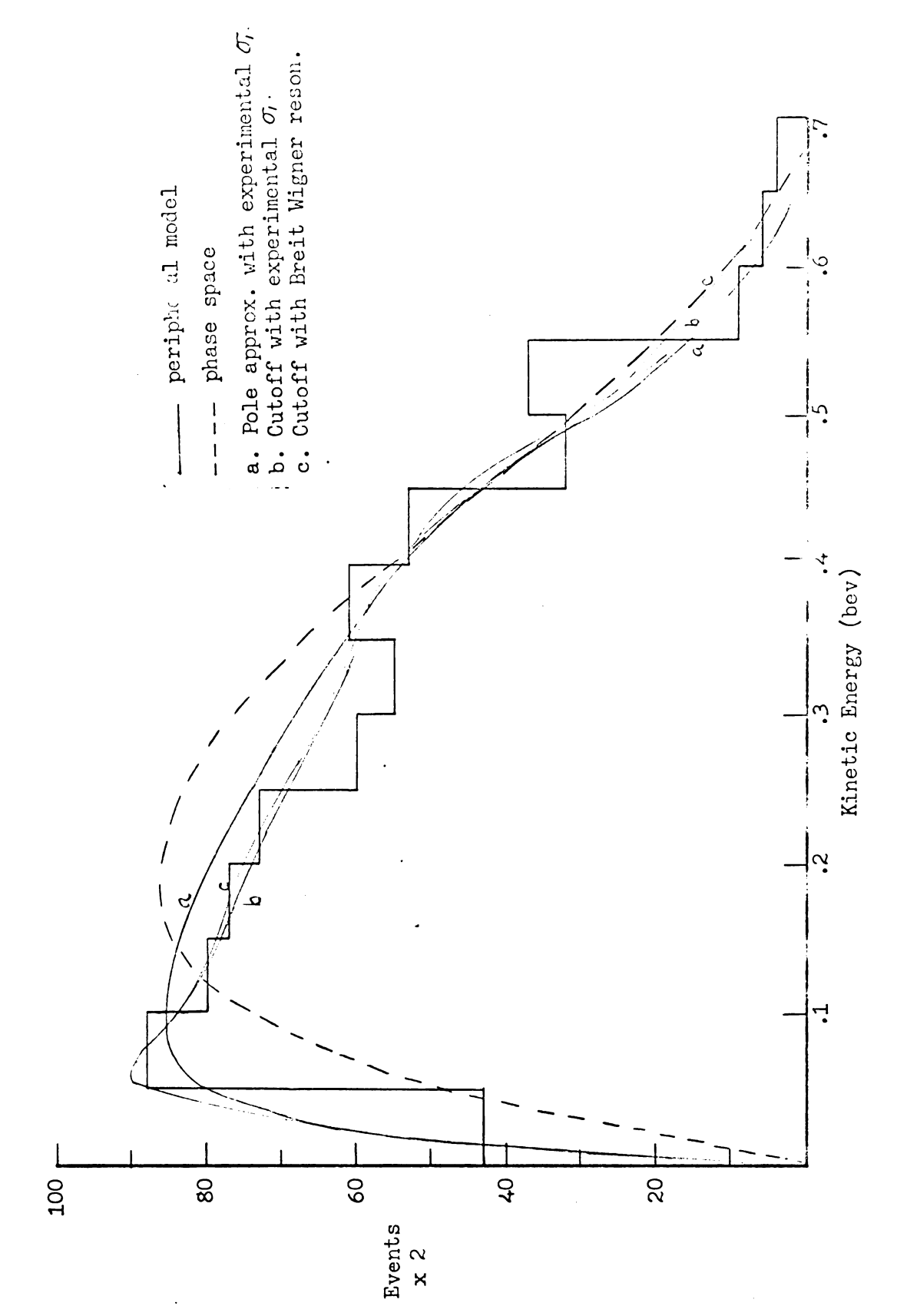
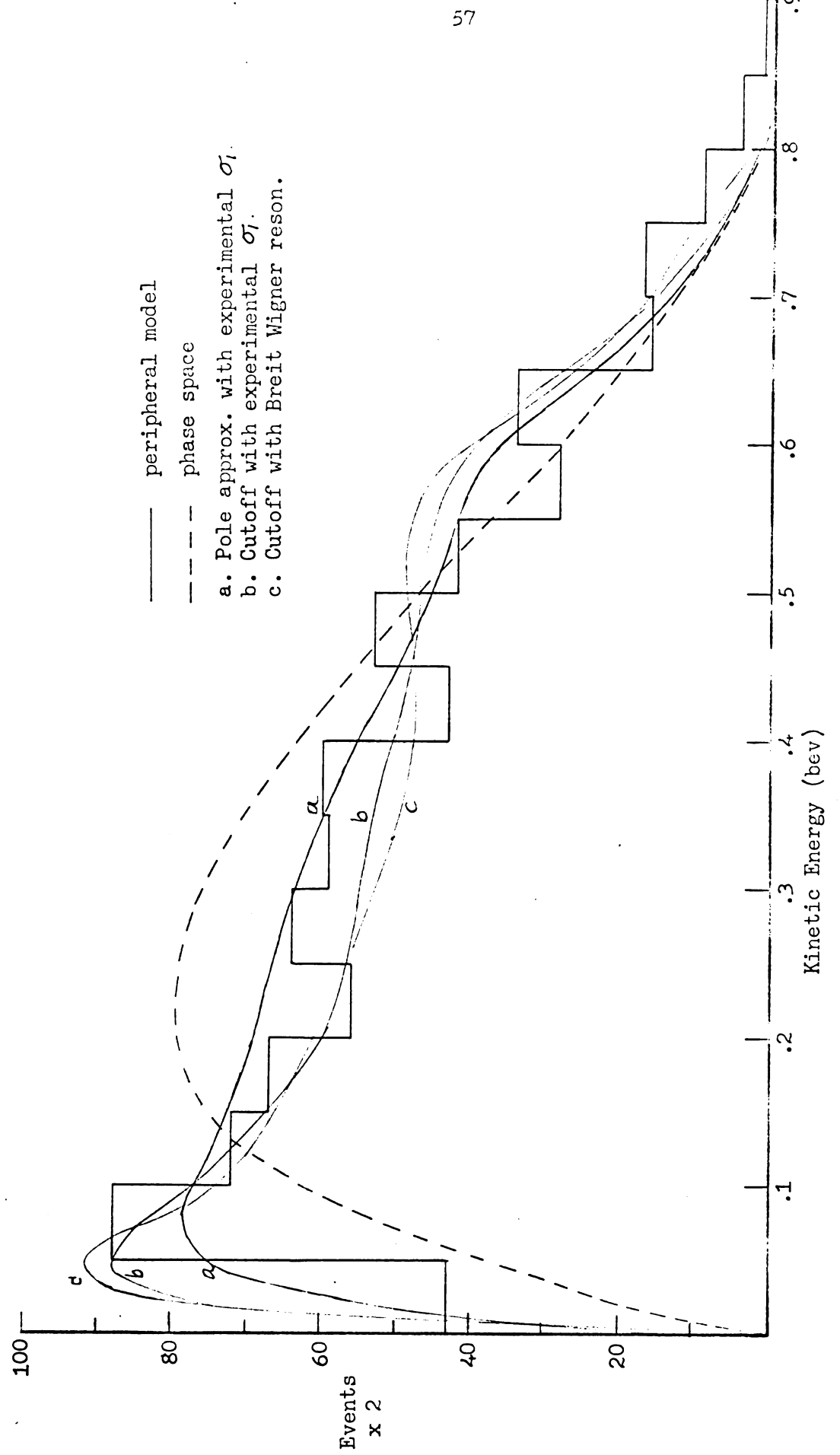


Figure 33. Proton lab kinetic energy; 339 ppm events with 1.43 < $P_0 < 1.53$ be://...

		,
		•
		•
		•
		,





Proton lab kinetic energy; 378 ppm events with 1.58 < Po < 1.75 bev/c. Figure 34.

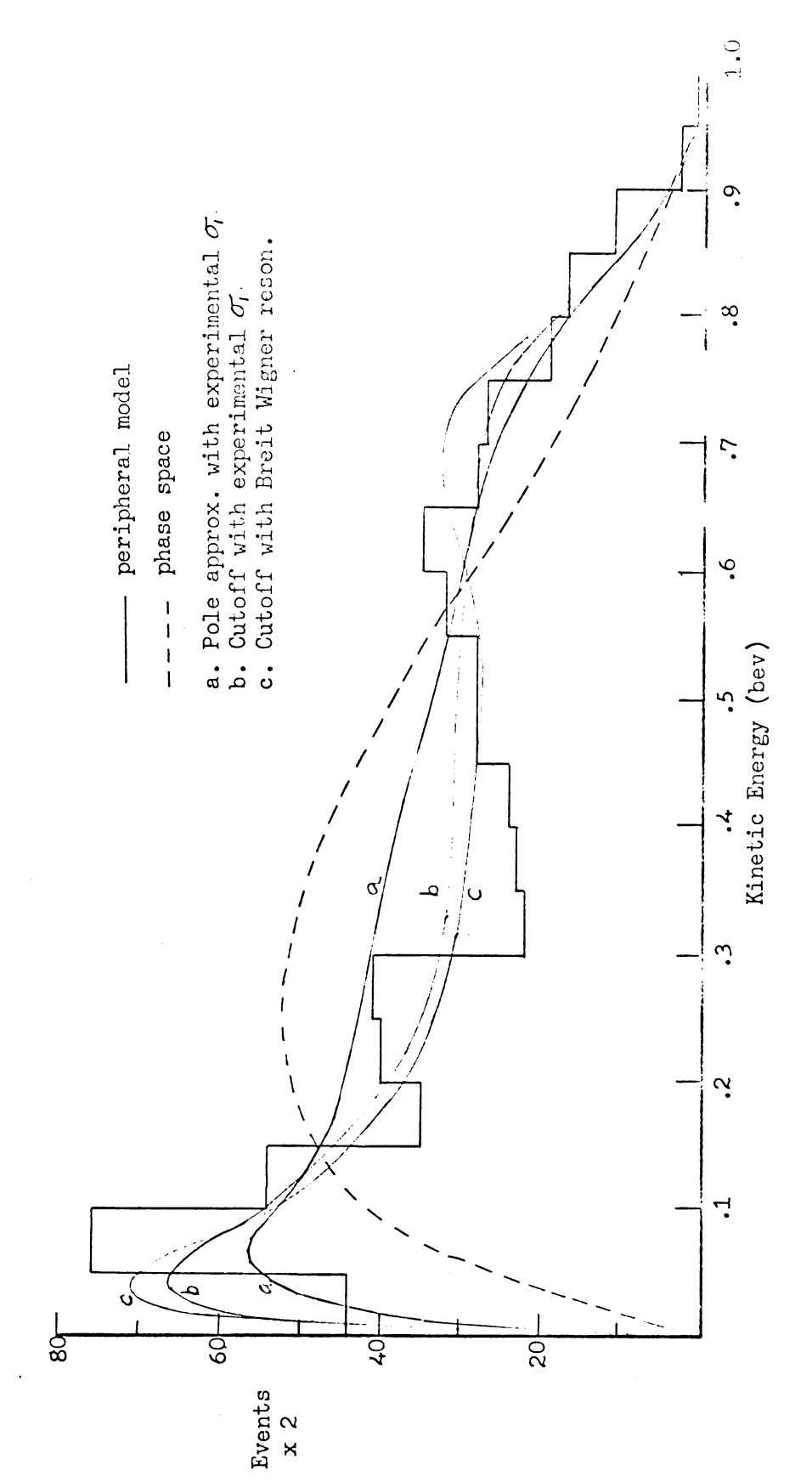


Figure 35. Proton lab kinetic energy; 294 pp \vec{r} events with 1.75 < Po < 1.92 Fey/s.

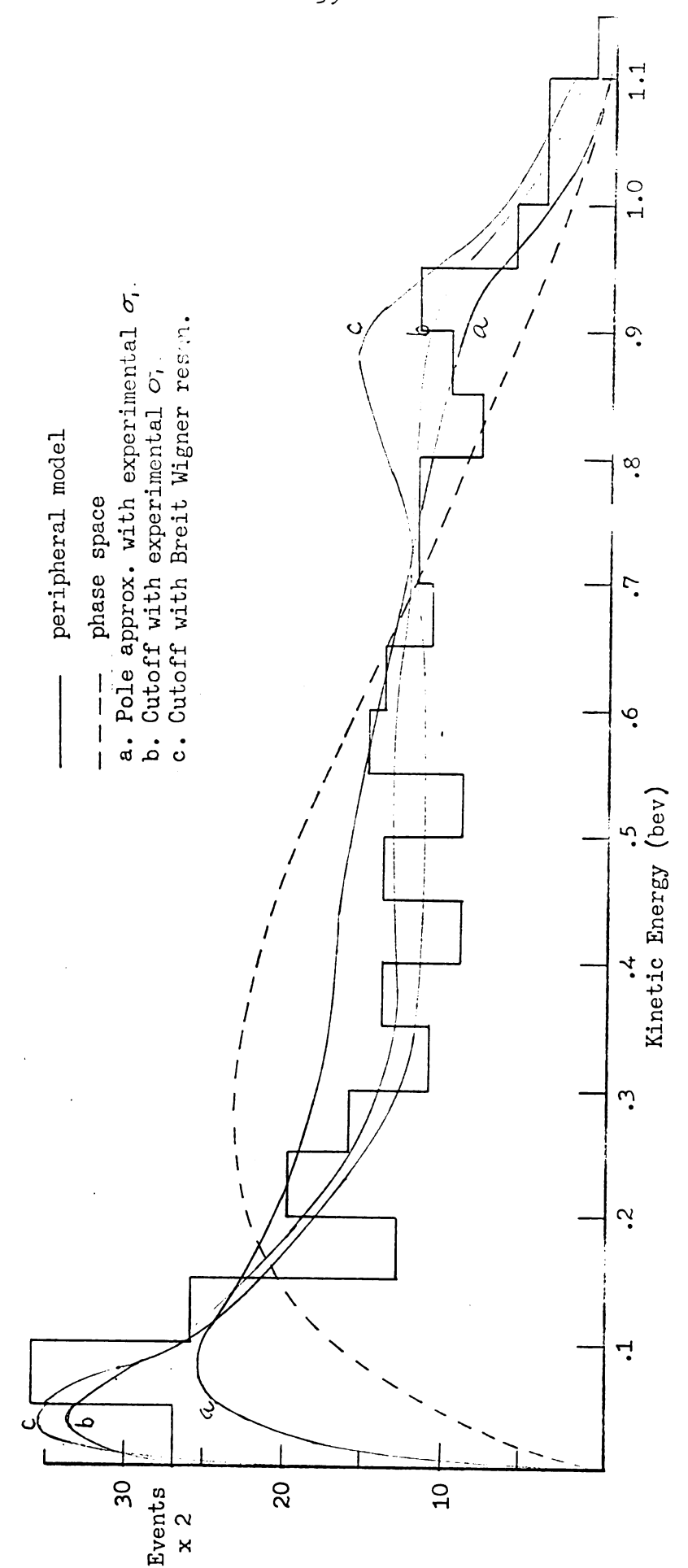


Figure 36. Proton lab kinetic energy; 152 pp \vec{r} events with 1.92 < Po < 2.10 bev/c.

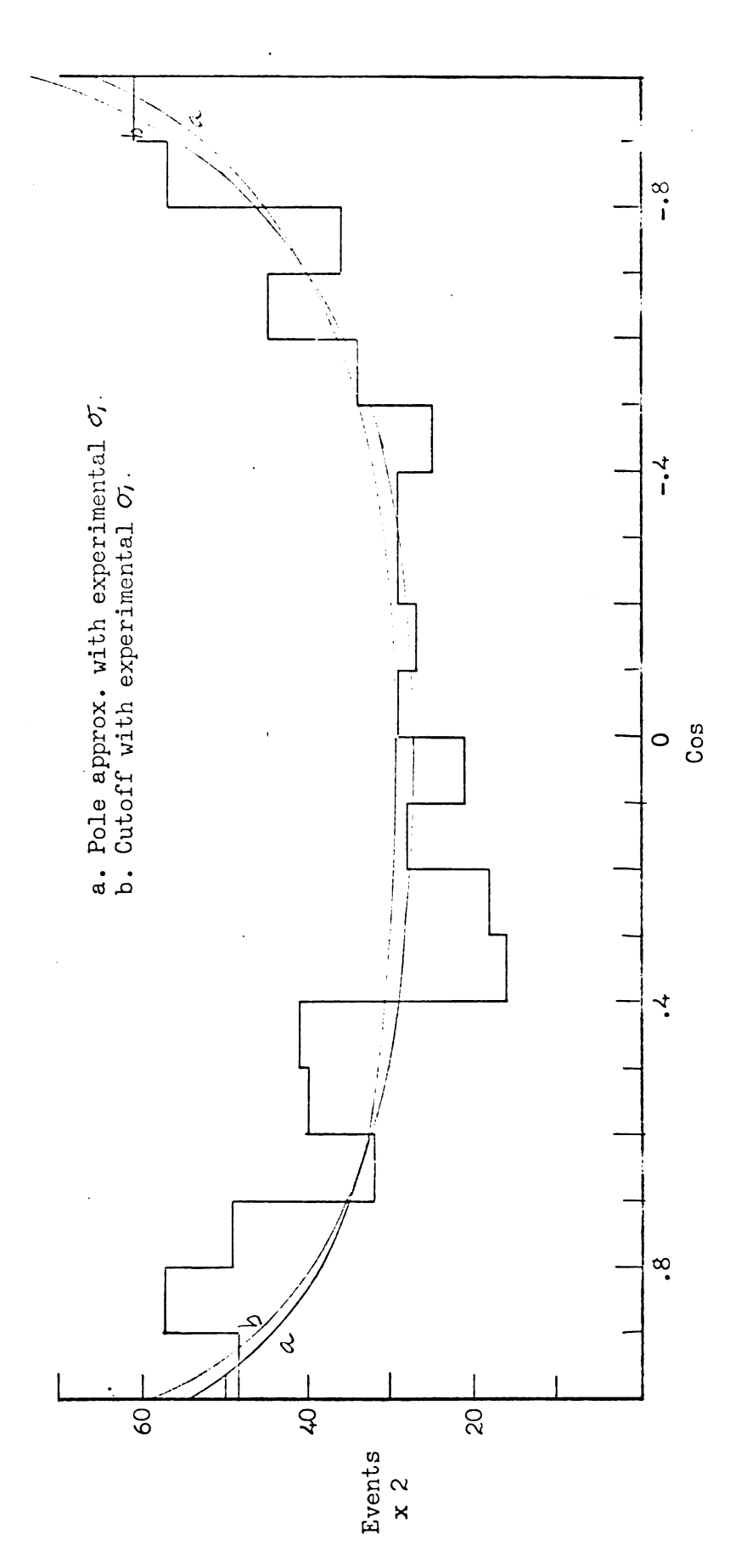
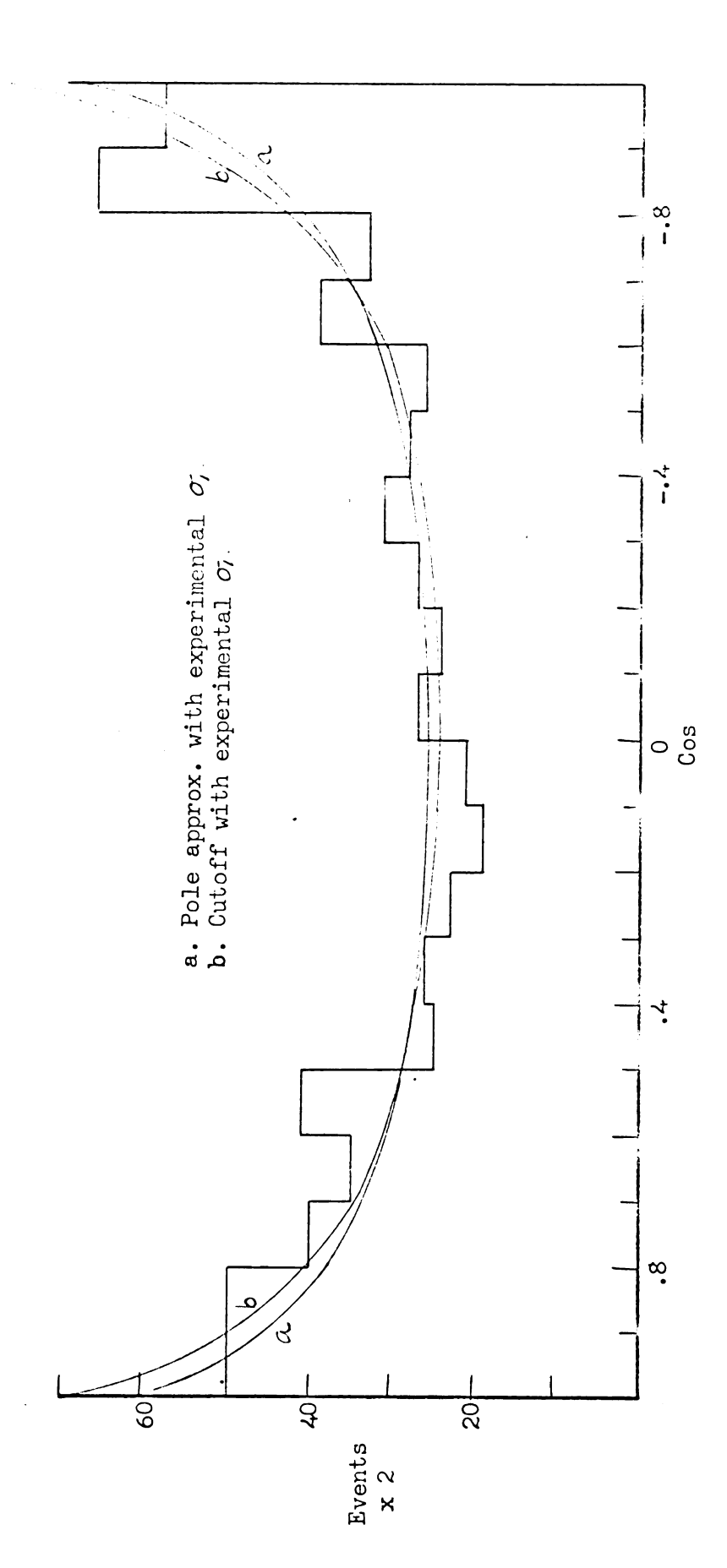


Figure 37. Proton center of mass angular distribution; 361 pp \vec{r} events with 1.23 < $\Gamma_0 < 1.43$ bev/c.



Proton center of mass angular distribution; 339 ppm events with 1.43 < $P_0 < 1.58~{\rm key/c}$. Figure 38.

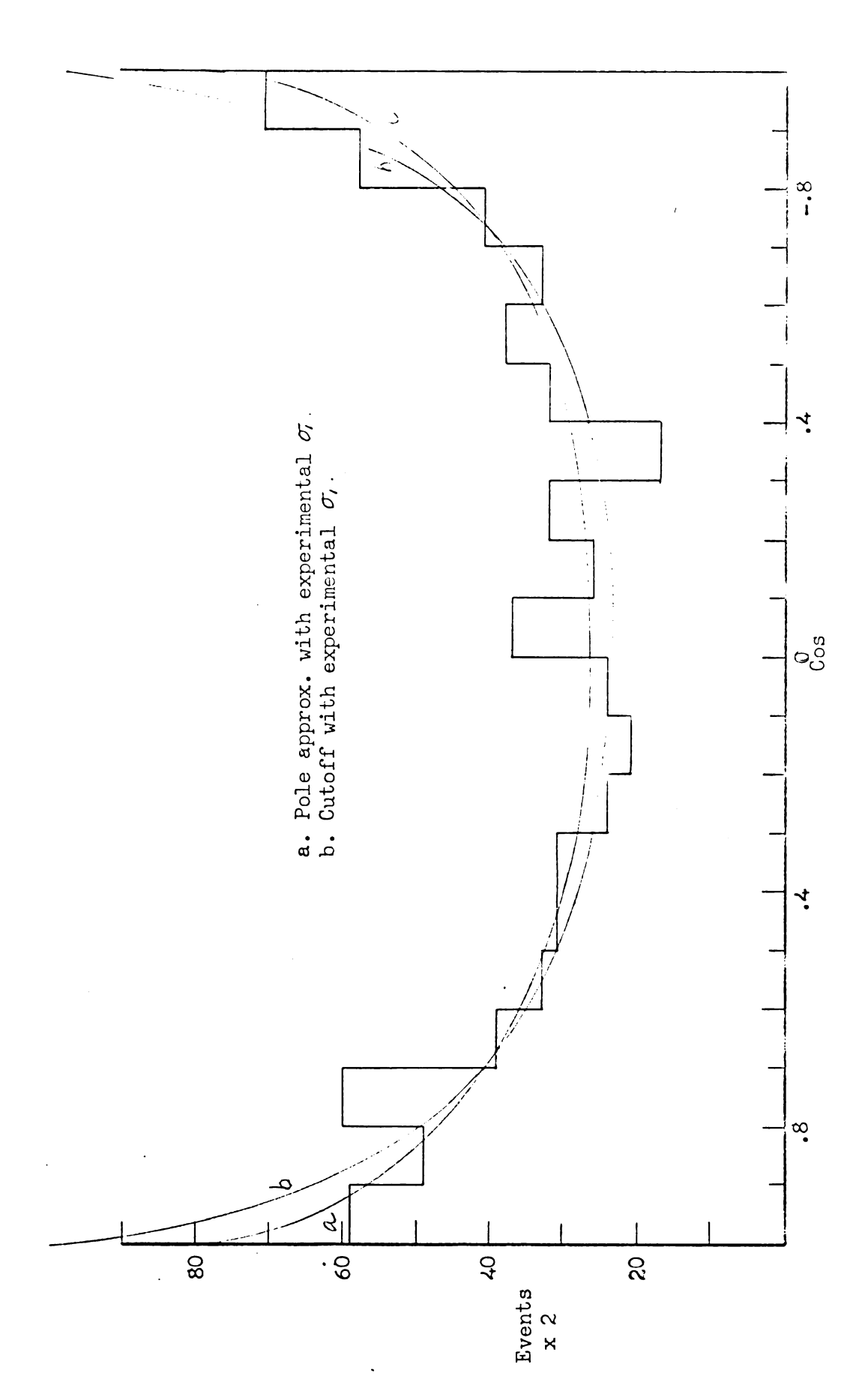


Figure 39. Proton center of mass angular distribution; 378 ppm events with 1.53 < $P_0 < 1.77 \pm 87/c$.

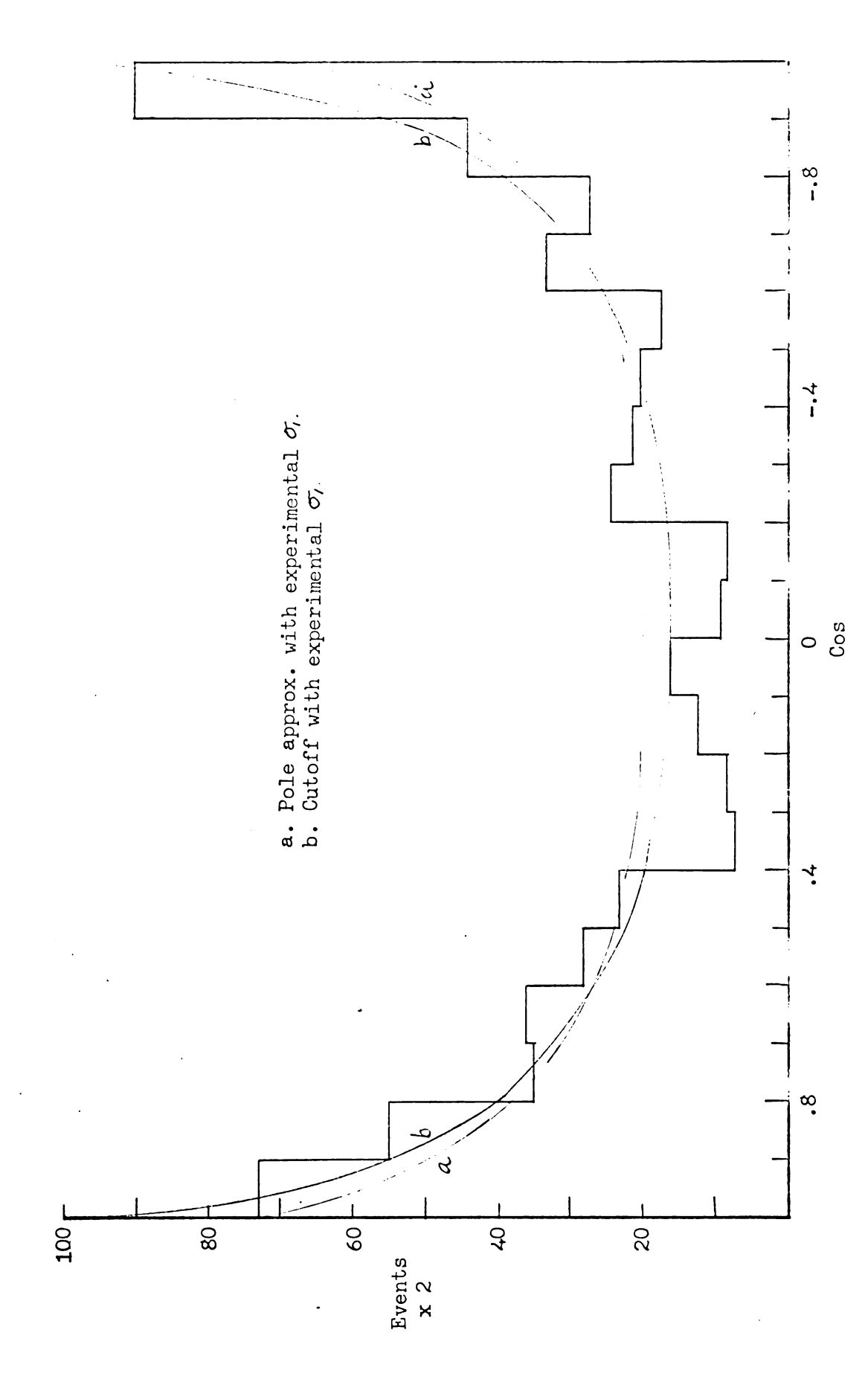


Figure 40. Proton center of mass angular distribution; 294 ppm events with 1.75 < P_0 < 1.92 bev/c.

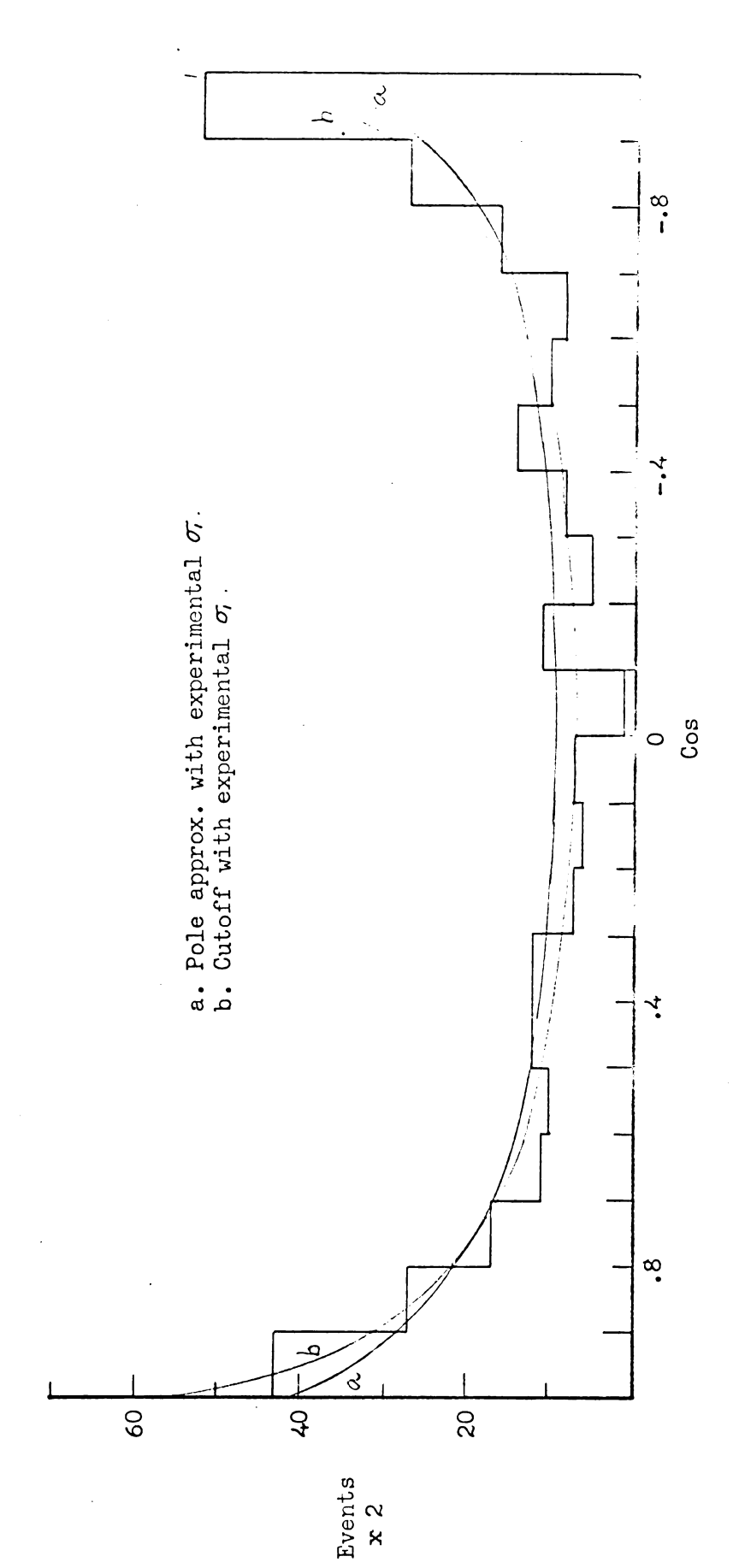
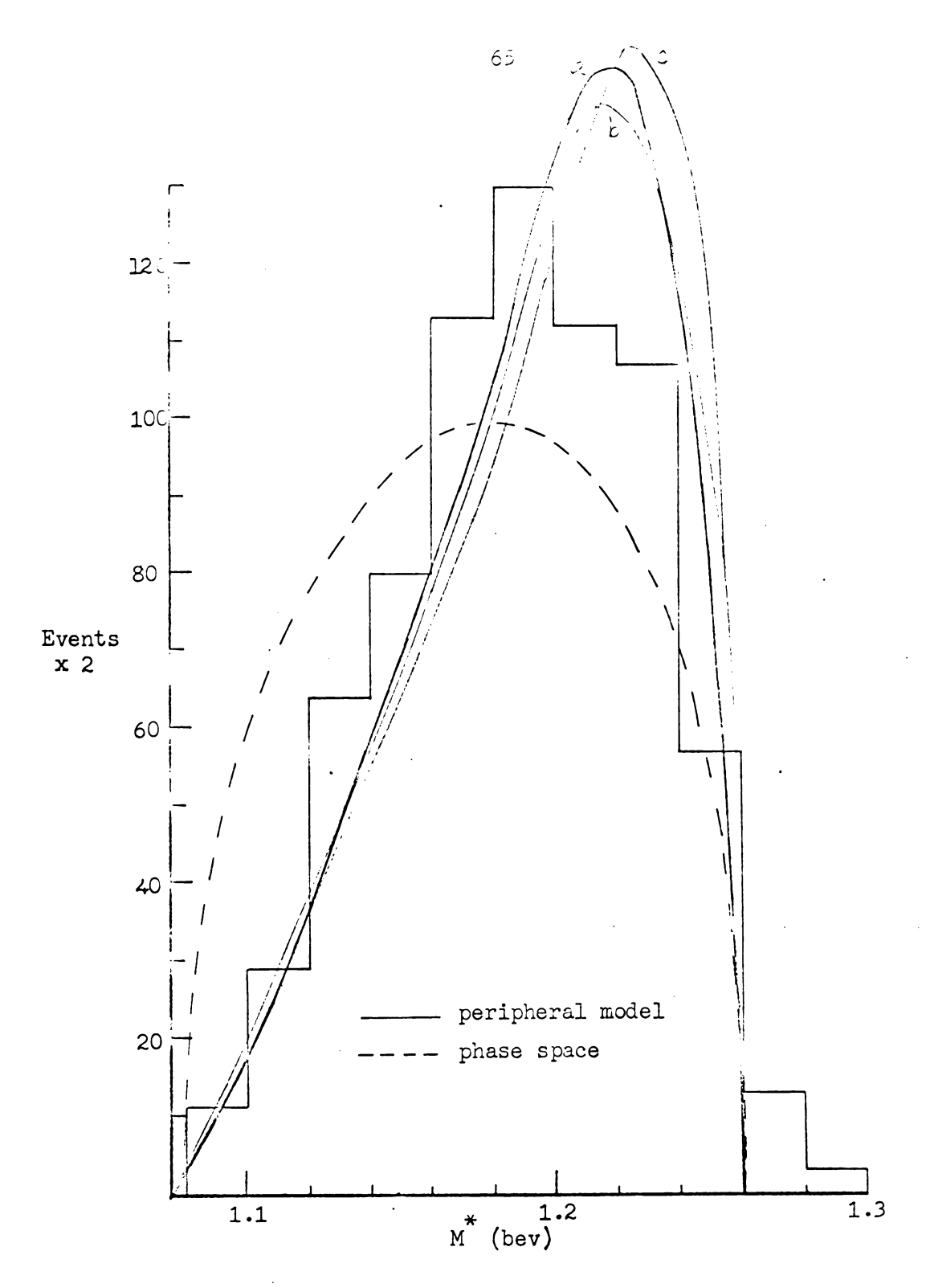


Figure 41. Proton center of mass angular distribution; 152 pp $\vec{\mathbf{n}}$ events with 1.92 < Po < 2.10 beager.



 M^{*} of $p\pi^{-}$ combinations;

361 pp $\overline{\pi}$ events with 1.28 < Po < 1.43 bev/c.

- a. Pole approx. with experimental σ_i b. Cutoff with experimental σ_i
- c. Cutoff with Breit Wigner reson.

		; ; ; v
		•
		•

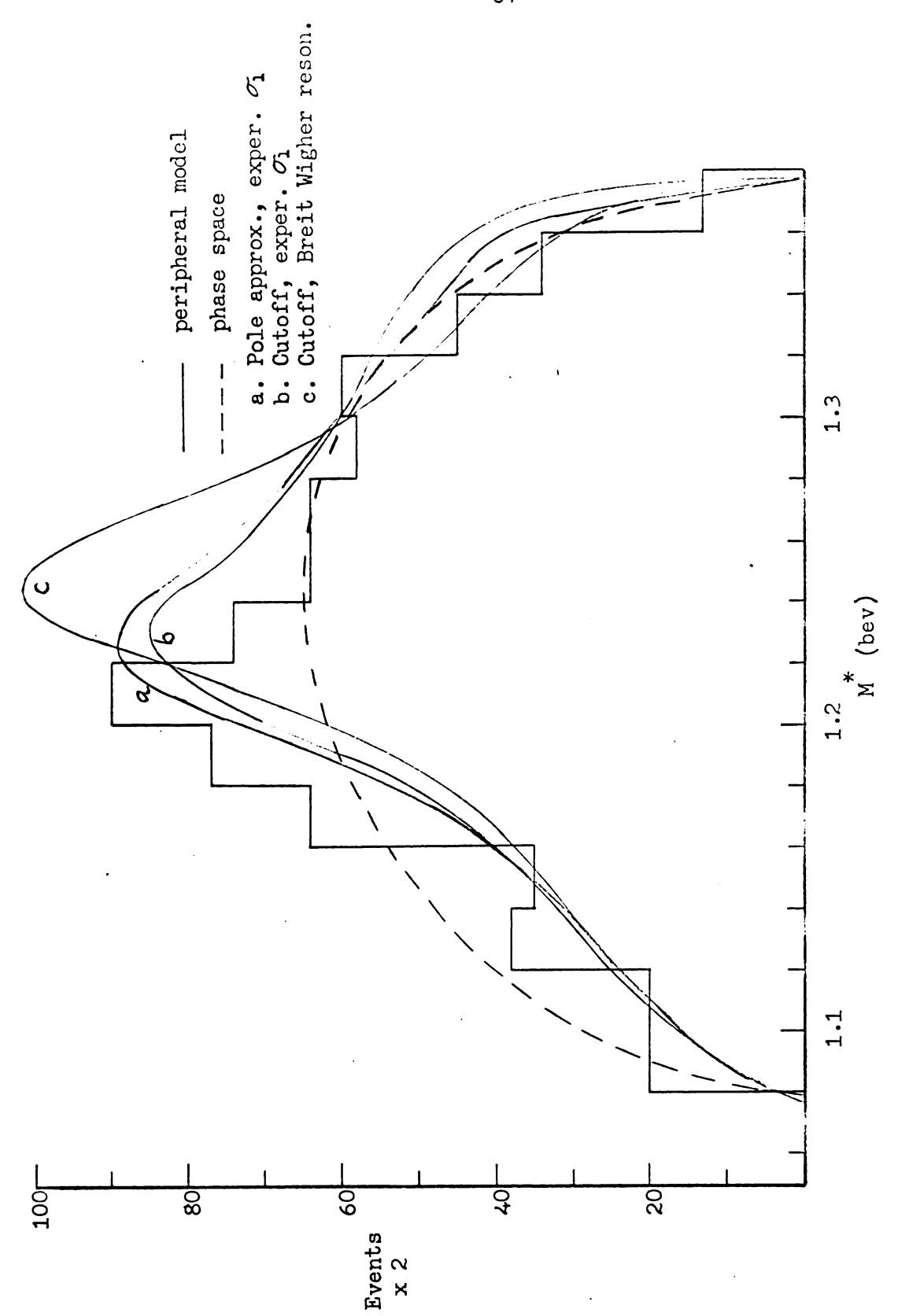


Figure 44. M of pm combinations; 378 ppm events with 1.58 < Po < 1.75 bev/c.

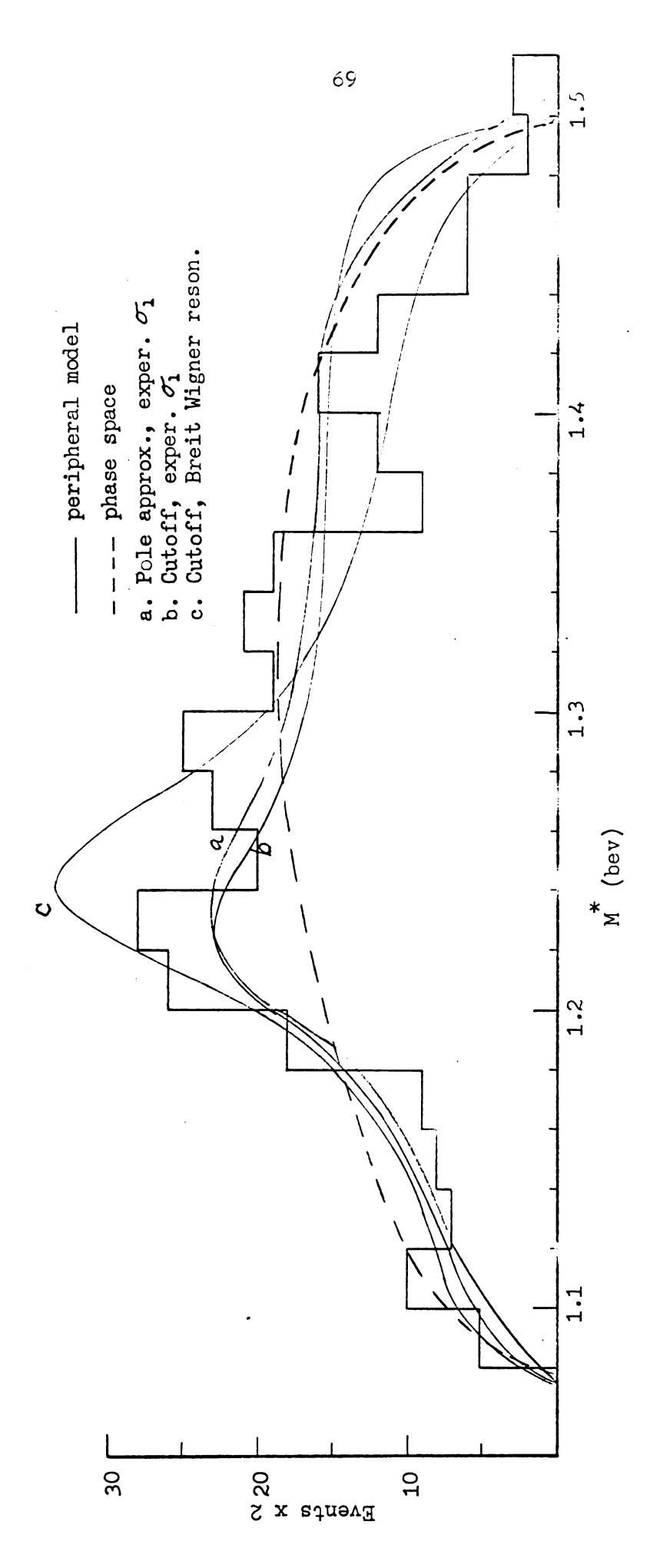


Figure 46. M of p π combinations; 152 pp π events with 1.92 < P₀ < 2.10 bcv/c.

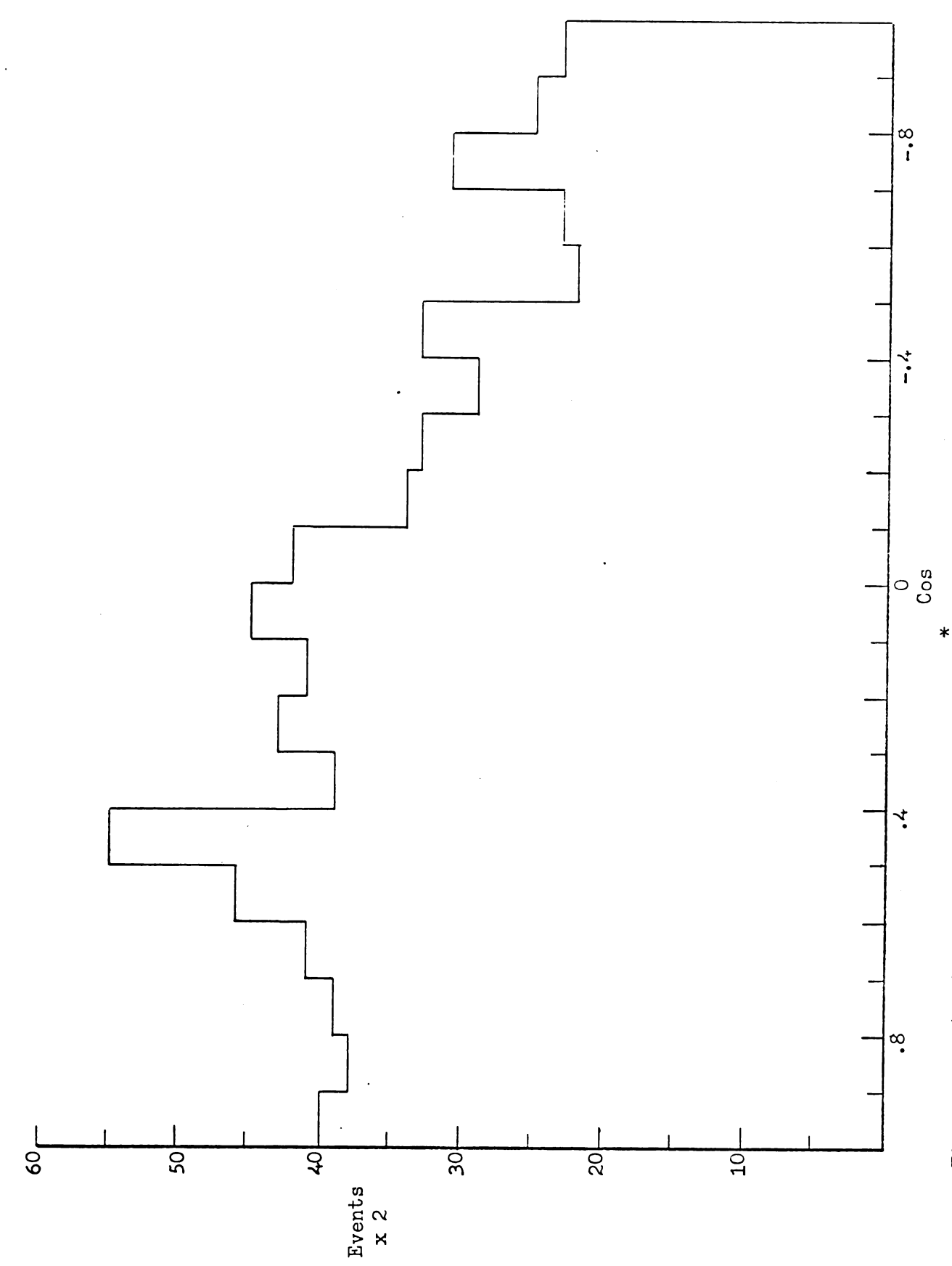


Figure 47. Angular distribution of pion in M system; 361 ppm events with 1.28 < Po < 1.43 ker/c.

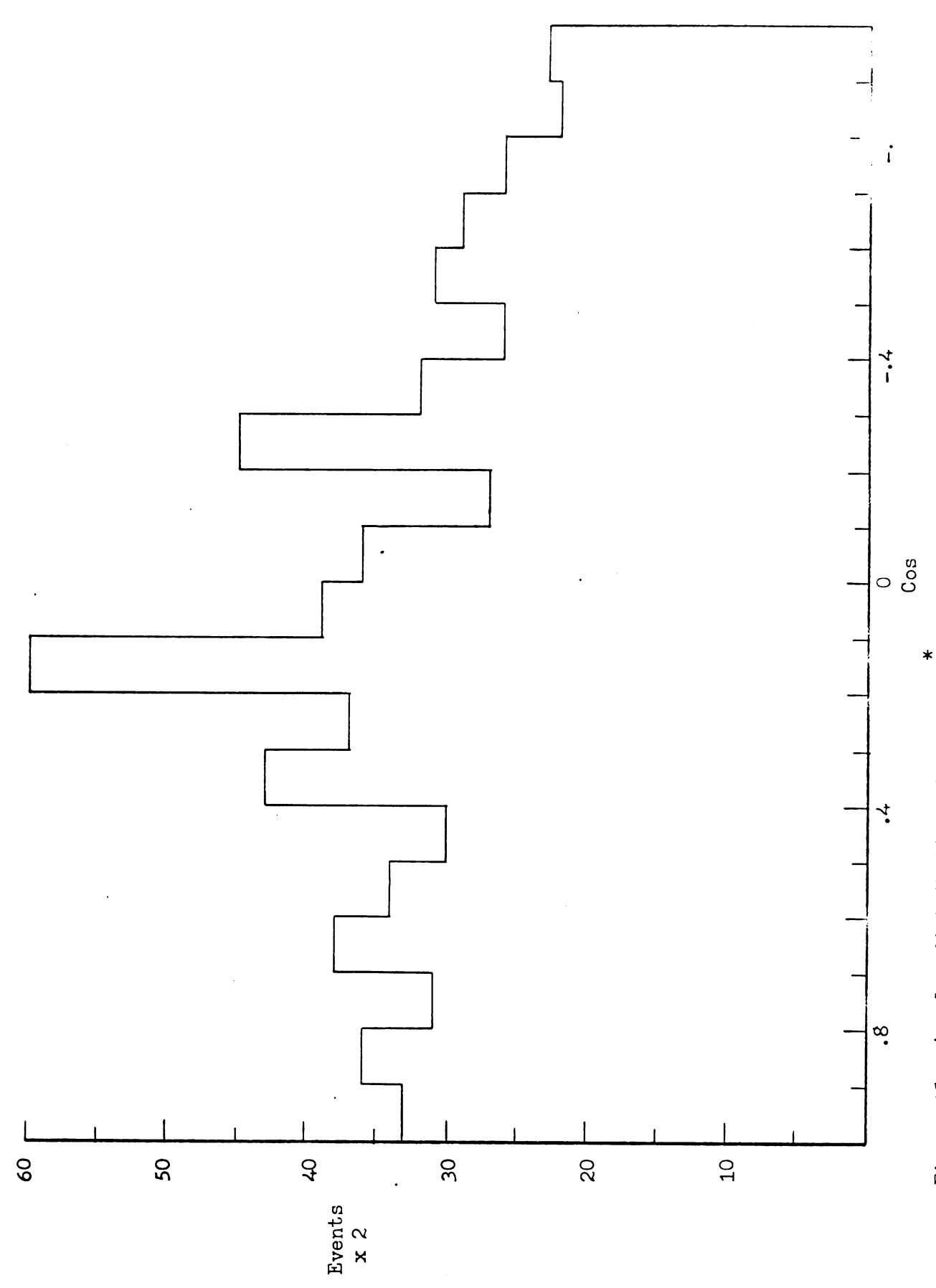


Figure 48. Angular distribution of pion in M system; 339 ppm events with 1.43 < P_0 < 1.53 bev/c.

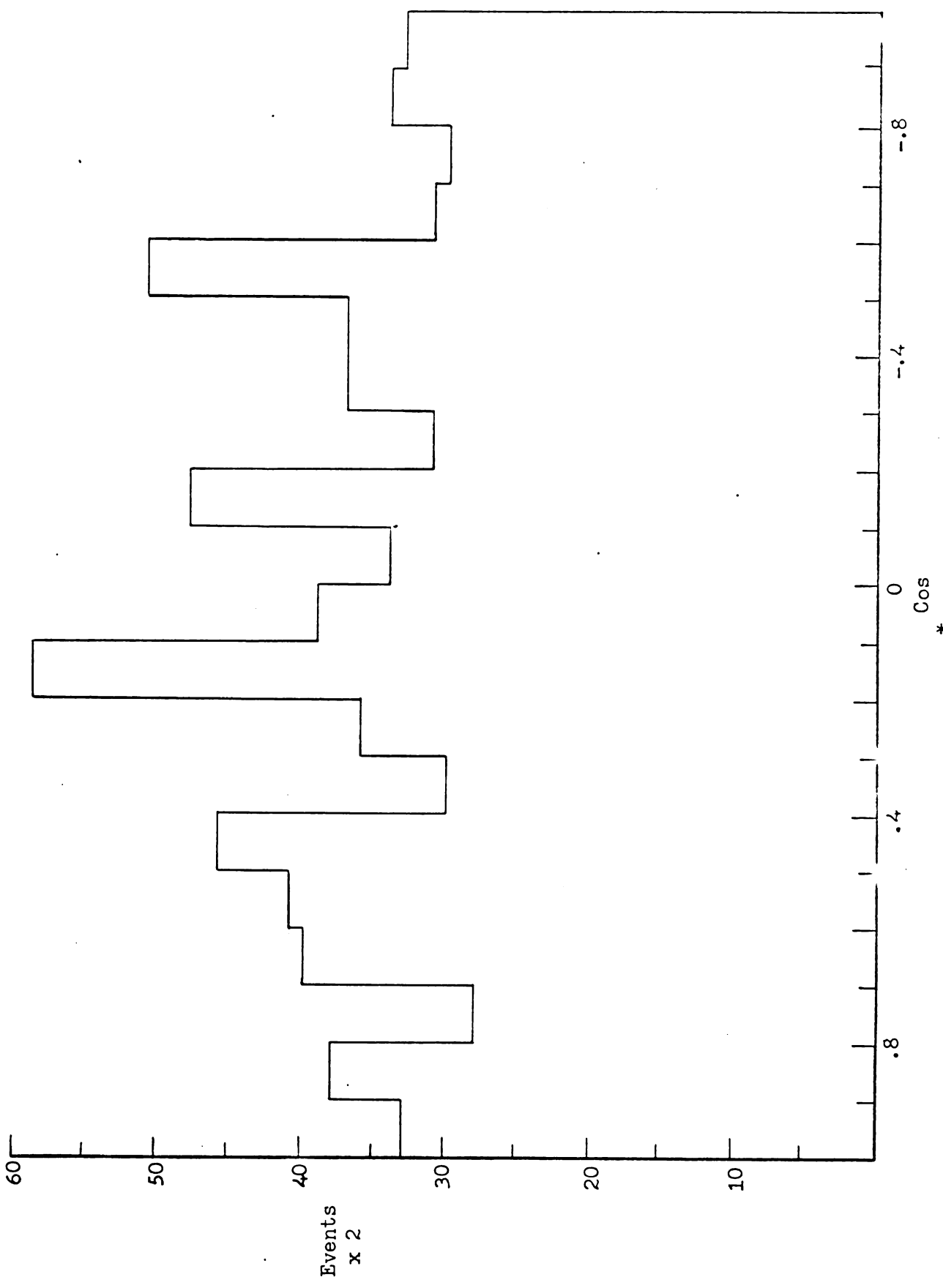


Figure 49. Angular distribution of pion in M system; 378 ppm events with 1.58 < P_0 < 1.75 bev/s.

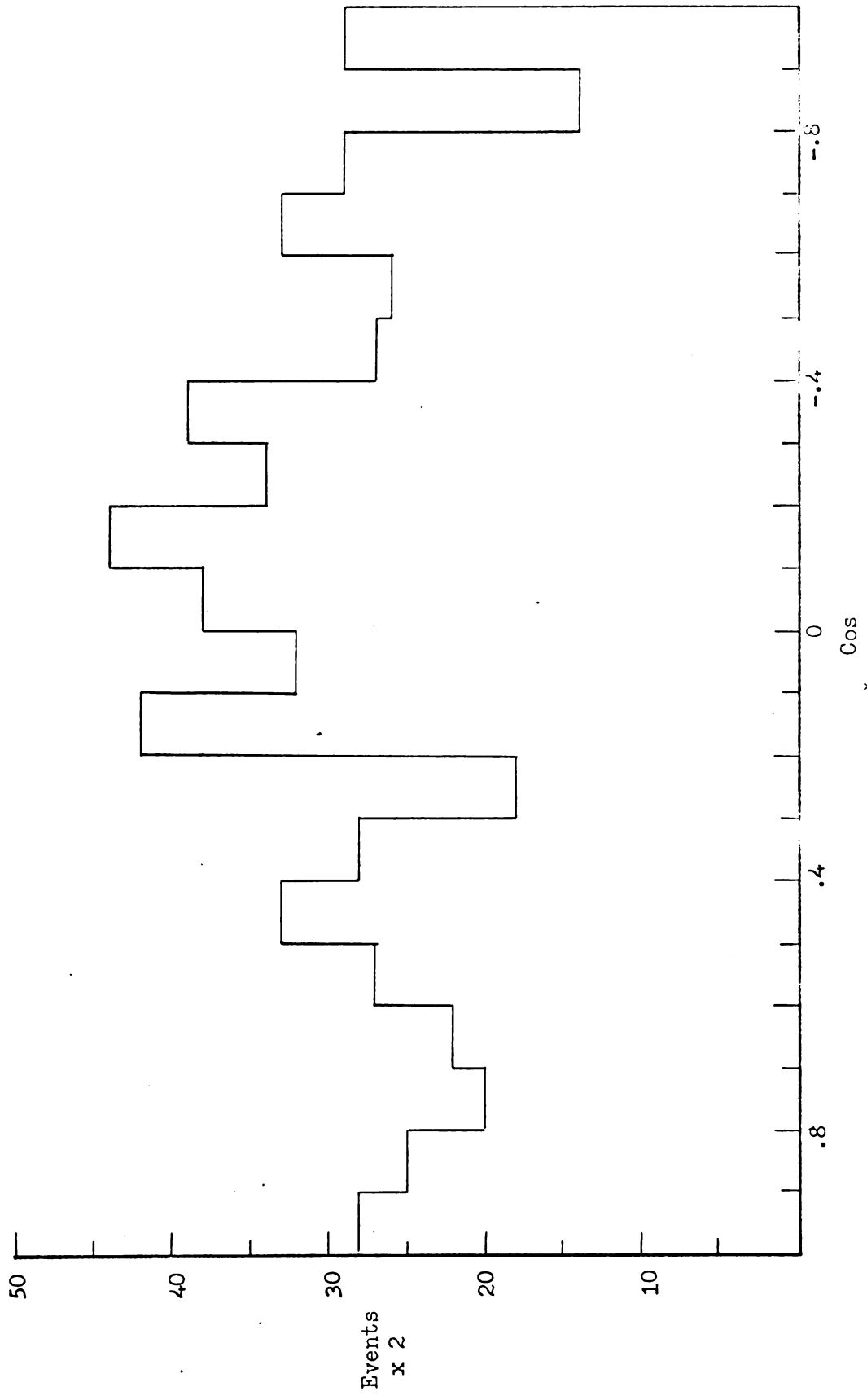
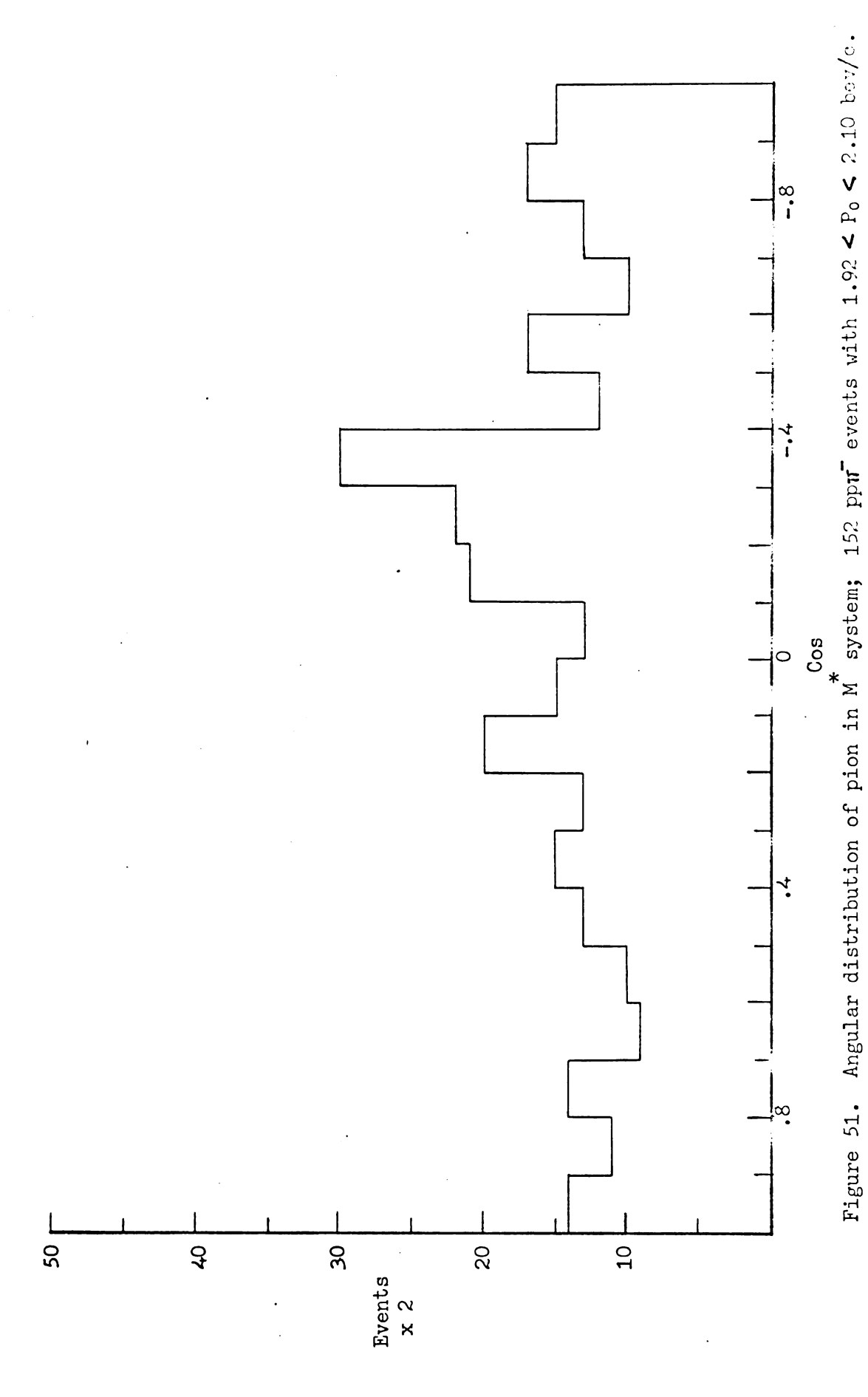


Figure 50. Angular distribution of pion in M system; 294 pp \vec{r} events with 1.75 < P_0 < 1.99 kery/s.

!
:



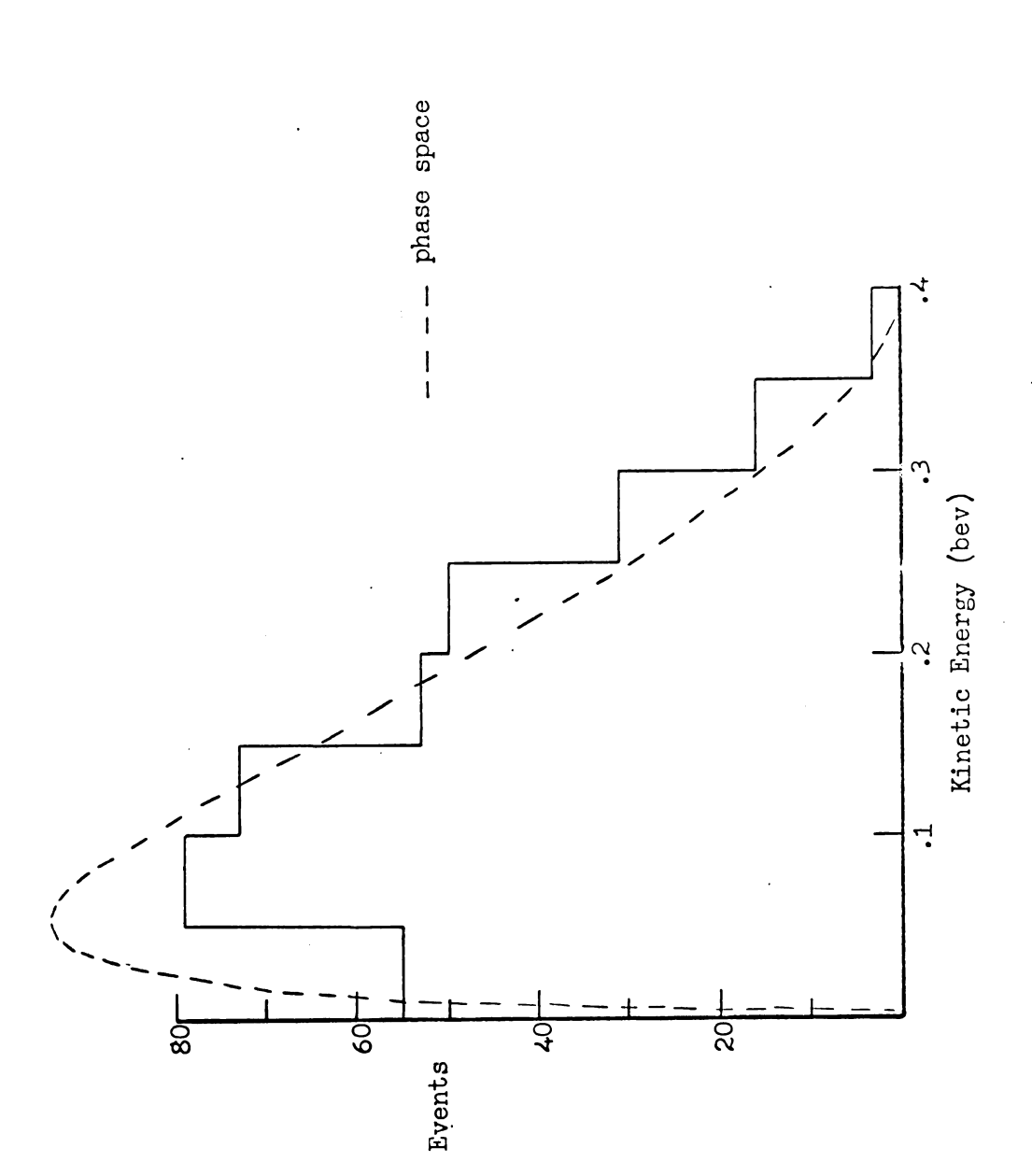


Figure 52. Pion lab kinetic energy; 361 ppm events with 1.28 < Po < 1.43 bev/c.

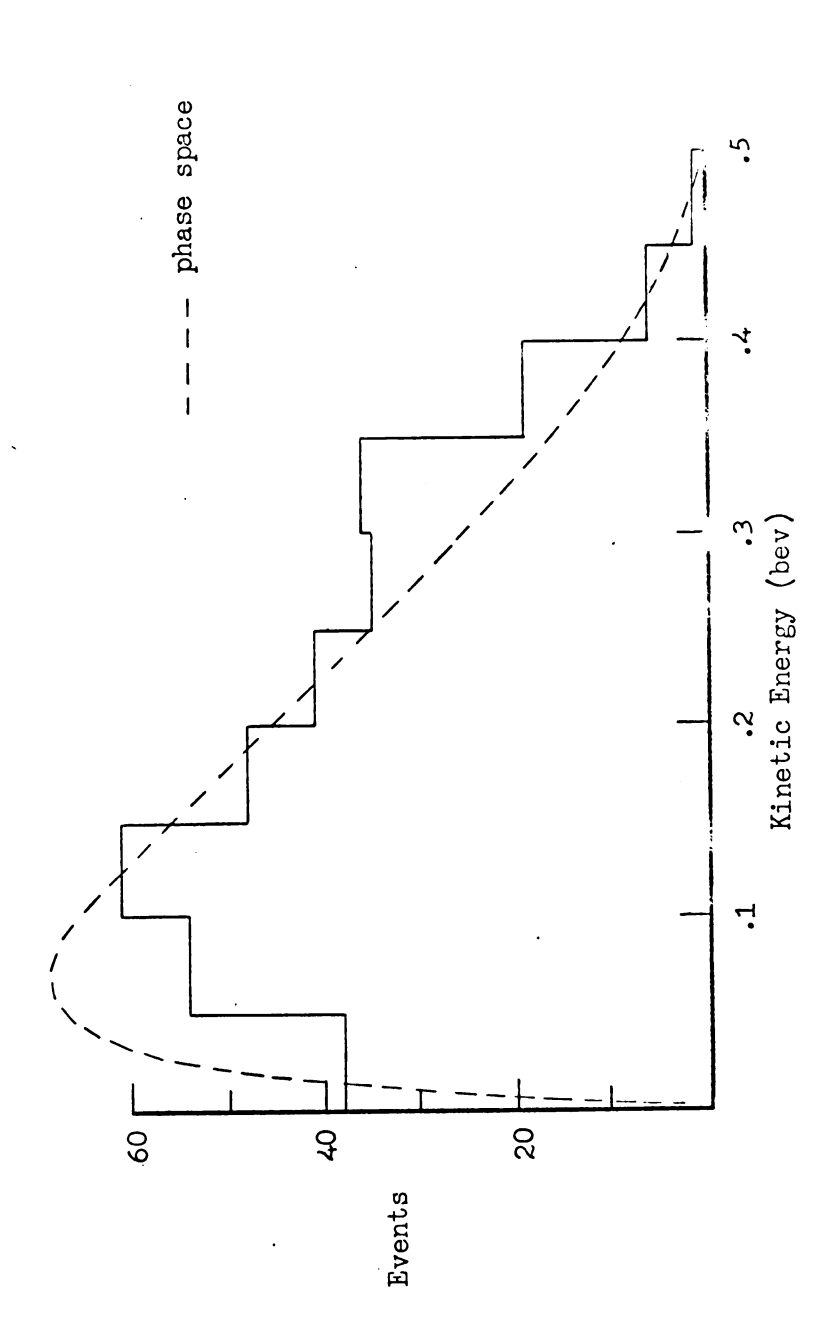


Figure 53. Pion lab kinetic energy; 339 pp \vec{r} events with 1.43 < Po < 1.58 bev/:

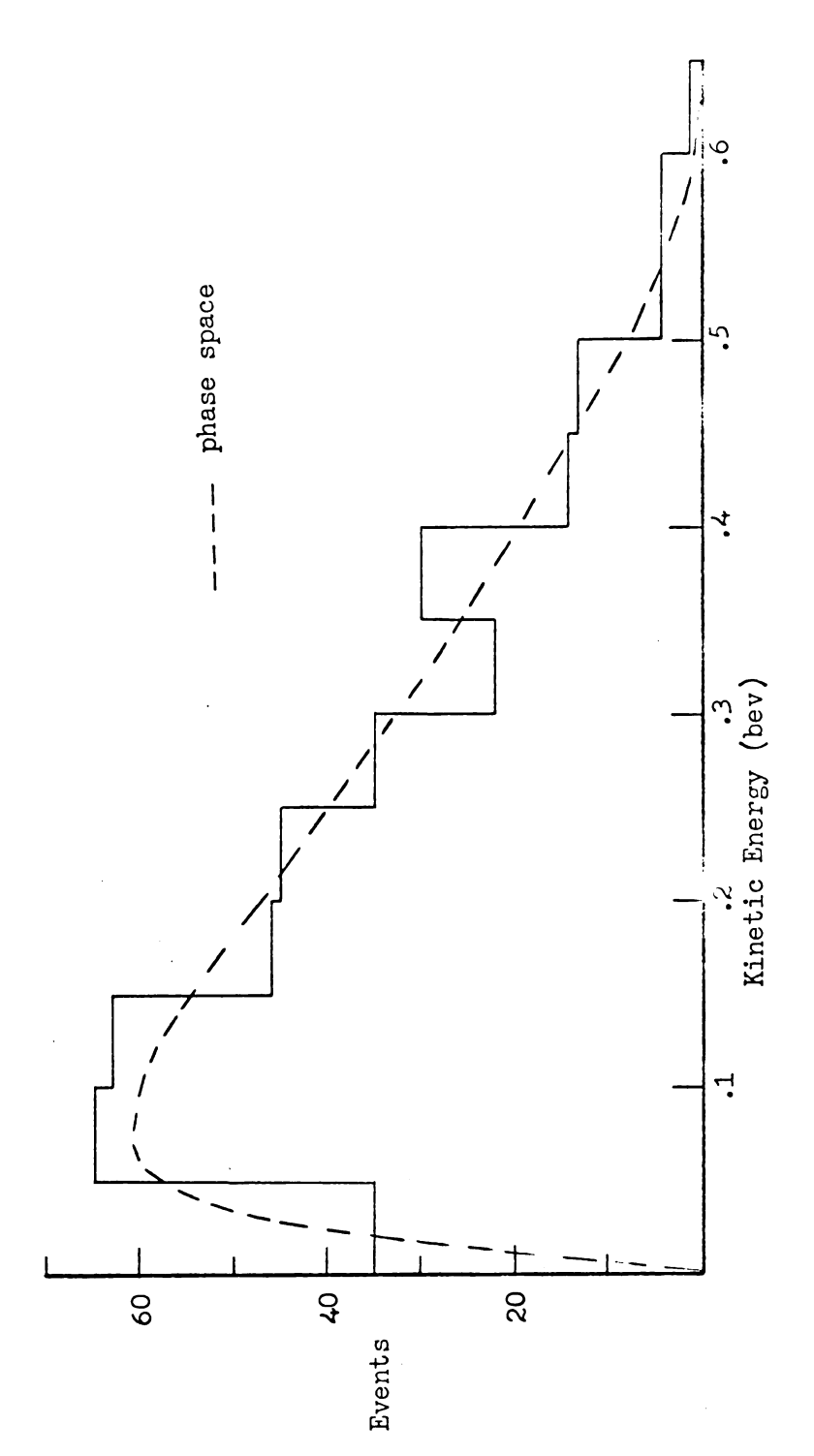


Figure 54. Pion lab kinetic energy; 378 pp \bar{n} events with 1.58 < P₀ < 1.75 bev/c.

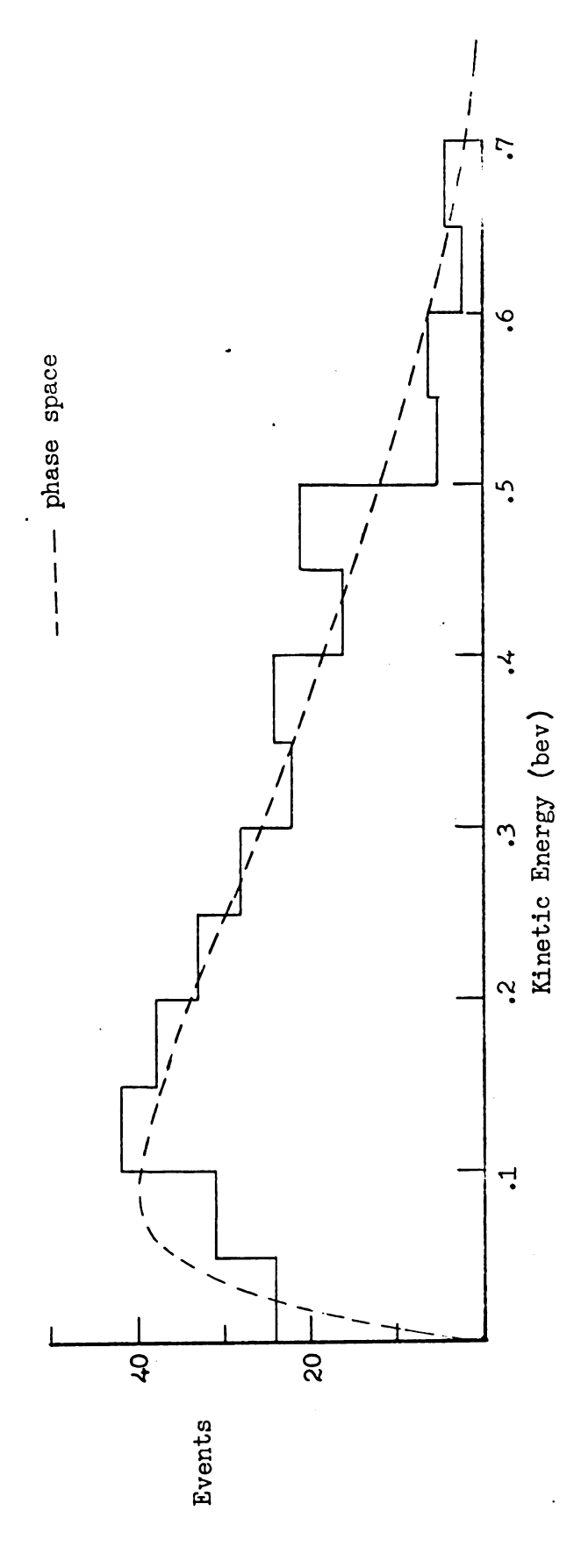
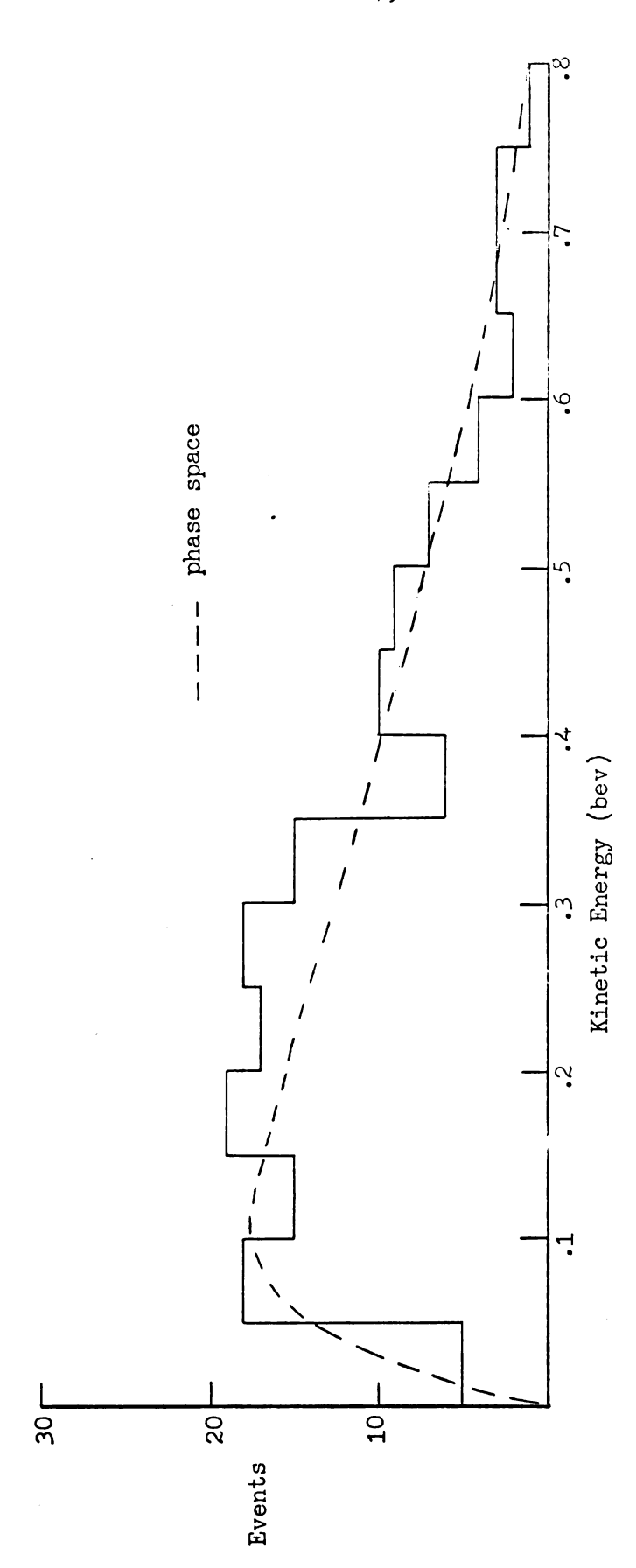


Figure 55. Pion lab kinetic energy; 294 pp \vec{n} events with 1.75 < P₀ < 1.92 bev/c.



vî

Figure 56. Pion lab kinetic energy; 152 pp \vec{r} events with 1.92 < Po < 2.10 bev/c.

			;
			•
,			
			•

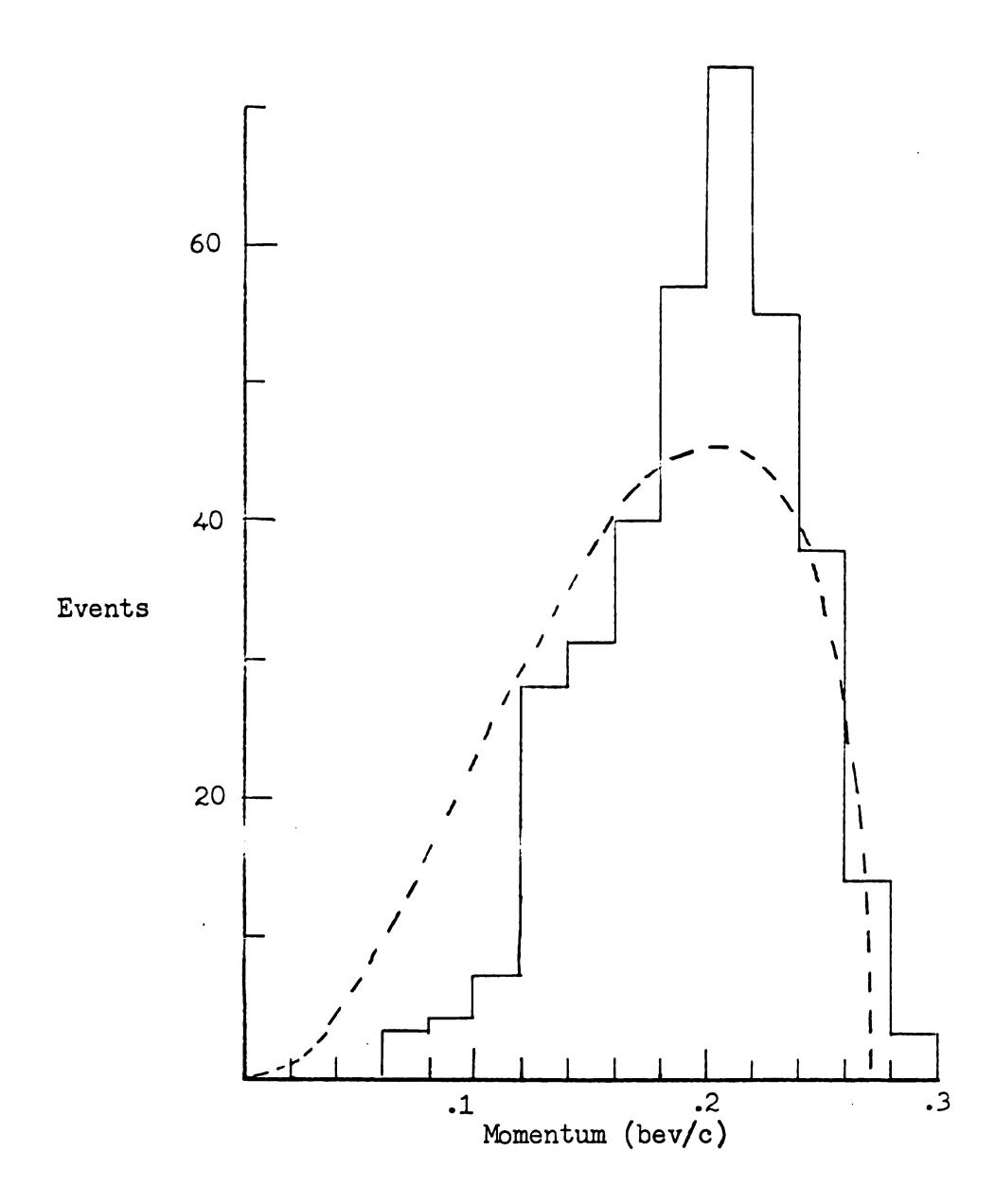


Figure 57. Pion center of mass momentum; $361 \text{ pp} \overline{\pi} \text{ events with } 1.28 < P_0 < 1.43 \text{ pev/c}.$ ---- phase space

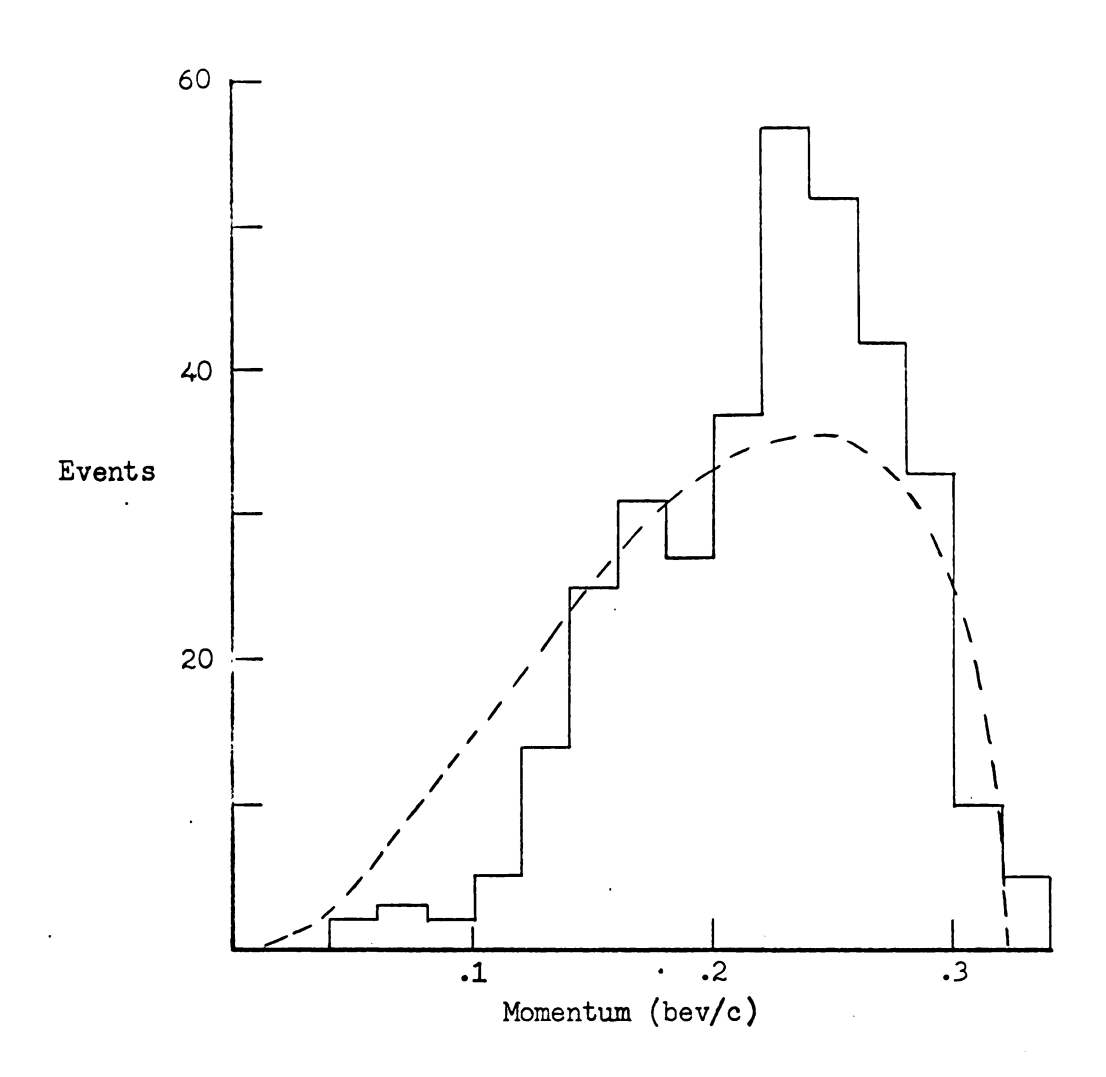


Figure 58. Pion center of mass momentum; 339 pp π^- events with 1.43 < P₀ < 1.58 bev/c. --- phase space

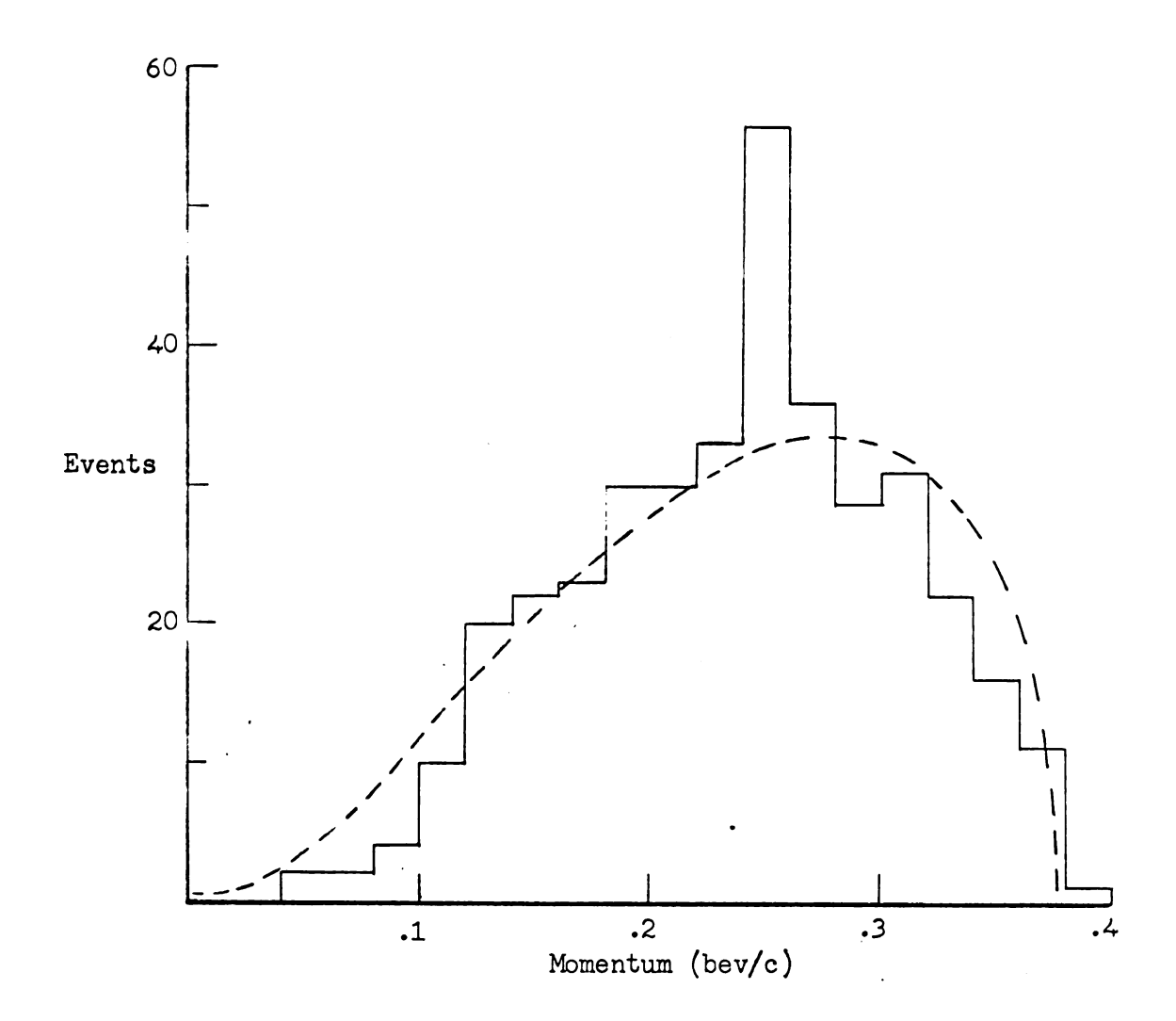


Figure 59. Pion center of mass momentum; $378 \text{ pp} \pi^-$ events with 1.58 < P₀ < 1.75 bev/c. --- phase space

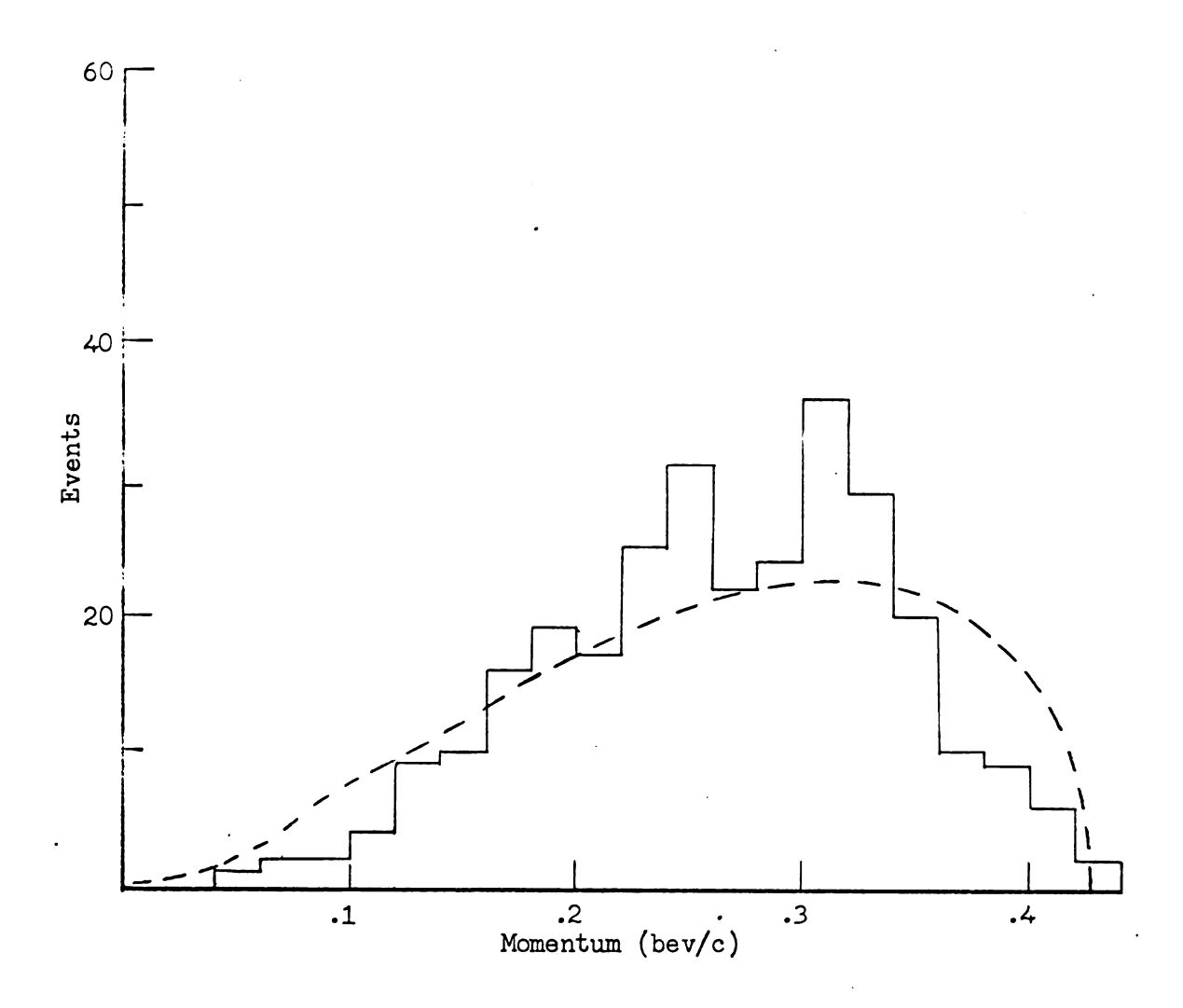


Figure 60. Pion center of mass momentum; 294 pp π^- events with 1.75 < P₀ < 1.92 bev/c. --- phase space

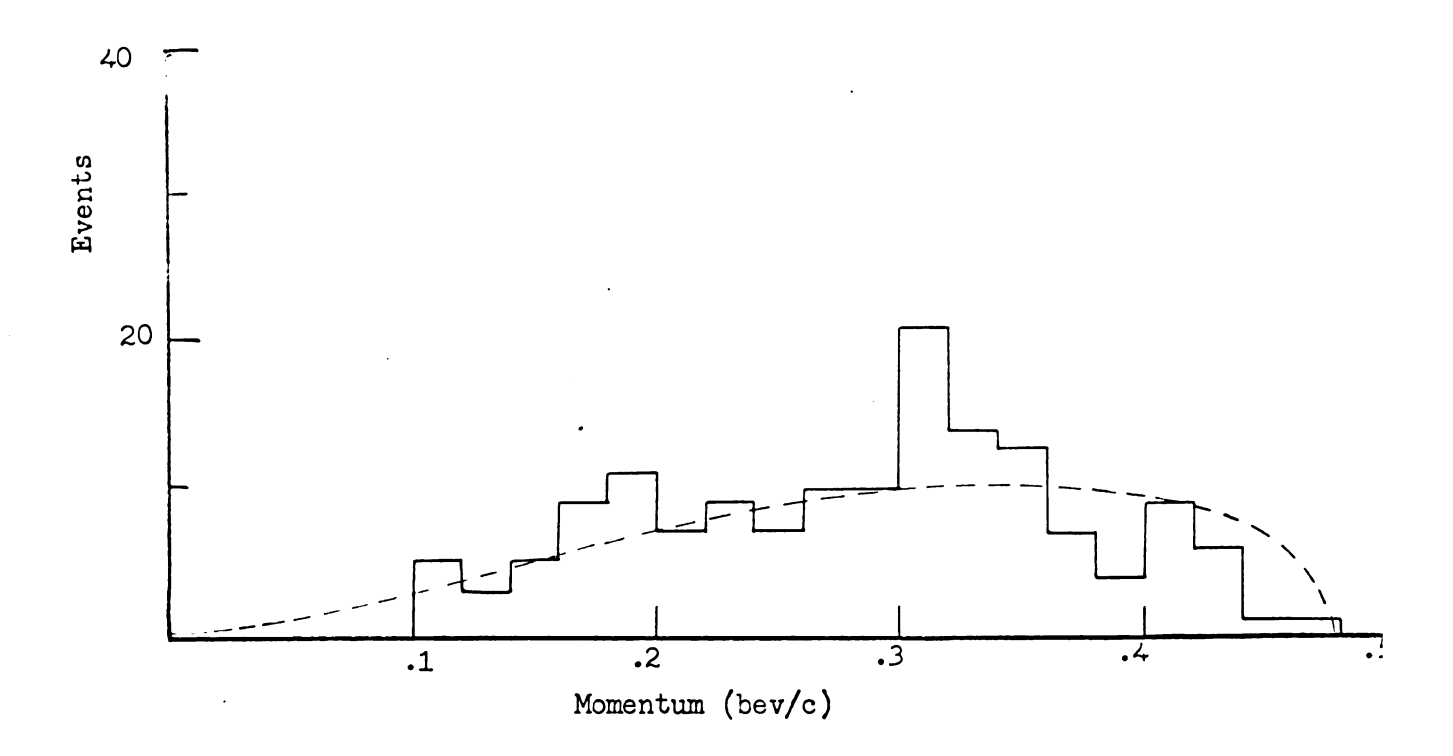


Figure 61. Pion center of mass momentum; 152 pp π events with 1.92 < P₀ < 2.10 bev/c. _ _ _ phase space

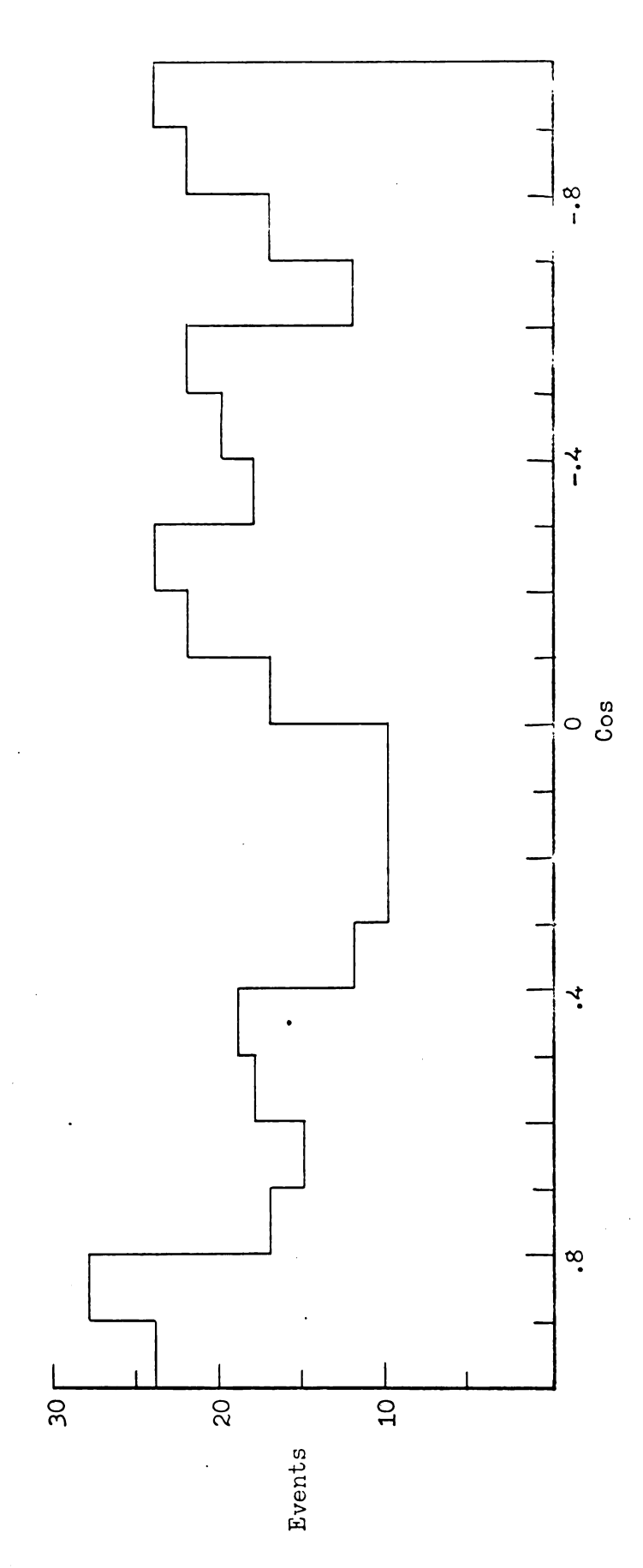


Figure 62. Pion center of mass angular distribution; 361 ppm events with 1.28 < Po < 1.43 FeV/c.

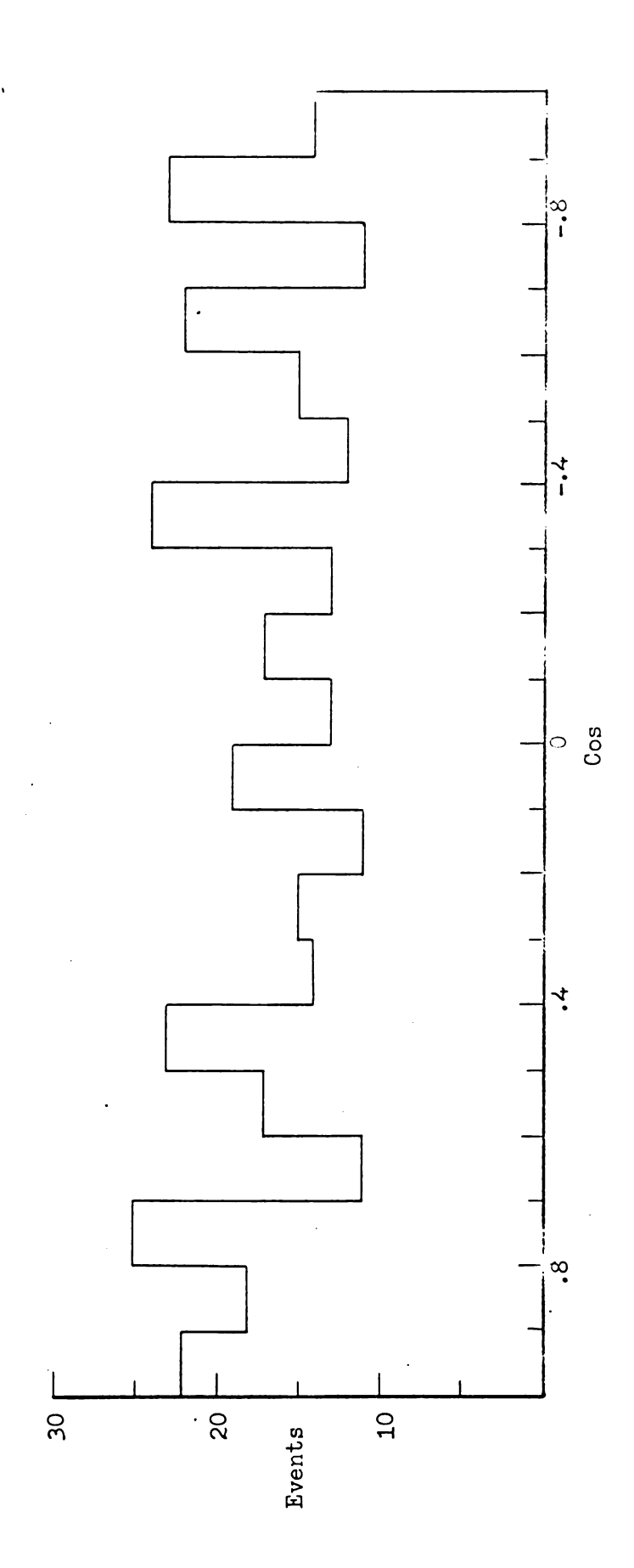


Figure 63. Pion center of mass angular distribution; 339 pp \vec{r} events with 1.43 < Γ_0 < 1.53 bev/c.

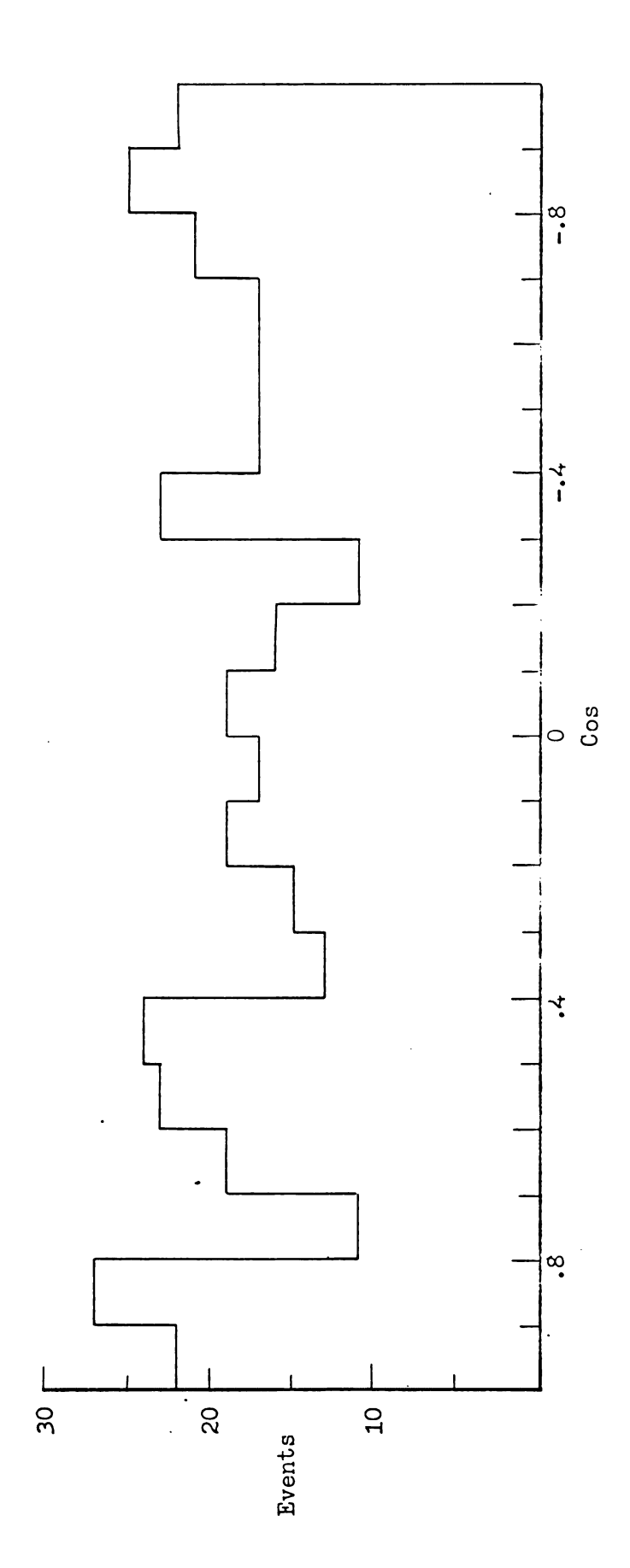


Figure 64. Pion center of mass angular distribution; 378 pp \vec{m} events with 1.58 < P₀ < 1.75 be::/c.

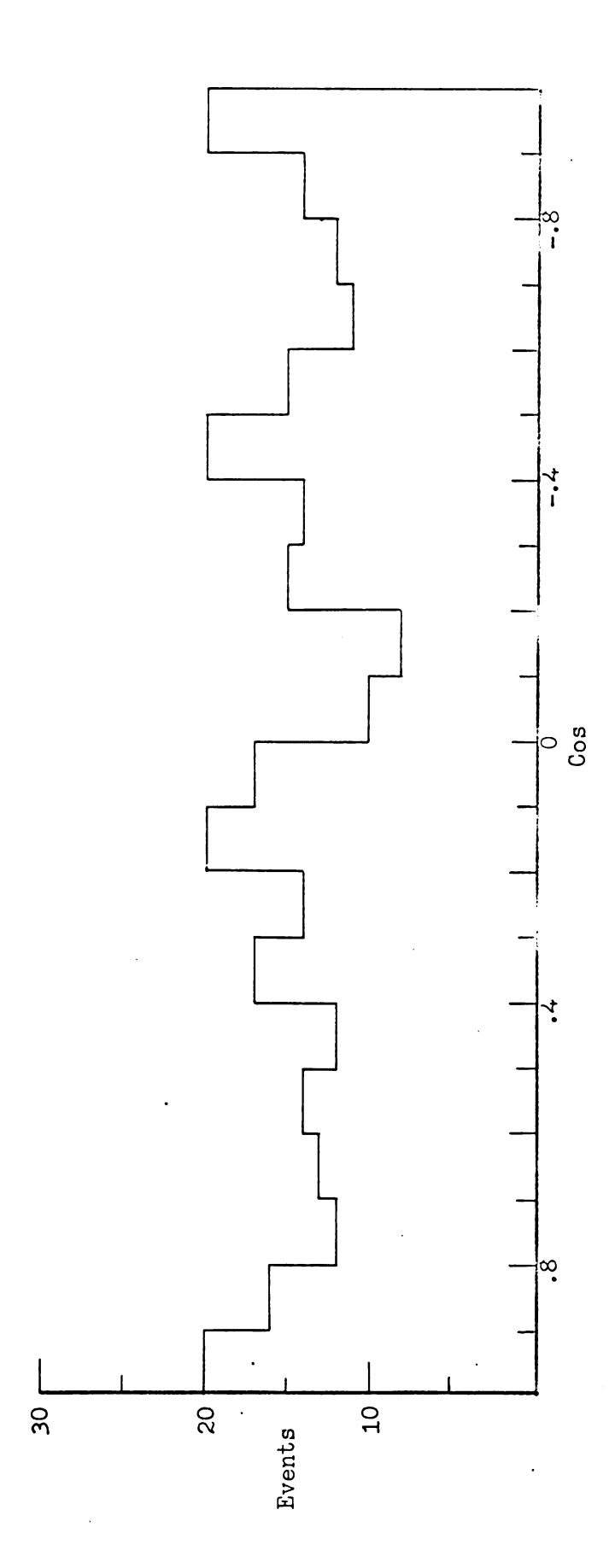


Figure 65. Pion center of mass angular distribution; 294 pp \vec{n} events with 1.75 < Po < 1.92 bey/c.

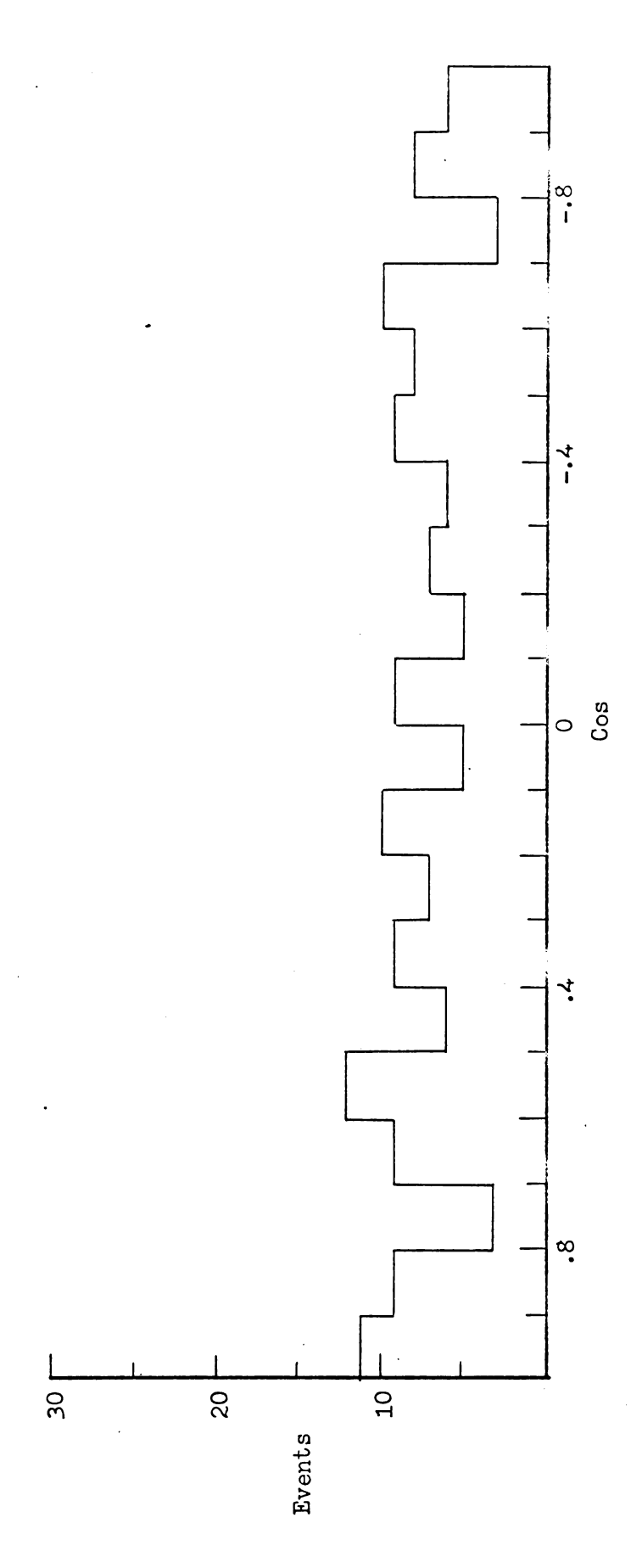


Figure 66. Pion center of mass angular distribution; 152 pp η events with 1.92 < Po < 2.10 be η /c.

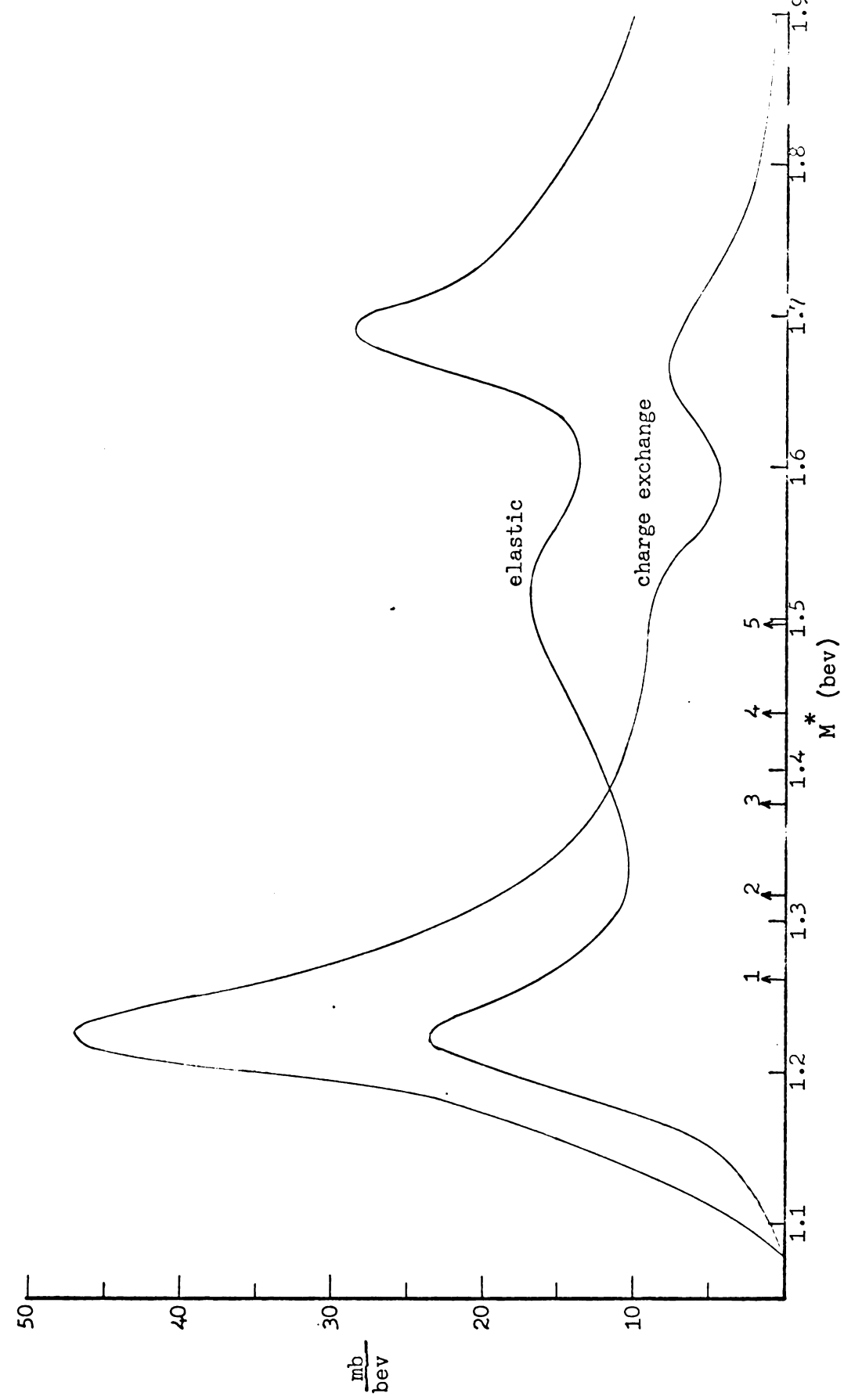
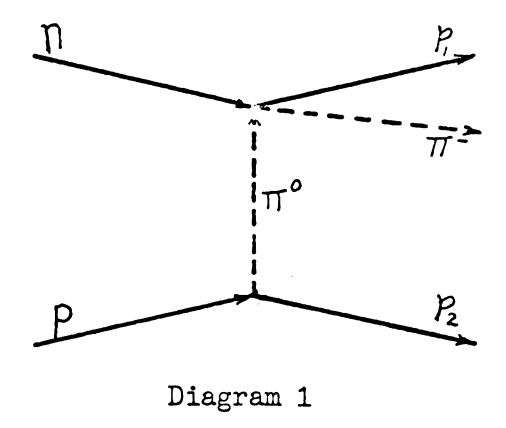


Figure 67. Elastic and charge exchange scattering cross-section for π^- p scattering as a function of the invariant mass of the pair. The arrows are the upper limits of M for the mean values of incident momentum of the five slices of the $\mathrm{pp}\pi^-$ data.



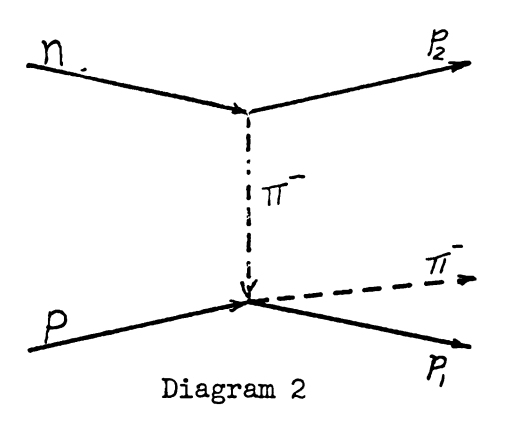


Figure 68. Peripheral diagrams for the pp π^- events. Diagram 1 indicates the proton in the bubble chamber emits a π^0 which is scattered with charge exchange by the incident neutron. Diagram 2 indicates the incident neutron emits a π^- and continues as a proton and the π^- scatters from the proton in the chamber.

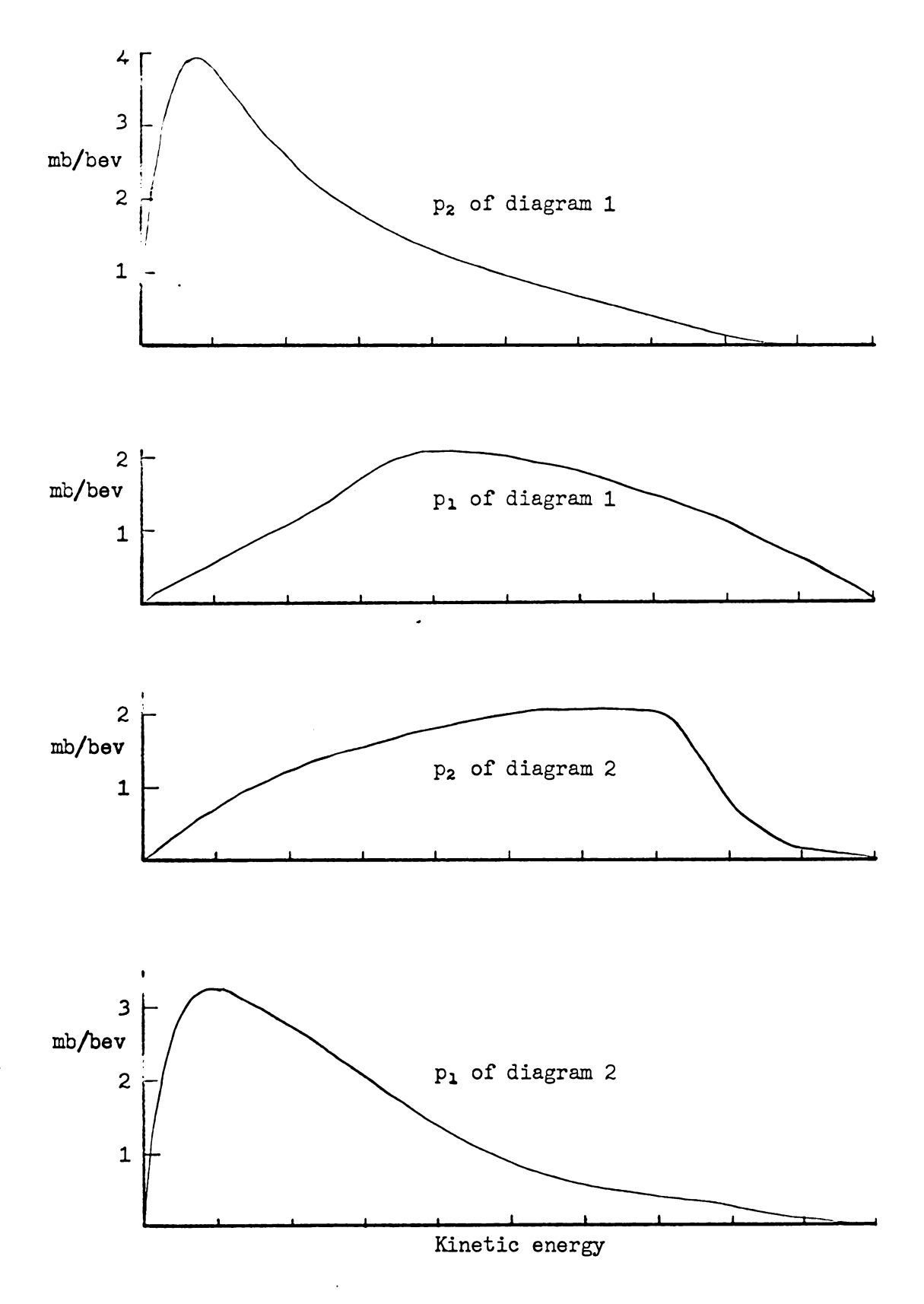
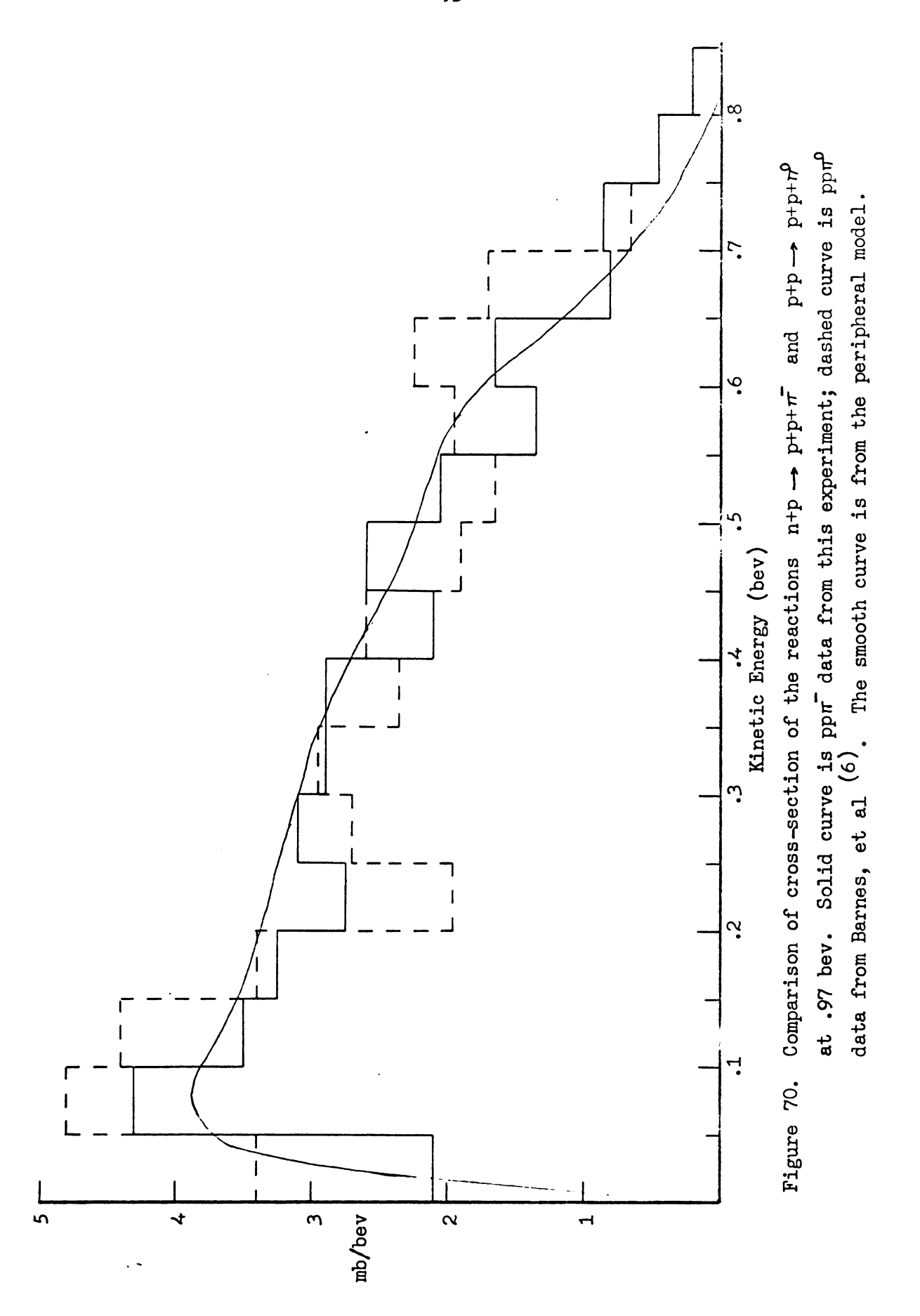


Figure 69. Contributions to the kinetic energy spectrum of the protons from each diagram of the $pp\pi$ data. These curves are taken from the .97 bev data.



i
ì

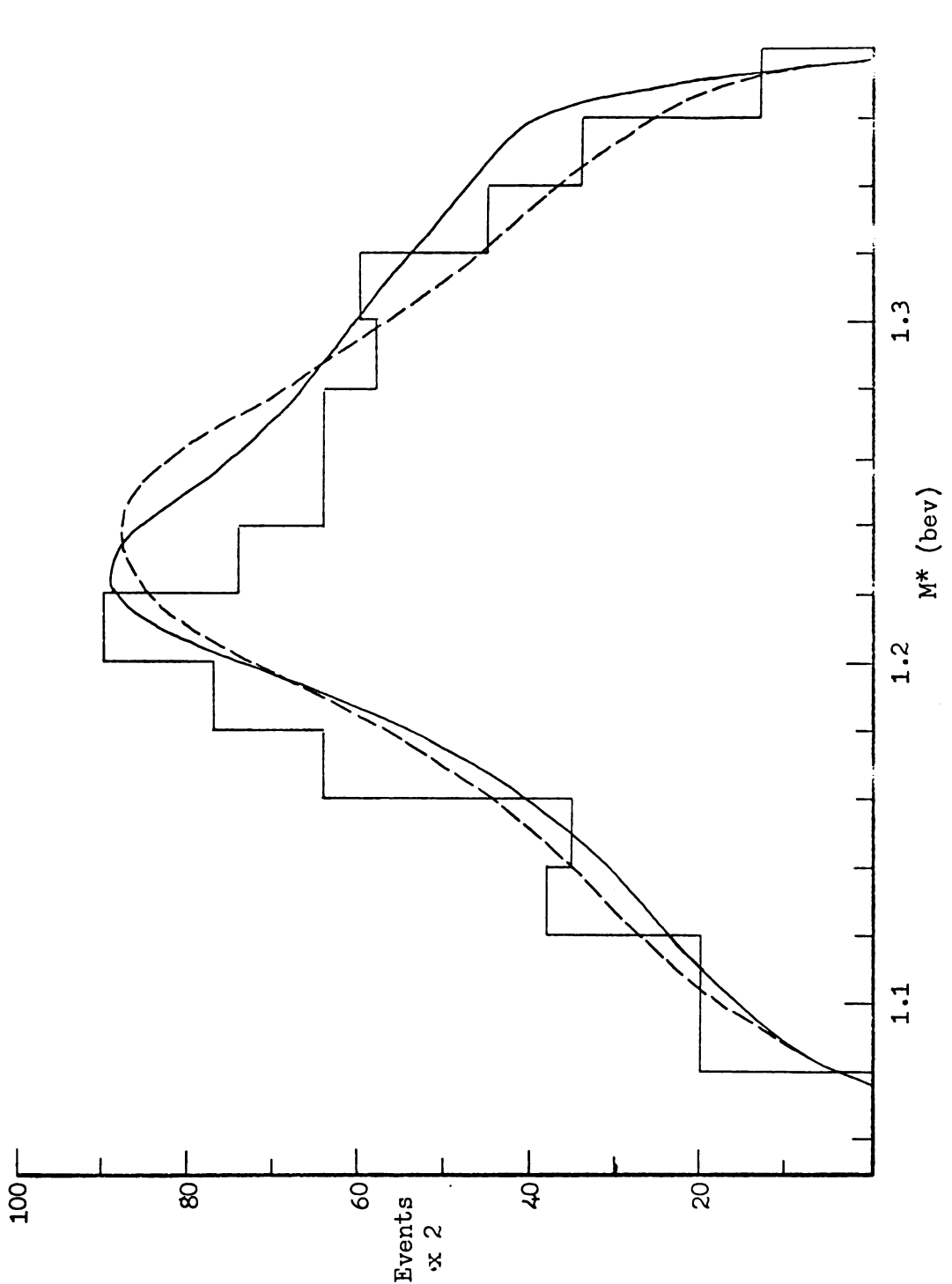


Figure 71. Comparison of M* spectrum from peripheral model and from phase space with resonance. The solid curve is from the peripheral model, the dashed curve is from phase space with a 3,3 resonance between the pion and proton folded in. See figure 44.

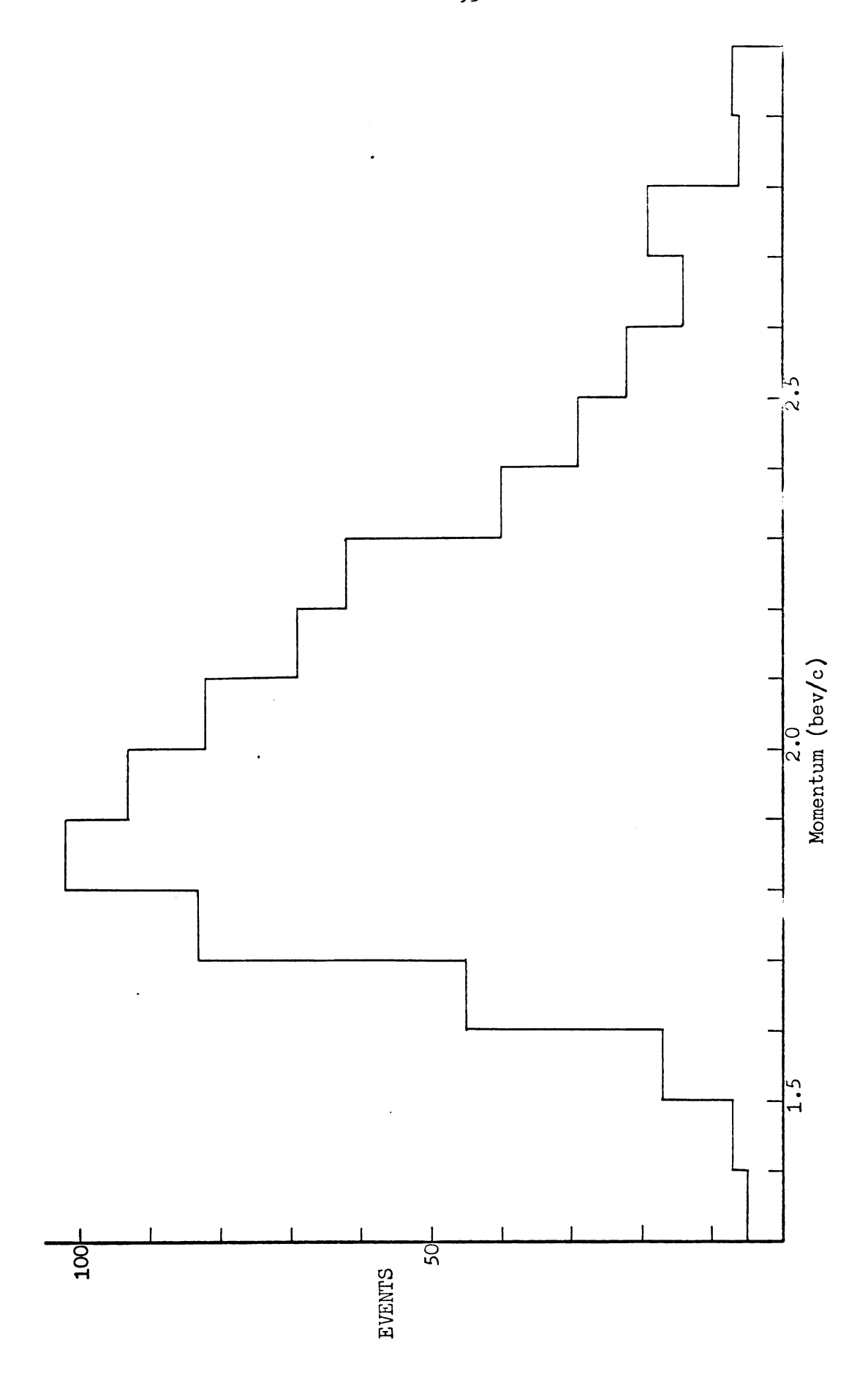
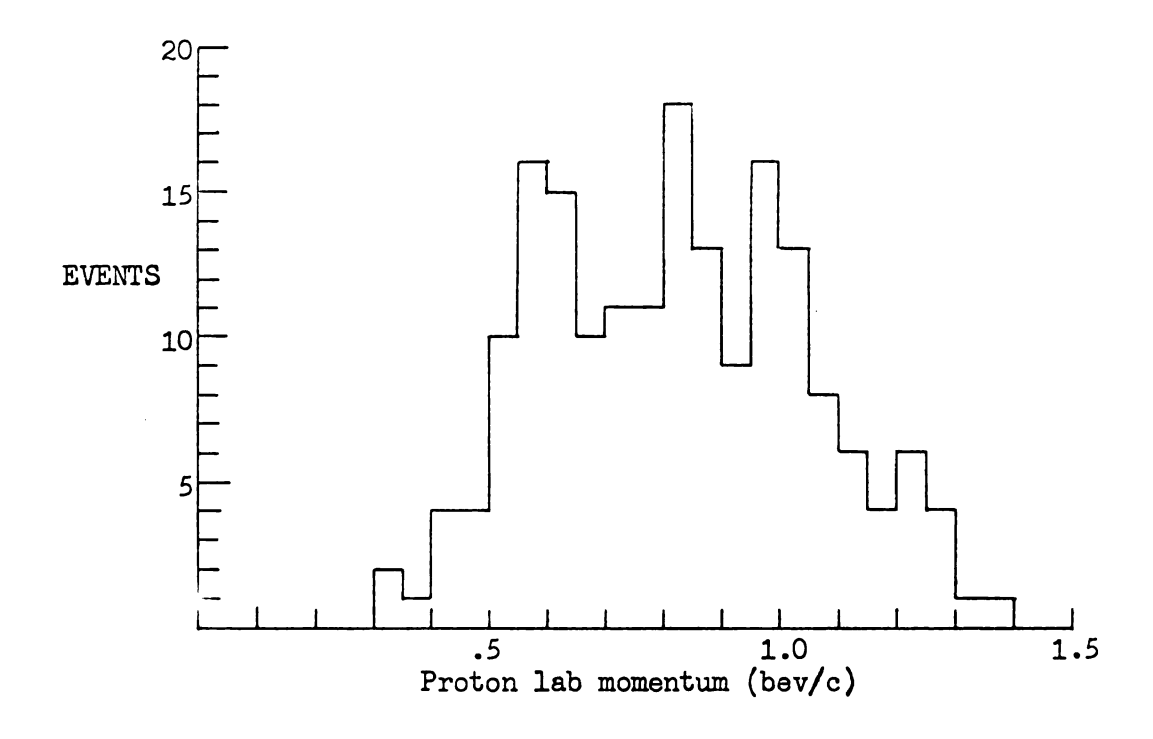


Figure 72. Incident lab momentum of pn $\pi^+\pi^-$ events.



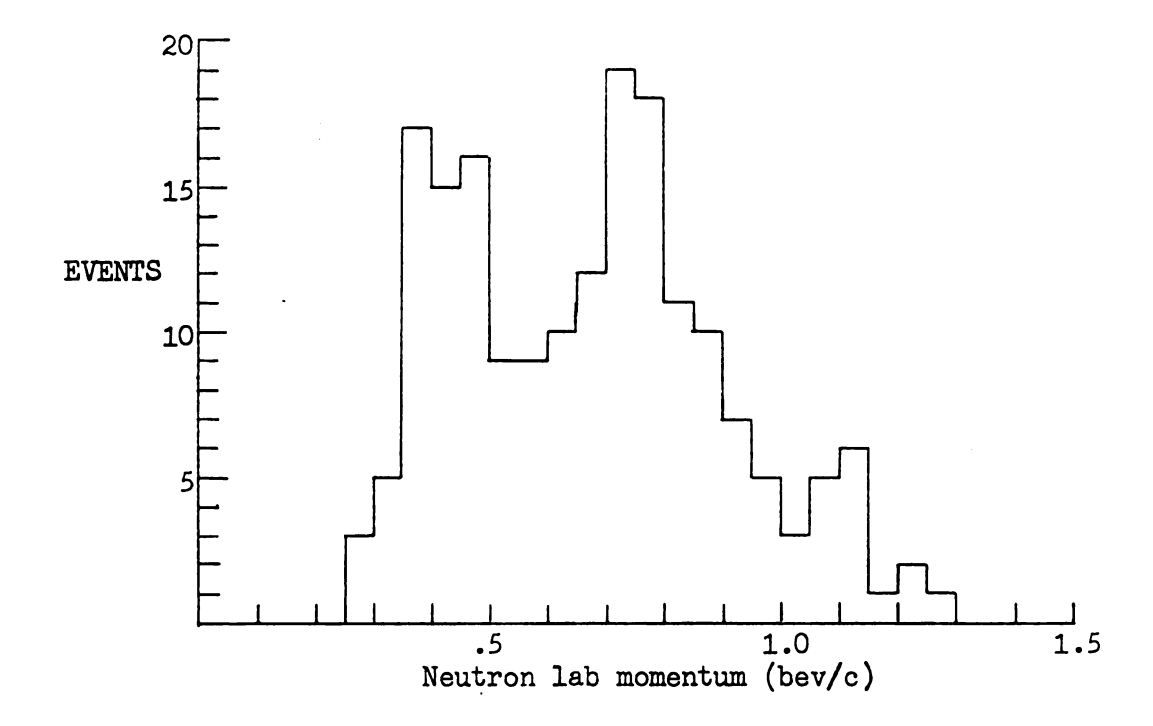
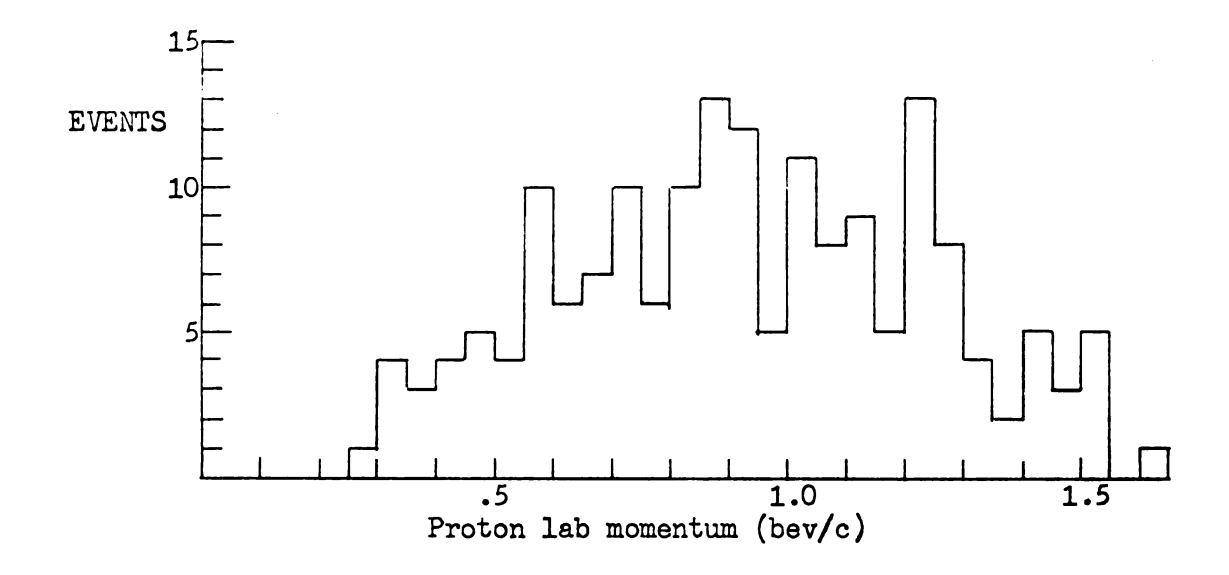


Figure 73. Nucleon lab momentum: 184 pn $\pi^+\pi^-$ events with 1.7 < Po < 1.9 bev/c.



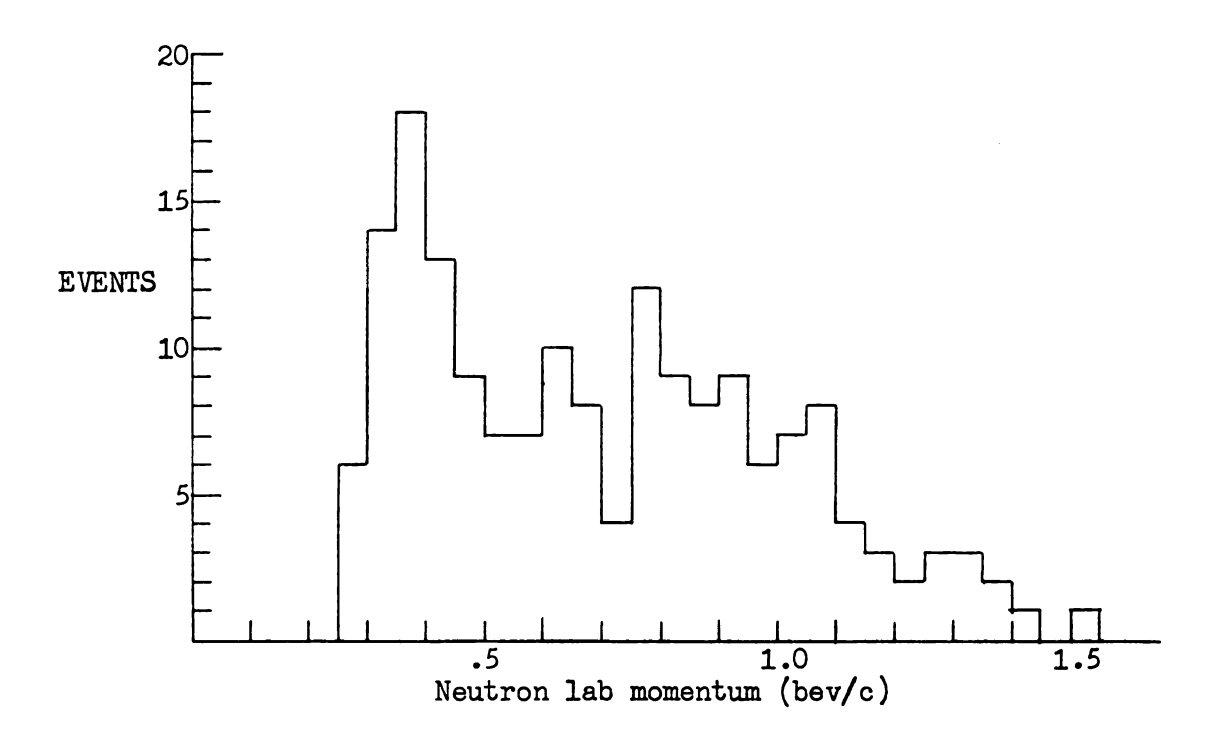
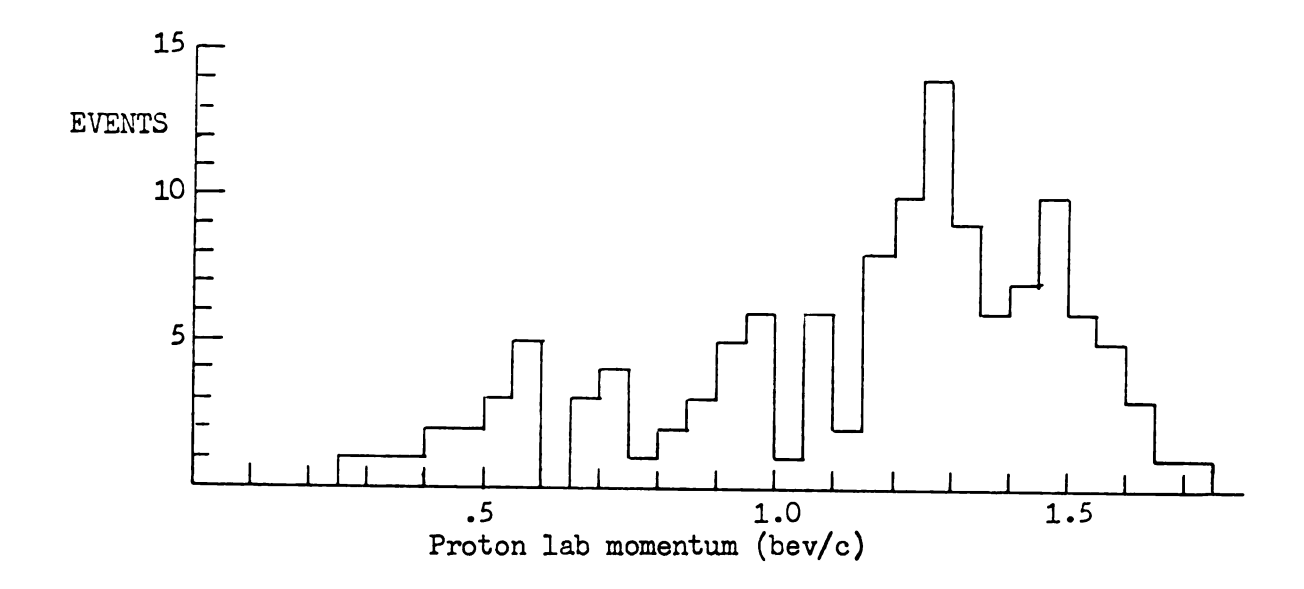


Figure 74. Nucleon lab momentum: 174 pn $\pi^{+}\pi^{-}$ events with 1.9 < Po < 2.1 bev/c.



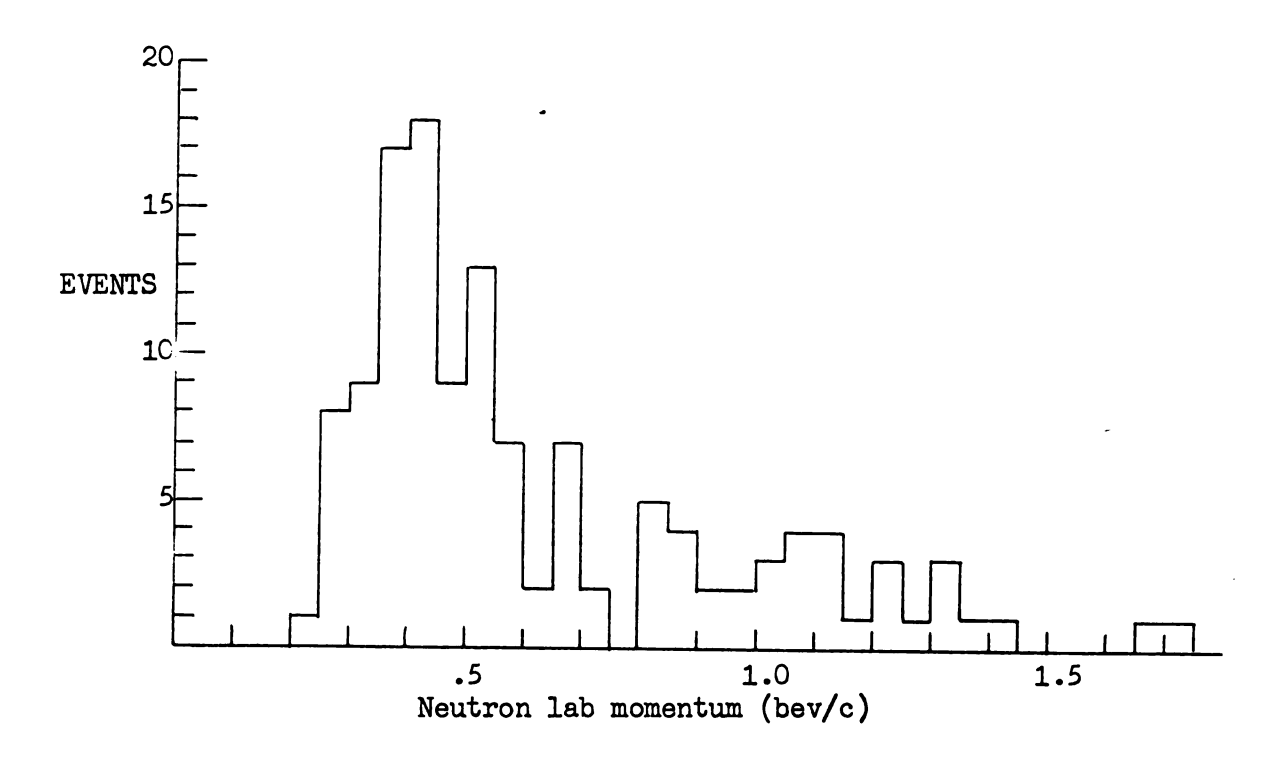


Figure 75. Nucleon lab momentum: 128 pn $\pi^+\pi^-$ events with 2.1 < Po < 2.3 bev/c.

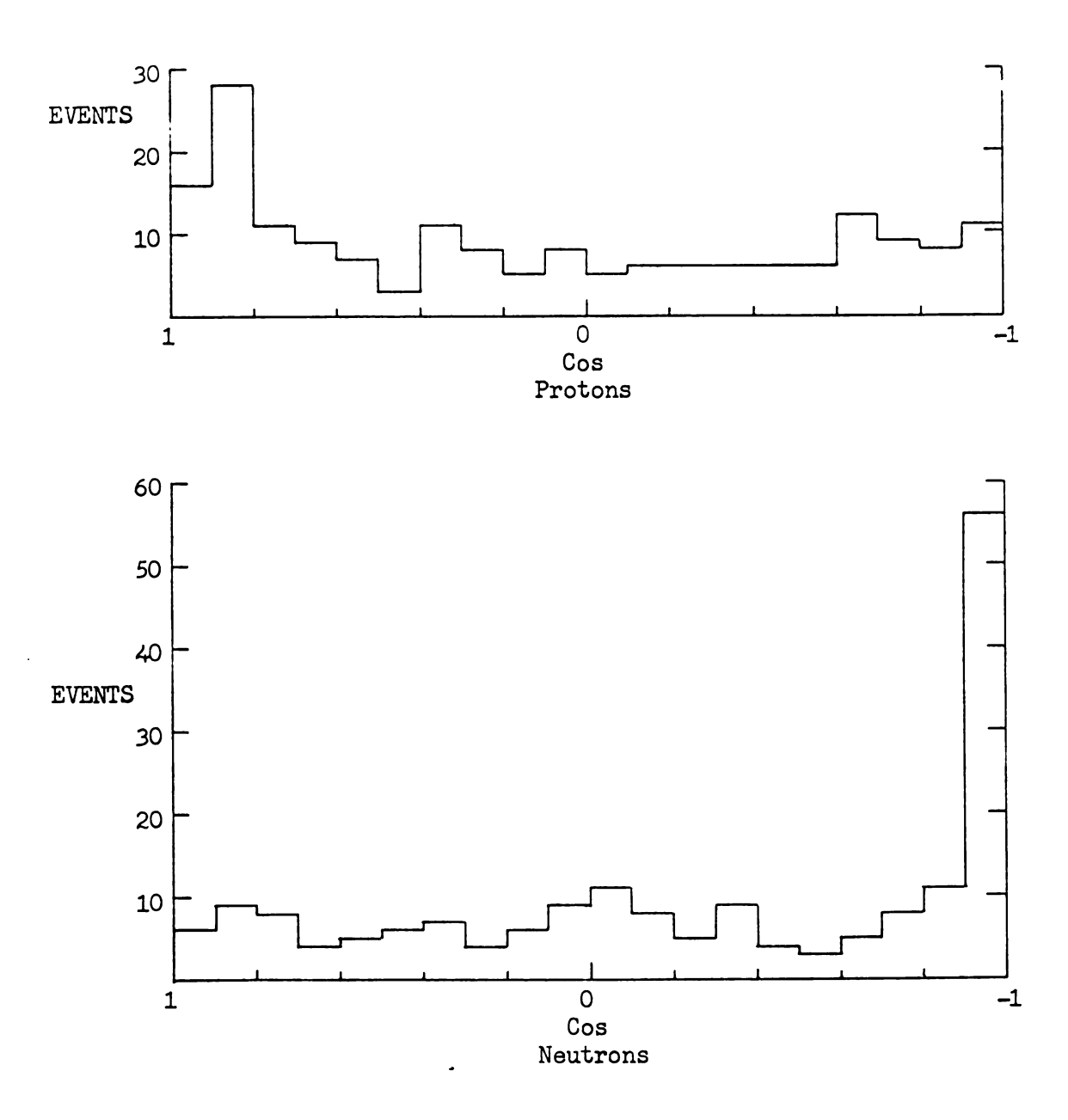


Figure 76. Nucleon center of mass angular distribution: $184~{\rm pn}\pi^+\pi^-~{\rm events}~{\rm with}~1.7 < P_0 < 1.9~{\rm bev/c}.$

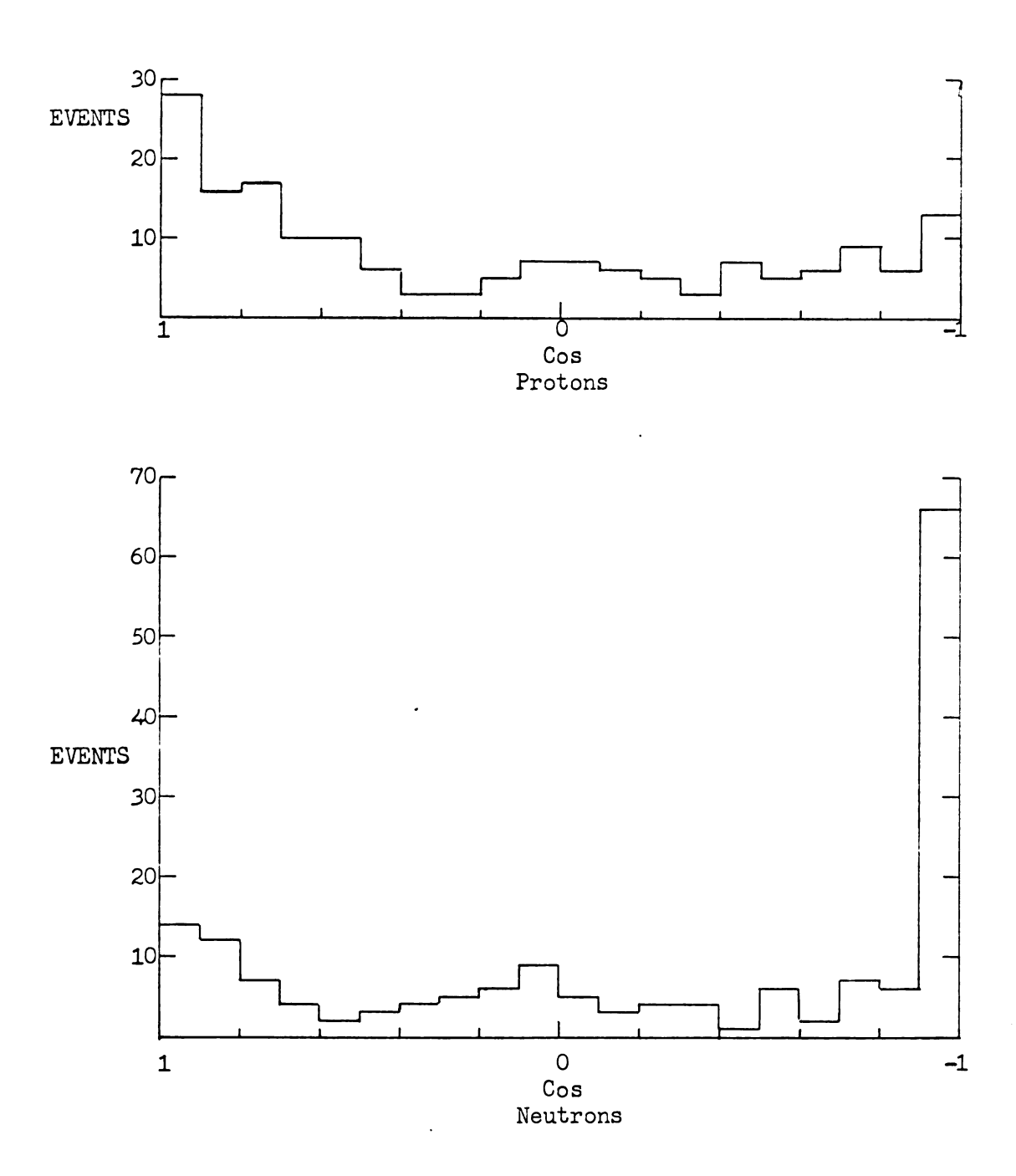
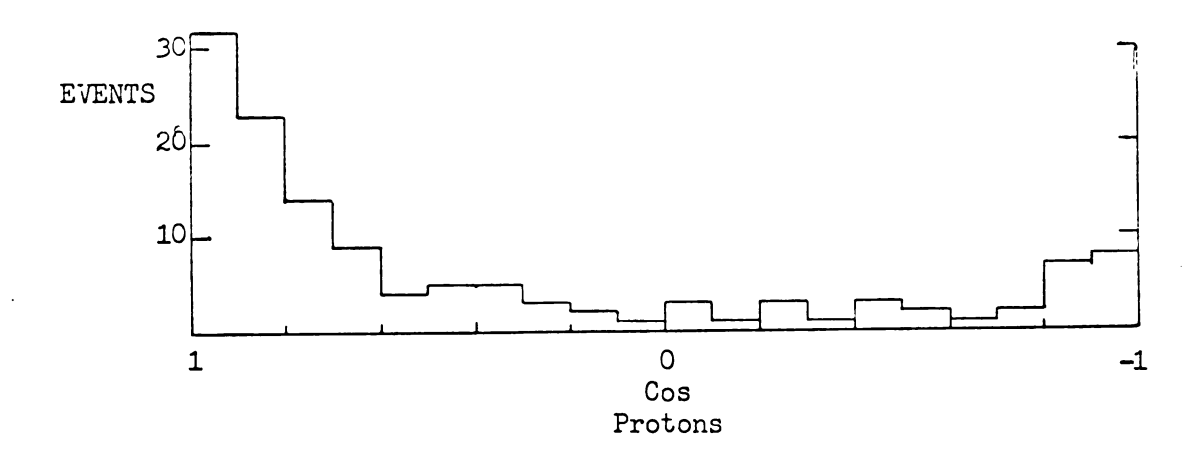


Figure 77. Nucleon center of mass angular distribution: $174~\rm pn\,\pi^+\pi^-~events~with~1.9 < P_0 < 2.1~bev/c.$



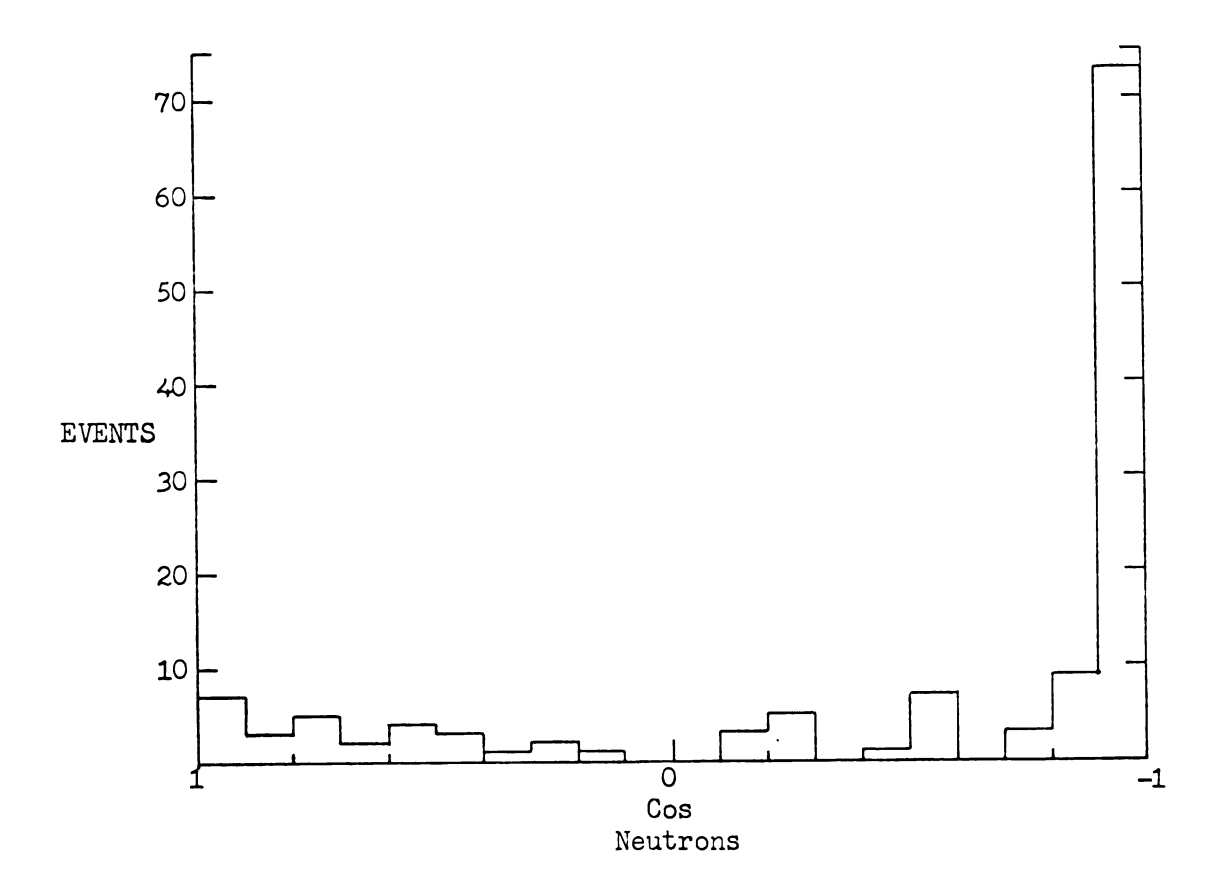


Figure 78. Nucleon center of mass angular distribution: $128~{\rm pn}\pi^+\pi^-~{\rm events~with~2.1} <~P_0 <~2.3~{\rm bev/c}\,.$

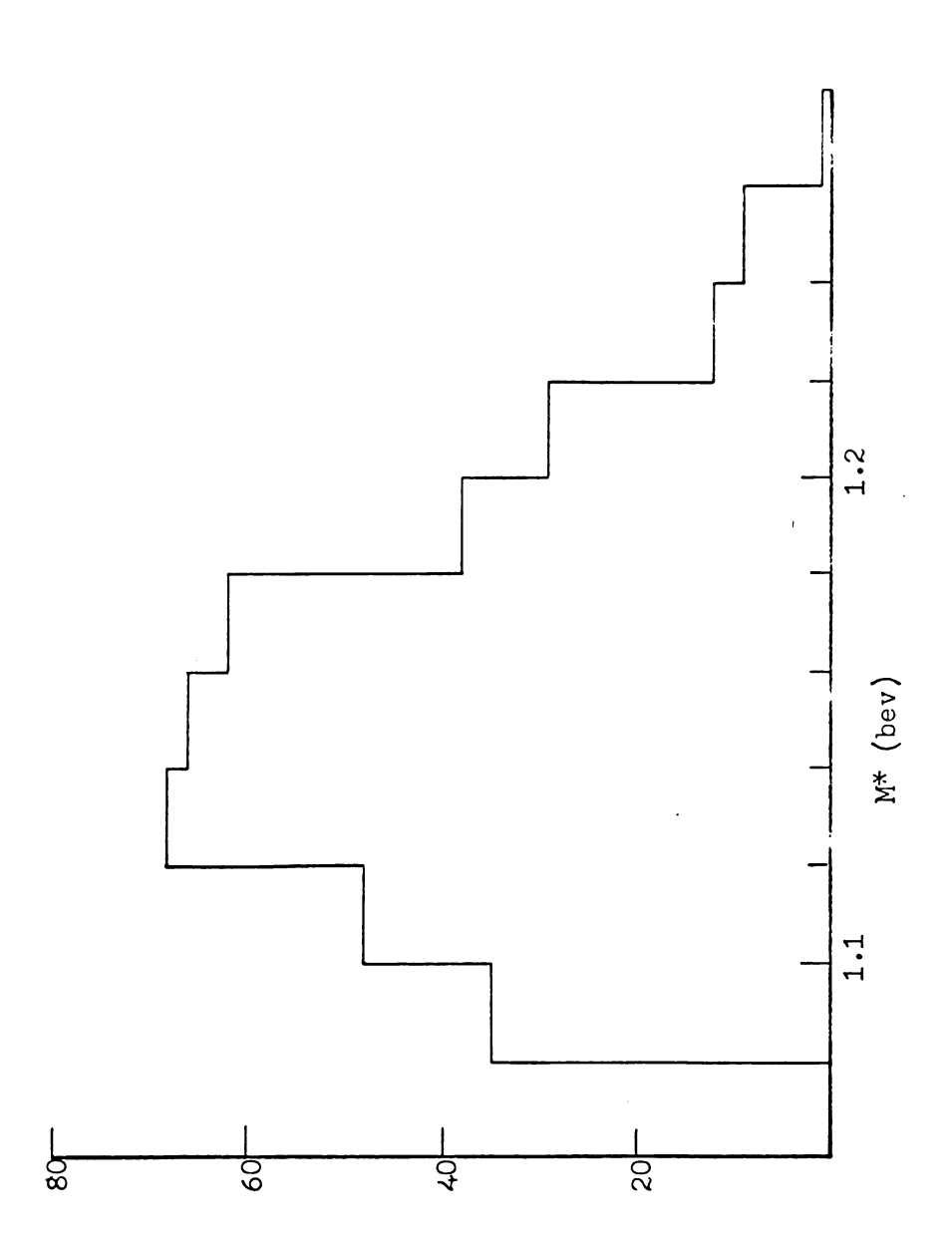


Figure 79. M* of p π and n π combinations: slice 1 of p π π events. 184 pn $^{+}\pi^{-}$ events with 1.7 < Po < 1.9 bev/c.

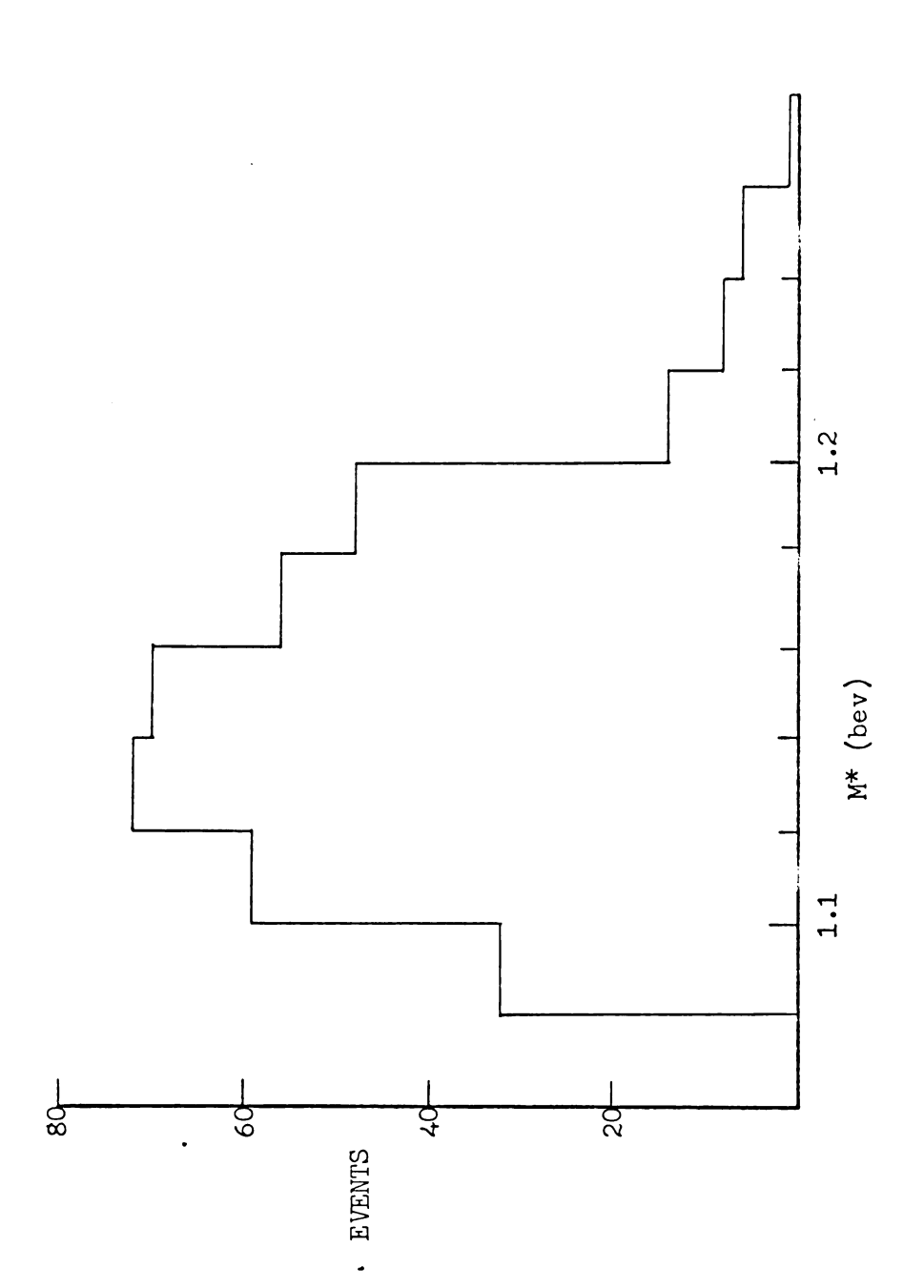


Figure 80. M* of pm and nm combinations: slice 1 of pnm events. $pn^{+}\pi^{-}$ events with 1.7 < P_0 < 1.9 bev/c.

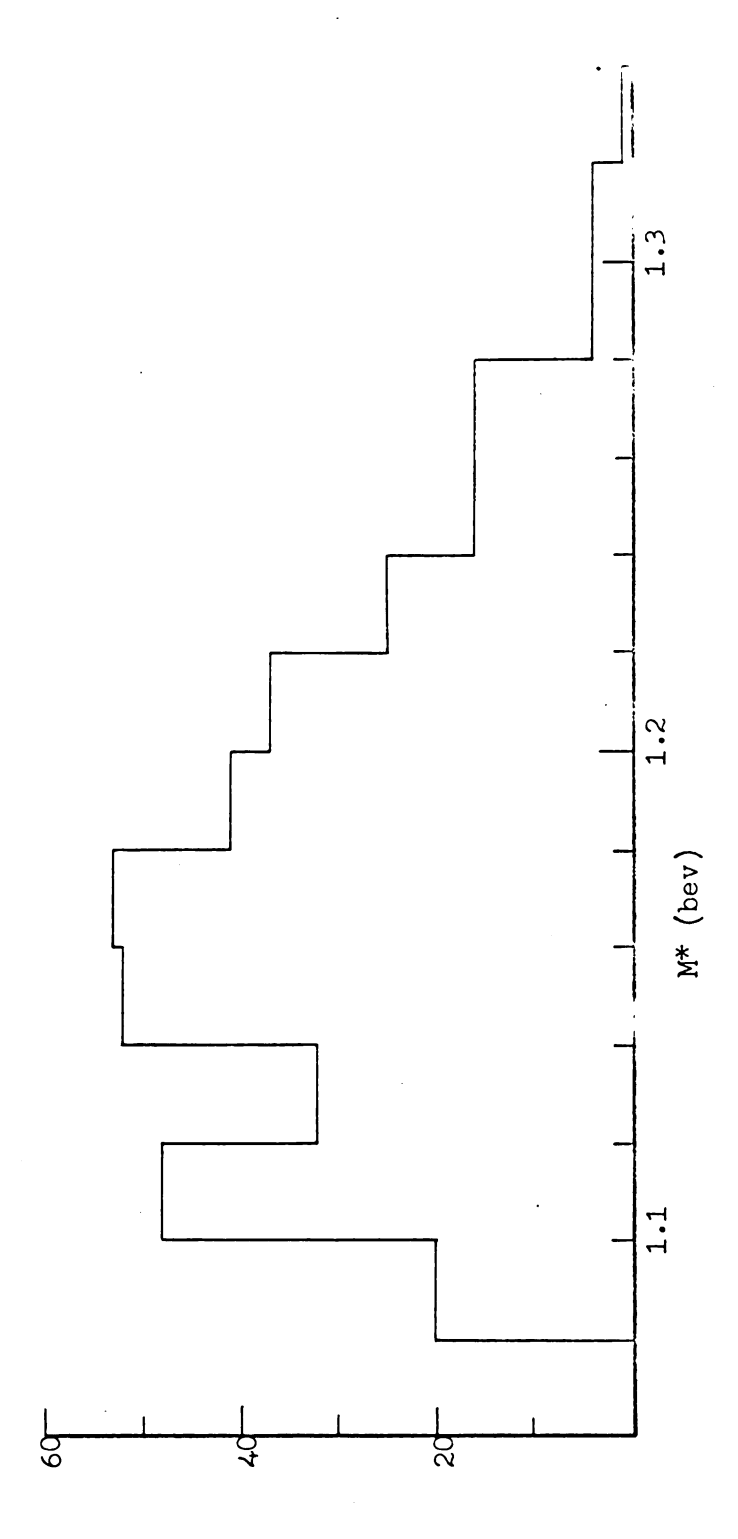


Figure 81. M* of $p\pi^+$ and $n\pi^-$ combinations: slice 2 of $pn\pi^+\pi^-$ events. 174 pn $\pi^{+}\pi^{-}$ events with 1.9 < Po < 2.1 bev/c.

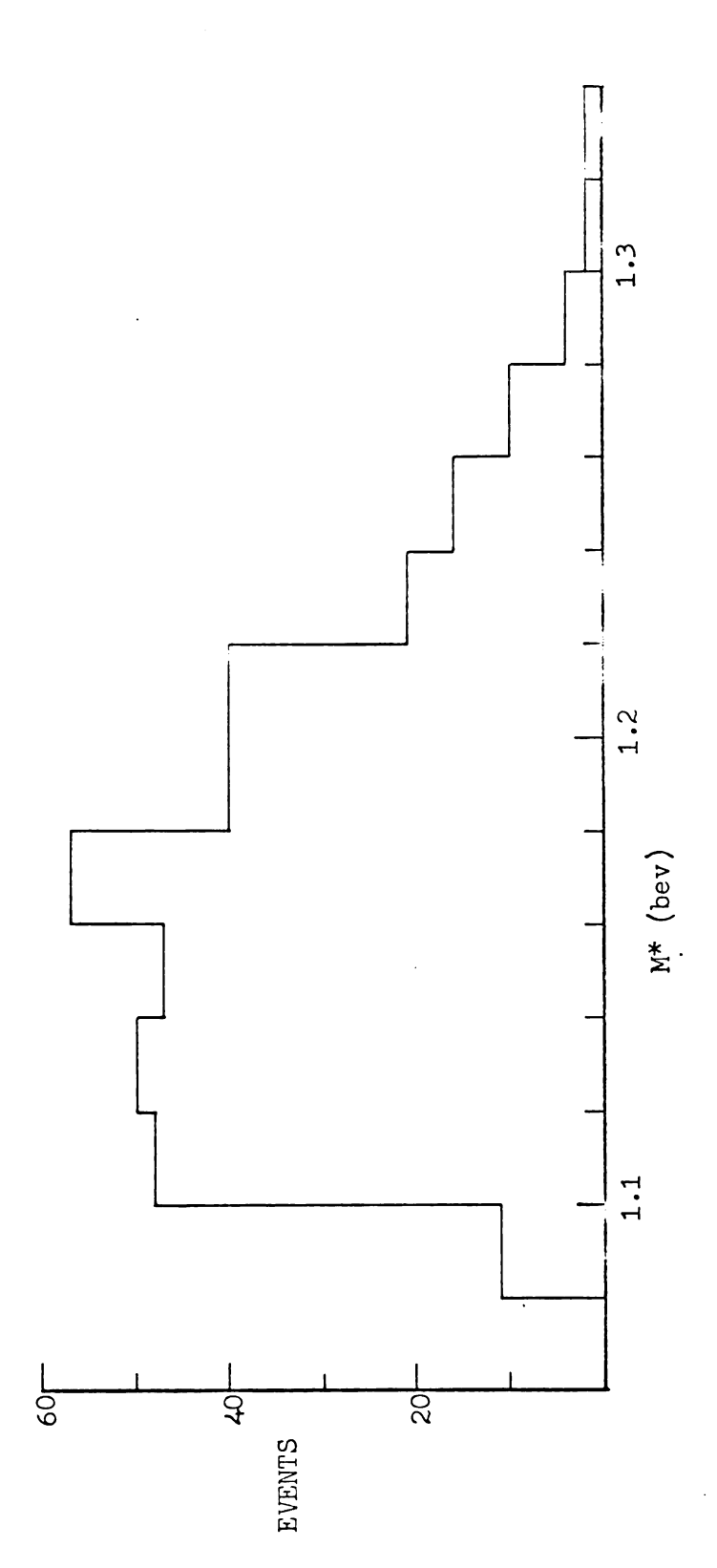


Figure 82. M* of $p\pi$ and $n\pi$ combinations: slice 2 of $pn\pi$ π events. 174 pn $\pi^{+}\pi^{-}$ events with 1.9 < P₀ < 2.1 bev/c.

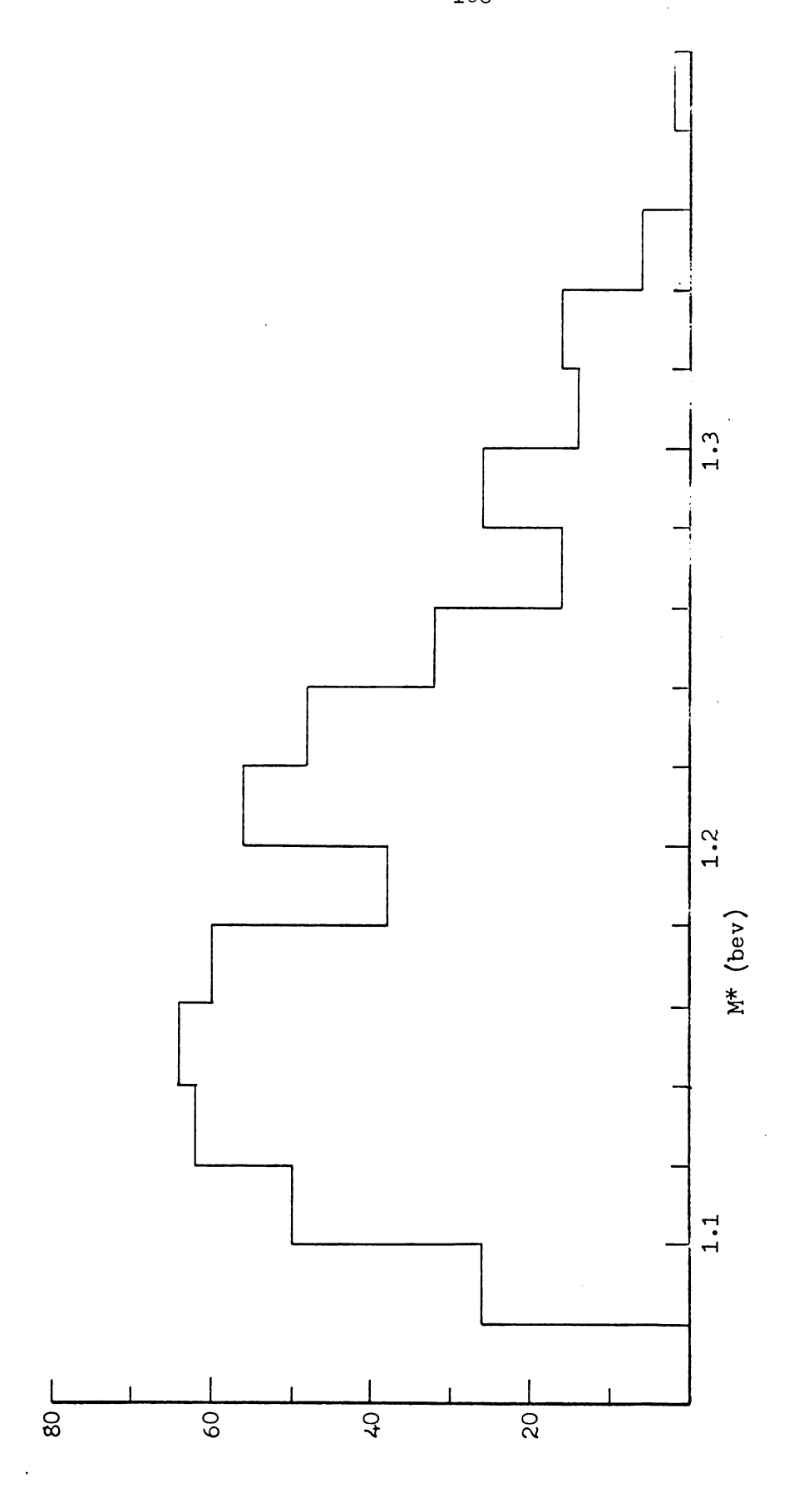


Figure 83. M* of $p\pi^+$ and $n\pi^-$ combinations: slice 3 of $pn\pi^+\pi^-$ events. 128 pn $^{+}\pi^{-}$ events with 2.1 < Po < 2.3 bev/c.



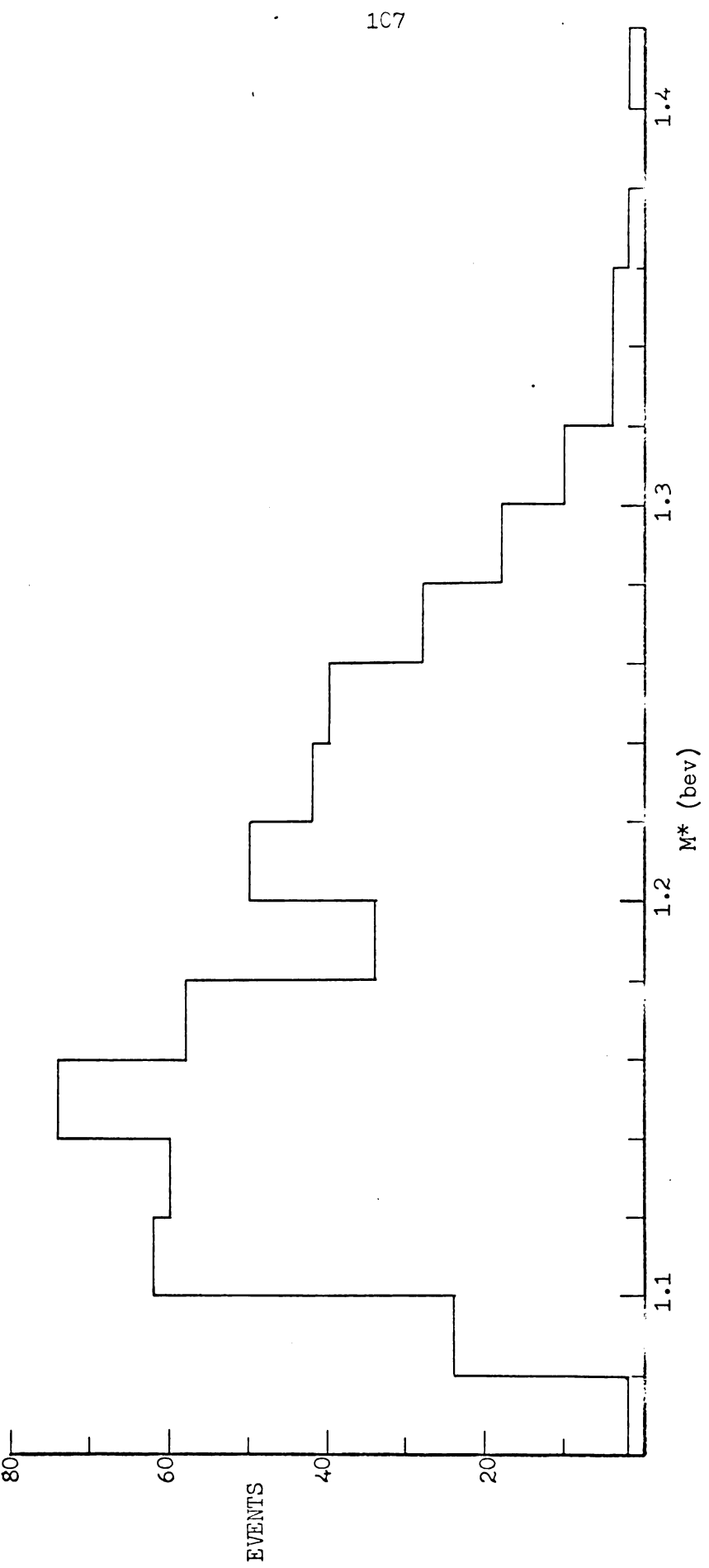


Figure 84. M* of $p\pi^-$ and $n\pi^+$ combinations; slice 3 of $pn\pi^+\pi^-$ events. 128 pn $^{+}\pi^{-}$ events with 2.1 < P₅ < 2.3 bev/c.

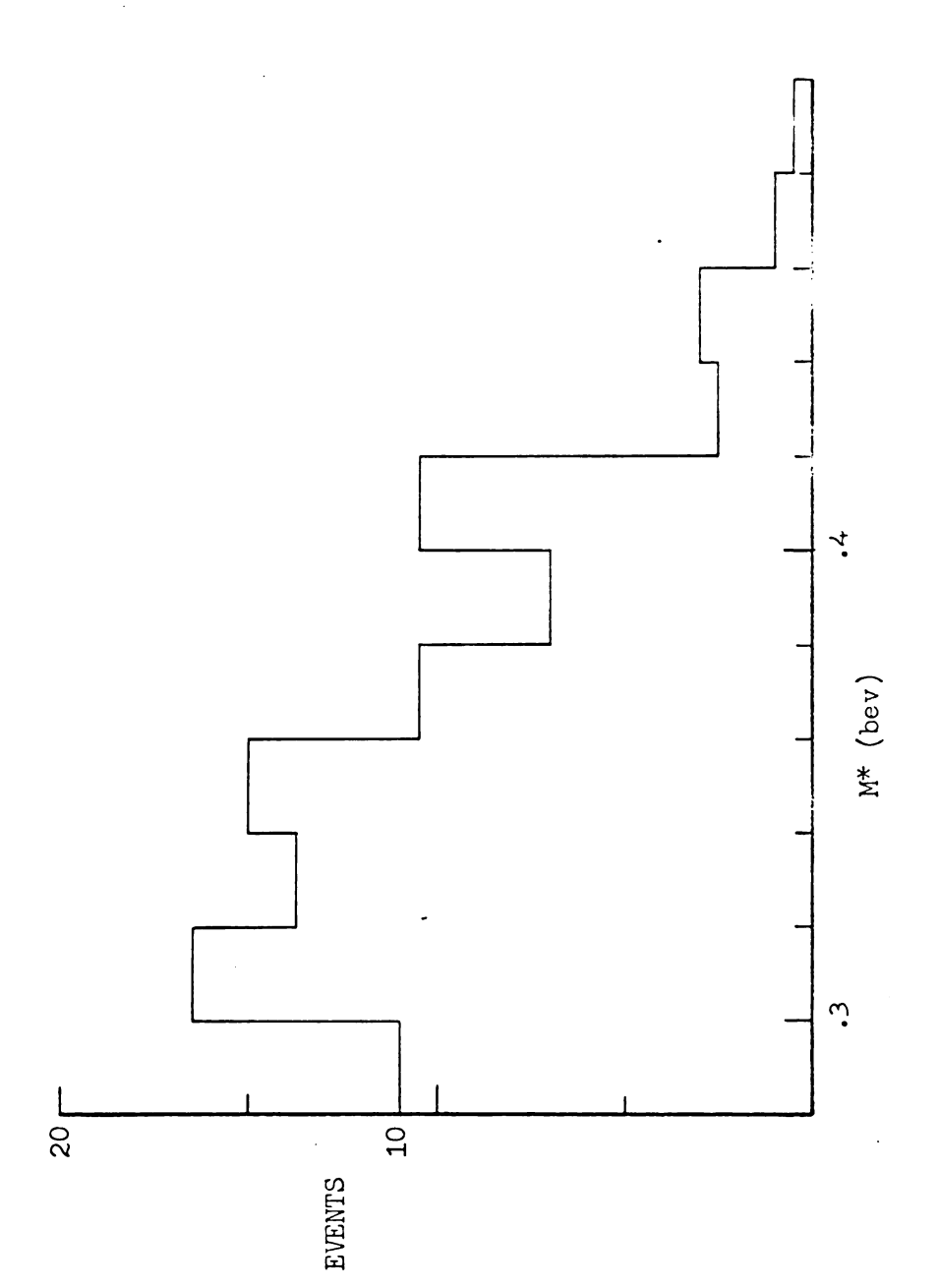


Figure 85. M* of $\pi^+\pi^-$ combination; slice 1 of pn $\pi^+\pi^-$ events. 184 pn $\pi^+\pi^-$ events with 1.7 < Po < 1.9 bev/c.

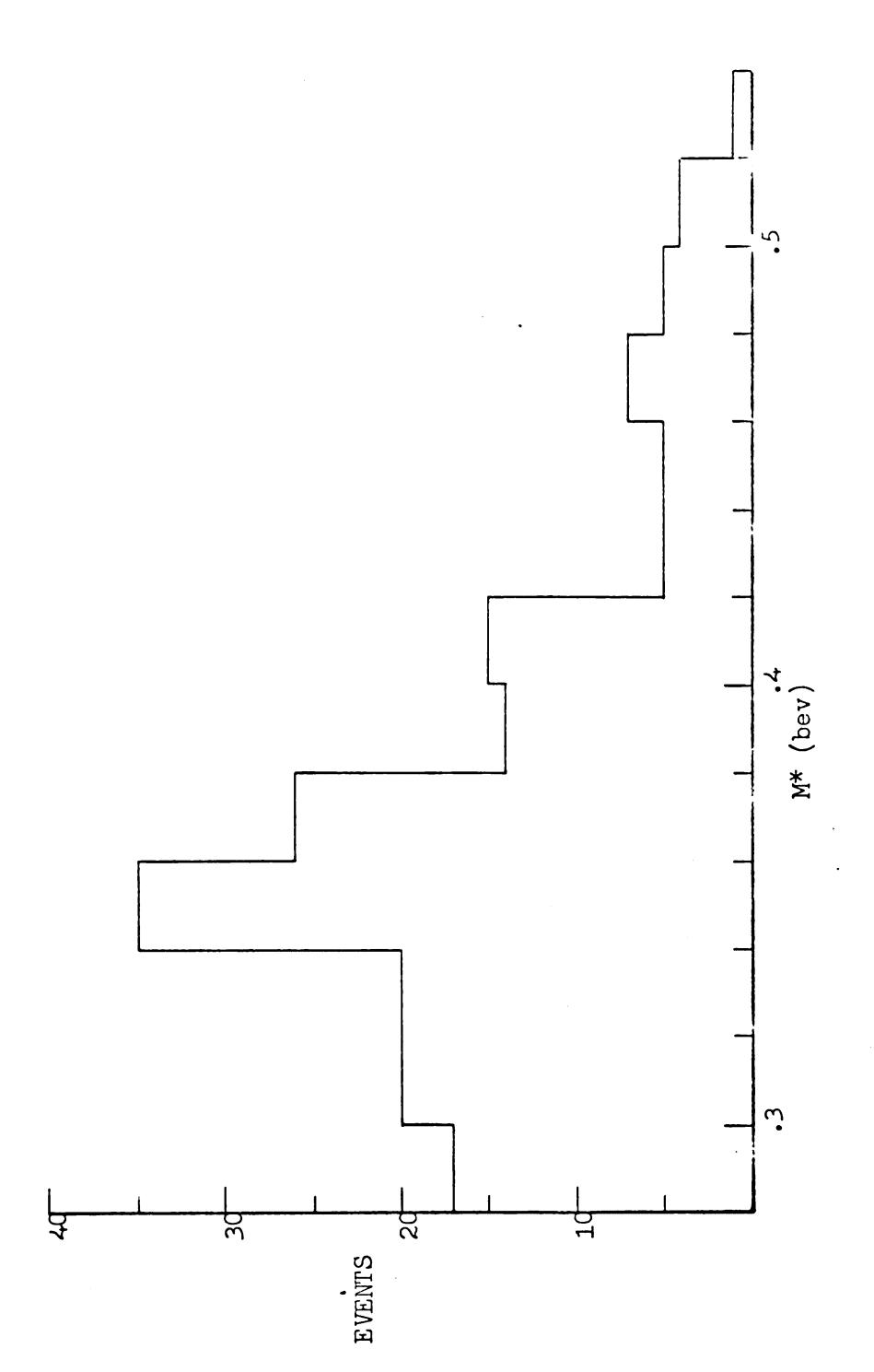


Figure 86. M* of $\pi^{+}\pi^{-}$ combination: slice 2 of pn $\pi^{+}\pi^{-}$ events. 174 pn $^{+}$ π^{-} events with 1.9 < Po < 2.1 bev/c.

		•

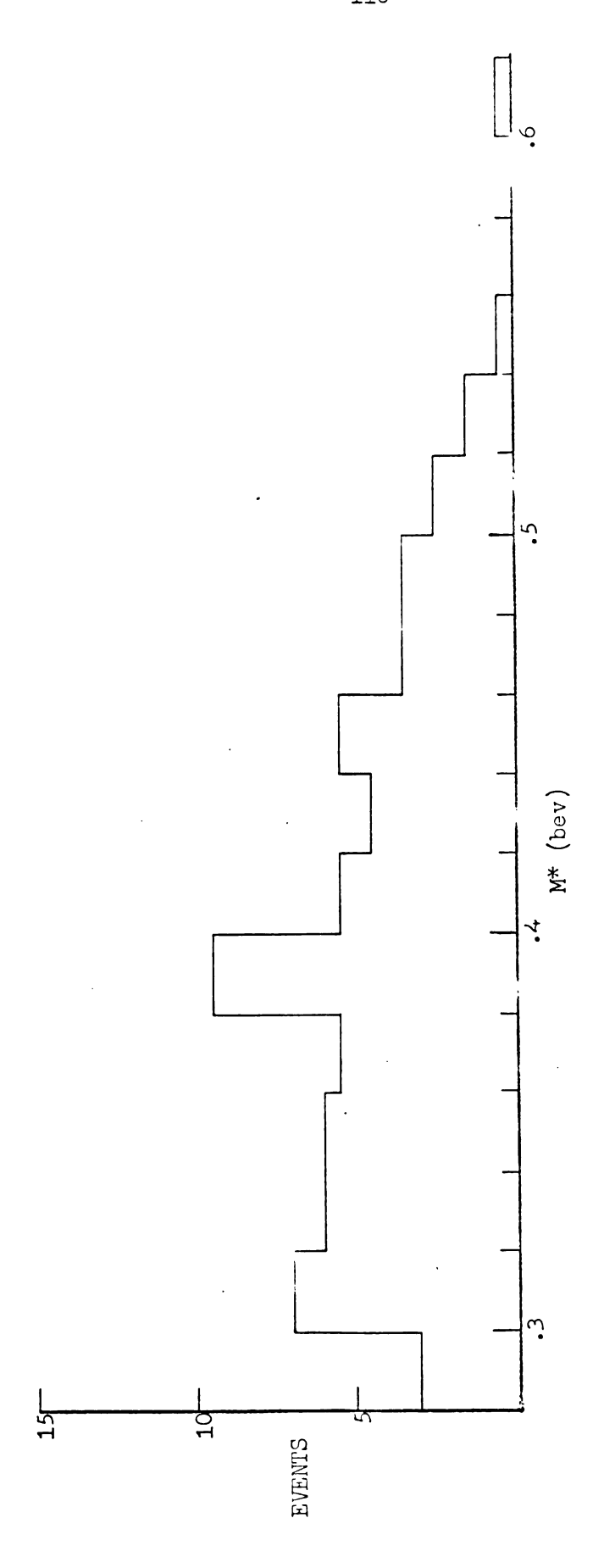


Figure 87. M* of $\pi^+\pi^-$ combination: slice 3 of $\operatorname{pn}\pi^+\pi^-$ events. 128 $\operatorname{pn}\pi^+\pi^-$ events with 2.1 < P₀ < 2.3 bev/c.

	:
	;
	•

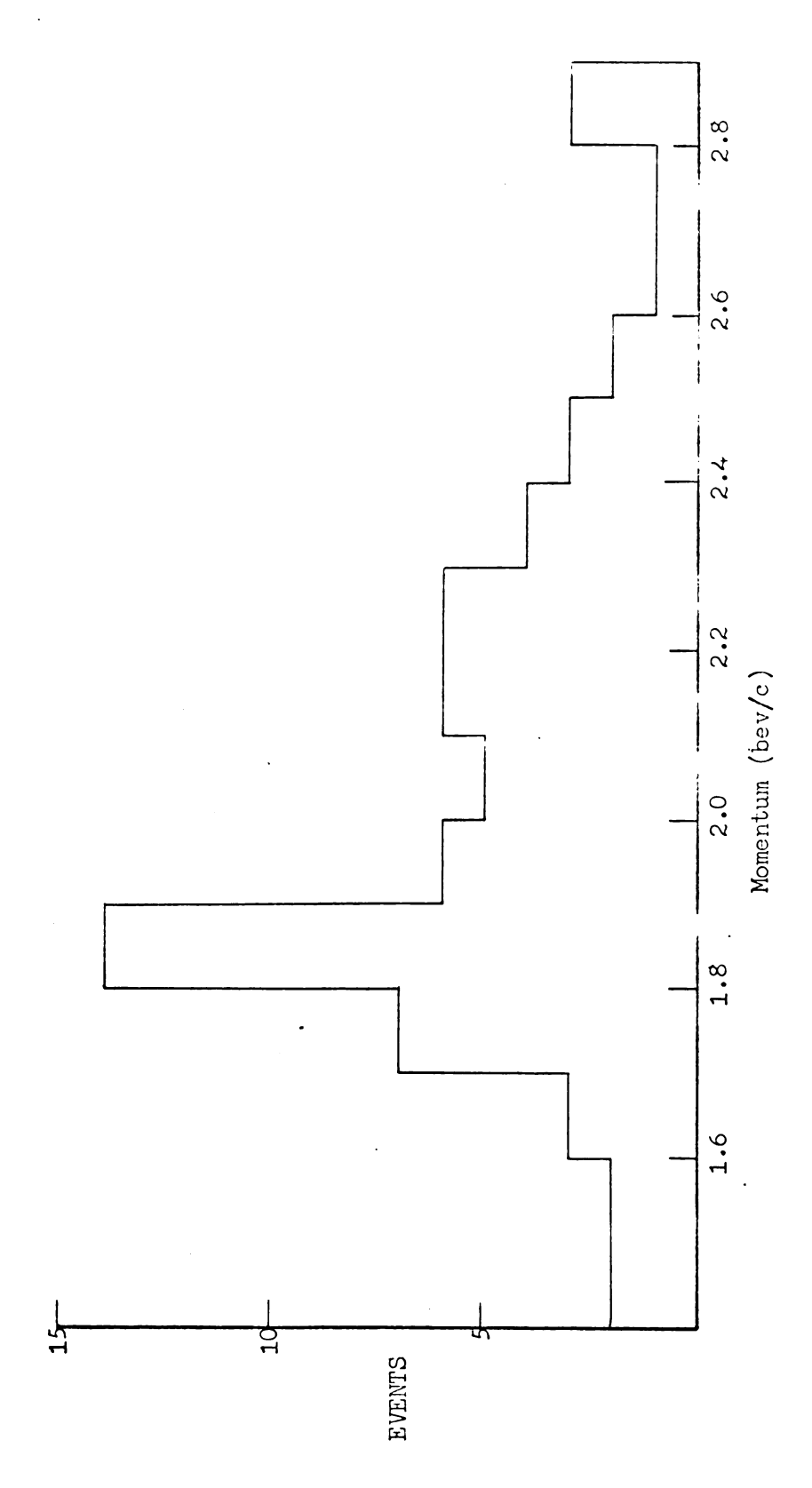


Figure 88. Incident lab neutron momentum of $pp\pi^{n}$ events.

VI. APPENDIX: Description of programs.

A. TRACK FITTING PROGRAM.

The track fitting program calculates momenta, angles, range, coordinates, etc. of up to five tracks per event by fitting five measured points on the tracks in each of three views to a helix whose axis is parallel to the z axis and the magnetic field. The program was designed especially for R. K. Adair's hydrogen bubble chamber which is 14 inches in diameter and 8 inches deep. There are three cameras located on a circle of 13 inches diameter looking perpendicularly at the chamber from a distance of 36.5 inches from the front window. The front window has two fiducial marks on its inside surface ten inches apart and in line with the beam direction. There is a magnetic field in the chamber along the z axis of 17.5 kilogauss.

The input data to the program is on standard I.B.M. punched cards. Data for an event consists of a measurement of the front fiducial marks for a view and measurements of five roughly equally spaced points on each track in the view starting with the origin of the track and ending at the end of the track. This is done for each view. There are identifying numbers in the first columns of each card giving the event number and track and view numbers. This data is read into the computer and reconstructed so that the points are effectively reprojected onto the front window plane. The coordinate system used here has its origin at one of the fiducial marks, the x axis goes through the other front fiducial mark, and the z axis goes from the front window to the back window.

Since the first points measured on a track were at the origin of the track, the points measured were actually corresponding points on the track. The calculation of the xyz coordinates of these corresponding points is a simple matter. Refer to figure A1. The equations for the x, y, and z coordinates of the point are:

$$x - (U_1 - A_1) z/D = U_1$$

 $y - (V_1 - B_1) z/D = V_1$
 $x - (U_2 - A_2) z/D = U_2$
 $y - (V_2 - B_2) z/D = V_2$
 $x - (U_3 - A_3) z/D = U_3$
 $y - (V_3 - B_3) z/D = V_3$.

,

These are six equations for the three unknowns x, y, and z. To combine these by the method of least squares, multiply each term of each equation by its coeficient of x and add the six equations together. Repeat this with the coeficients of y and then z to obtain the three equations:

$$3x - \sum_{i=1}^{3} (u_i - A_i) z/D = \sum_{i=1}^{3} u_i$$

$$3y - \sum_{i=1}^{3} (V_i - B_i) Z/D = \sum_{i=1}^{3} V_i$$

$$\sum_{i=1}^{3} (u_i - A_i) x + \sum_{i=1}^{3} (V_i - B_i) y - \sum_{i=1}^{3} [(u_i - A_i)^2 + (V_i - B_i)^2] \frac{1}{2} \sum_{i=1}^{3} [(u_i - A_i) u_i + (V_i - B_i) V_i]$$

Now dividing each of these equations by 3 the sums reduce to averages, and the result can be expressed more simply as:

$$X - (\overline{u} - \overline{A}) z/D = \overline{u}$$

$$y - (\overline{V} - \overline{B}) z/D = \overline{V}$$

$$(\overline{u} - \overline{A}) \times + (\overline{V} - \overline{B}) y - \left[\overline{(u - A)^2} + \overline{(V - B)^2} \right] z/D$$

$$= \overline{u^2} - \overline{Au} + \overline{V^2} - \overline{BV}$$

where the bars imply averages.

This reduces to:

$$z = D * R$$

 $y = \overline{V} + (\overline{V} - \overline{B}) * R$
 $x = \overline{U} + (\overline{U} - \overline{A}) * R$

where R =
$$\overline{\underline{A}*\overline{U}} - \overline{\underline{A}} * \overline{\underline{U}} + \overline{\underline{B}*\overline{V}} - \overline{\underline{B}} * \overline{\underline{V}} + \overline{\underline{U}}^2 - \overline{\underline{U}^2} + \overline{\underline{V}}^2 - \overline{\underline{V}^2}$$

$$\overline{(\underline{A} - \underline{U})^2} - (\overline{\underline{A}} - \overline{\underline{U}})^2 + (\underline{B} - \underline{V})^2 - (\overline{\underline{B}} - \overline{\underline{V}})^2$$

Having obtained the coordinates of the origin of the track we go about finding the coordinates of the last point measured. Since corresponding points were not measured for the last point we have to interpolate along the track as measured in two of the views in order to find corresponding points. The slopes of the tracks in the x-y plane are tested to see which view pairs are most favorable for this interpolating. Circles are fitted through the last three points in two of the views, and the intersections of these circles and a line parallel to the positions of the camera axes going through the final point of the third view are taken as points corresponding to the point in the third view. Now having corresponding points for the end of the track the same procedure as above may be applied to obtain xyz coordinates of the endpoint.

Now these two points will define a family of helixes with axes parallel to the z axis. If the projection of the helix representing the track is found, then the helix is determined. Coordinates are rotated to a system such that the origin of the track lies at the origin and the endpoint is on the positive x axis. Refer to figure A2. The point d' is found by intersecting the line p1'-p5' and the line parallel to the y axis through p3'. Then projecting from the point A,B through d' down to the x axis we find the point d which is also the x coordinate of the point p3. Finally the line from A,B projected through p3' to the line parallel to the y axis through d intersects at p3 giving both x and y coordinates of p3. This is done for each of the middle points of the track in all views. The result is an array of points closely fitting a circle. By least squares a circle is fit to these points which goes through the endpoints and whose center lies on the perpendicular bisector of the line

segment between the endpoints. This is a one parameter fit. The value of the radius of the circle is then taken as the average of the distances between the center of this circle and the 15 data points. The deviations of these distances from the mean serve as a measure of the accuracy of the fit.

Now knowing the helix which describes the track, the direction cosines of the track are calculated in a straightforward fashion as well as the range of the track in the chamber. In order to obtain the momentum of the track from the radius of the helix and the magnetic field in the chamber, the average value of the magnetic field along the track is obtained by integrating the field along the track. By measurements of the magnetic field without the bubble chamber in place we found that a good representation of the field is:

$$\overline{B} = B_0 + B (z - z_0)^2 - B (r - r_0)^2$$

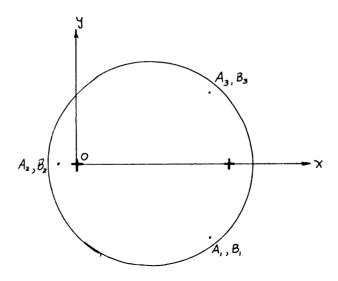
where B_0 = 17.5, B = 0.0062319, B = 0.0035486, z_0 and r_0 are the center of the chamber, and r is the radial position in the chamber. The average magnetic field is obtained by a straightforward integration:

$$\overline{B} = \frac{\int B \cdot ds}{\int ds}$$
 , where ds is an element of path length.

The momentum is then obtained from the well known formula:

$$P = \frac{0.3 * B * R}{\sin \varphi}$$

where φ is the dip angle of the track. Units are mev/c, kilogauss, and centimeters.



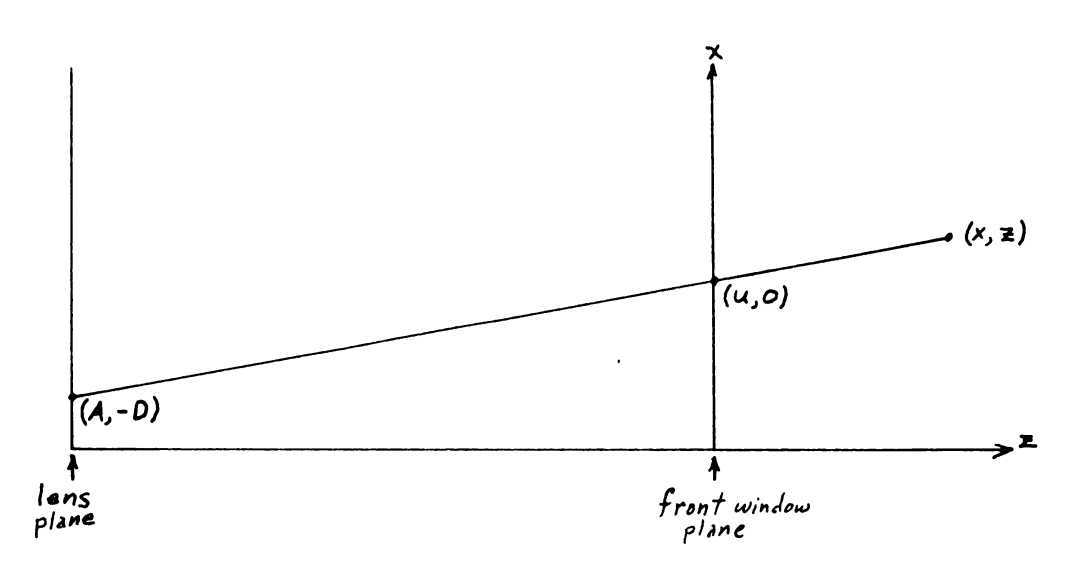


Figure A1. Geometry for finding points in the chamber from measured points. The upper figure represents the arrangement of the cameras with respect to the coordinate system used. Here the z axis is into the page. The lower figure represents the geometry in the x-z plane for relating points in the front window plane to the coordinates of the point in the chamber. A & B are the coordinates of the camera positions, U & V are the coordinates of the measured point as projected onto the front window. D is the effective distance of the camera lenses from the front window. D = $n(d+\delta/n^*)$, where d is the actual air distance between the front glass and the lens, ξ is the total glass thickness, and n and n^* are the indices of refraction of hydrogen and glass respectively.

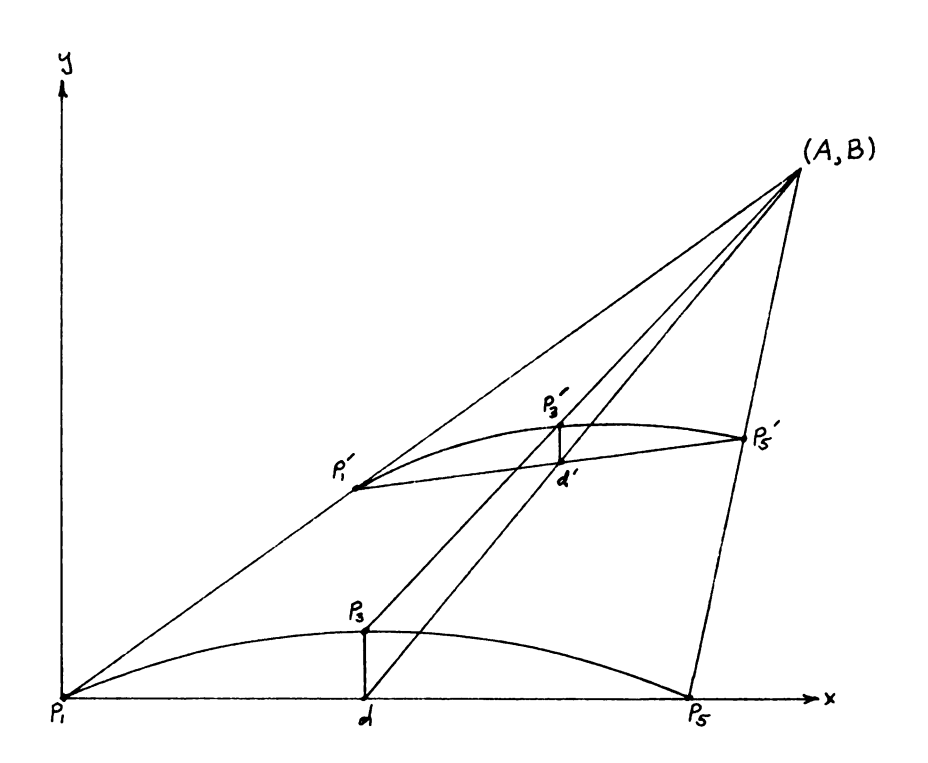


Figure A2. Geometry of the circle fitting proceedure.

The points p₁ and p₅ represent the first and last point of the track in the chamber, while p₁'and p₅' represent the corresponding points from this view as projected onto the front window. Points p₃ and p₃' have the same meaning for some middle point.

B. KINEMATIC TESTING PROGRAM.

The subroutine QEVAL was written to attempt to balance energy and momentum of the events assuming certain mass assingments of the incident and outgoing particles by adjusting the magnitudes of the outgoing momenta without changing the directions. The mass assignments correspond to the possible three body final states of the experiment:

$$n + p \rightarrow p + p + \pi^{-}$$
 $K^{0} + p \rightarrow p + K^{+} + \pi^{-}$
 $K^{0} + p \rightarrow p + \pi^{+} + K^{-}$.

The method is to adjust the outgoing momenta in the best manner to eliminate the unbalance of energy while keeping the chisquare function representing the adjustment of momenta a minimum. In mathematical terms the problem is to minimize chisquare subject to the condition that the change in Q is equal to -Q, where $Q = E_{in} - E_{out}$.

The incident momentum, P_0 , is always equal to the vector sum of the outgoing momenta. Let α, β, δ be the direction cosines of the tracks at the vertex of the event. The apparent unbalance of energy then is given by:

$$Q = \left\{ \left(P_{1} \alpha_{1} + P_{2} \alpha_{2} + P_{3} \alpha_{3} \right)^{2} + \left(P_{1} \beta_{1} + P_{2} \beta_{2} + P_{3} \beta_{3} \right)^{2} + \left(P_{1} \gamma_{1} + P_{2} \gamma_{2} + P_{3} \gamma_{3} \right)^{2} + m_{o}^{2} \right\}^{\frac{1}{2}} + m_{p}$$

$$- \left\{ P_{1}^{2} + m_{1}^{2} \right\}^{\frac{1}{2}} - \left\{ P_{2}^{2} + m_{2}^{2} \right\}^{\frac{1}{2}} - \left\{ P_{3}^{2} + m_{3}^{2} \right\}^{\frac{1}{2}} \right\}$$

The chisquare function we wish to minimize is:

$$\chi^2 = \sum_{i=1}^3 (z_i - z_{oi})^2 / \sigma_{z_i}^2$$

where z = 1/p. z is used rather than p since it is proportional to curvature, not radius of curvature, and should be more normally distributed. The condition on the minimum of chisquare is:

$$dQ = \sum_{i} \frac{\partial Q}{\partial z_{i}} dz_{i} = \sum_{i} \frac{\partial Q}{\partial p_{i}} \frac{dp_{i}}{dz_{i}} dz_{i} = -Q,$$

where

$$\frac{\partial Q}{\partial P_i} = P_{ox} \alpha_i + P_{oy} \beta_i + B_z \delta_i - \frac{P_i}{E_i},$$

and

$$\frac{d\rho_i}{dz_i} = -\rho_i^2 .$$

For simplicity let us represent the equations for X2 and dQ as:

$$\chi^{2} = \sum \beta_{i} x_{i}^{2}$$

$$G = \sum A_{i} x_{i} + Q = 0$$

To minimize X² subject to G, form:

$$\frac{1}{2}d\chi^2 - \lambda dG = 0$$

where λ is an arbitrary constant. This leads to:

$$\sum_{i} (B_{i} x_{i} - \lambda A_{i}) dx_{i} = 0$$
or
$$B_{i} x_{i} - \lambda A_{i} = 0 \quad \text{for all } i.$$

Substitute this result back into G to solve for λ :

$$\lambda \sum_{i} \frac{A_{i}^{2}}{B_{i}} + Q = 0 ,$$
so
$$\lambda = -Q / \sum_{i} A_{i}^{2} / B_{i} ,$$
and
$$X_{j} = \frac{-A_{j}}{B_{j}} \frac{Q}{\sum_{i} A_{i}^{2} / B_{i}} .$$

Now substituting for the x's, A's, and B's we obtain the increments to make in the z's:

$$dz_{i} = -\frac{\sigma_{z_{i}}^{2} \frac{\partial Q}{\partial z_{i}} Q}{\sum_{i} (\sigma_{z_{i}} \frac{\partial Q}{\partial z_{i}})^{2}}$$

The problem was done for each mass assignment in turn. Up to five iterations of the data adjustment were allowed although rarely more than one was necessary. If after an iteration the chisquare function was larger than 7.8 the program stopped further calculation. If the value of Q was made less than 1 mev and the chisquare function was still less than 7.8, the program continued to calculate the momenta, direction cosines, and energies of all tracks in the center of mass of the system.

C. THE PERIPHERAL MODEL PROGRAM.

The theory and development of the equation for the calculations done by the SELLERI program are set down in a paper by E. Ferrari and F. Selleri (21). This report is very comprehensive and the reader is referred to it for a complete discussion of the problem. It contains a brief resume of the status of the peripheral model, some general considerations of S-matrix theory, a thorough discussion of the peripheral S-matrix in particular, as well as the equations for calculation of various cross-sections. The description of the model has already been presented on page 3, and the general equation for the differential cross-section on page 15. The problem is to integrate this equation with respect to the proper variables in order to obtain the spectra desired.

Before discussing the cross-section equations it will be well to review some of the nomenclature of the problem. Referring to figure 1b, the incident particle, p_1 , interacts with a meson, k, in the cloud of the stationary particle, p_2 , which recoils as q_2 . p_1 scatters from k and goes out as particles q_1 and q_3 . The incident particle masses are M_1 and M_2 , the outgoing particle masses are m_1 , m_2 , and m_3 , and the rest mass of the transferred meson k is μ . Some important invariant quantities used in the evaluation are:

$$W^{2} = -(p_{1} + p_{2})^{2}$$

$$\Delta^{2} = (q_{2} - p_{2})^{2}$$

$$t^{2} = (q_{1} - p_{1})^{2}$$

$$\omega^{2} = -(q_{1} + q_{3})^{2}$$

$$u^{2} = -(q_{2} + q_{3})^{2}$$

$$\Delta^{2} = (q_{2} - p_{1})^{2}$$

$$t^{2} = (q_{1} - p_{2})^{2}$$

$$t^{2} = (q_{3} - p_{1})^{2}$$

$$t^{2} = (q_{3} - p_{2})^{2}$$

$$t^{2} = -(q_{1} + q_{2})^{2}$$

Four different coordinate systems are used in the evaluation of certain expressions: the B system is the over-all rest system, the L system is the lab system, the Q system is the rest system of the pair of particles q₁ and q₃, and the P system is the rest system of the pair of particles q₂ and q₃. The evaluation of any variable in one of these systems is indicated by a superscript B, L, Q, or P. q₁, q₂, etc. imply 4-momentum until the energy is used explicitly.

t e t

An additional zero subscript implies the energy of the particle. Hence $\mathbf{q_{20}}^L$ is the energy of the particle $\mathbf{q_2}$ in the lab, and $\mathbf{q_1}^Q$ is the magnitude of the momentum of particle $\mathbf{q_1}$ evaluated in the Q system. Explicit expressions for all kinematic variables are given for each coordinate system as functions of the above invariant quantities and masses, so that one can evaluate the equations with ease.

Ferrari and Selleri have derived the formulas for evaluating the spectra of certain variables pertaining to particles q_1 and q_2 . Starting with the general expression for the cross-section as a function of all final variables, the procedure is to change variables to a set which includes the variable whose spectrum is desired and then integrate over all other variables.

For particle q_2 all the information needed is contained in $\frac{d^2\sigma}{d\Delta^2d\omega^2}$. Quantities like d^3q_2/q_{20} are invariant and can be evaluated in any coordinate system. Let

$$\frac{d^3g_2}{g_{20}} = g_2^B dg_{20}^B d\cos \Theta_2^B d\varphi_2^B.$$

The integral over $d\phi_2^B$ gives 2π for unpolarized initial particles. To make the coordinate transformation $d^3q_2/q_{20} \rightarrow d\Delta^2d\omega^3$:

where the Jacobian

$$J = \frac{1}{4W\rho_1^Bg_2^B} = \frac{1}{4Fg_2^B}.$$

After integrating over the δ -function:

$$\int \frac{d^3g_i \, d^3g_3}{g_{i0} \, g_{30}} \, \delta''(p_g - p_i) \, \longrightarrow \, \int \frac{g_3}{\omega} \, d\omega \, g_i^{\alpha} \, d\varphi_i^{\alpha} \, .$$

Putting these relations into the general differential cross-section:

$$\frac{d^2\sigma}{d\Delta^2 d\omega^2} = \frac{G^2}{8\pi F^2} P_{\perp}^{\alpha} \omega \sigma_{\perp}(\omega) \frac{\Delta^2 + (m_2 - M_2)^2}{(\Delta^2 + \mu^2)^2}.$$

Now to evaluate a particular spectrum there are simple relations for changing variables from Δ^2 or ω^2 to leave the variable of interest. The minimum/maximum value of Δ^2 is given by

In order to evaluate the spectrum of lab kinetic energy, $T_2^{\ L}$ is expressed as a function of Δ^2 in the relation:

$$T_2^L = \frac{1}{2M_2} \left[\Delta^2 + (M_2 - m_2)^2 \right]$$

Then the partial cross-section as a function of T_2^L is:

$$\frac{d\sigma}{dT_{2}^{L}} = 2 M_{2} \frac{d\sigma}{d\Delta^{1}} = \frac{M_{2}G^{2}}{4\pi F^{2}} \frac{\Delta^{2} + (m_{2} - M_{2})^{2}}{(\Delta^{2} + \mu^{2})^{2}} \int_{-\infty}^{\infty} d\omega^{2} \rho_{1}^{\alpha} \omega \sigma_{1}(\omega),$$

$$(m_{1} + m_{3})^{2}$$

where $\omega_{max}^{2}(\Delta^{2})$ is given by:

$$\omega_{max}^{2}(\Delta^{2}) = W^{2} + m_{2}^{2} - \frac{W P_{20}^{B}}{M_{2}^{2}} \left(\Delta^{2} + M_{2}^{2} + m_{2}^{2}\right) + \frac{P_{1}^{B} W}{M_{2}^{2}} \left\{ \left[\Delta^{2} + (m_{1} - M_{2})^{2}\right] \left[\Delta^{2} + (m_{2} + M_{2})^{2}\right] \right\}^{\frac{1}{2}}.$$

To evaluate certain of the variables in these equations two functions are defined:

$$(W, m^2, M^2) = \frac{1}{2W} \left(W^2 + m^2 - M^2 \right)$$

$$P(W, m^2, M^2) = \frac{1}{2W} \left\{ W^4 - 2W^2 (m^2 + M^2) + (m^2 - M^2)^2 \right\}^{\frac{1}{2}}$$

These functions than represent the center of mass energy and 3-momentum of a particle with mass m colliding with a particle of mass M at a total center of mass energy W. The unknown variables above are expressed as:

$$P_{i}^{\mathcal{Q}} = P\left(\omega, M_{i}^{2}, -\Delta^{2}\right)$$

$$P_{2o}^{\mathcal{B}} = E(W, M_{i}^{2}, M_{i}^{2})$$

$$P_{i}^{\mathcal{B}} = P\left(W, M_{i}^{2}, M_{i}^{2}\right)$$

For the center of mass angular distribution $d \Delta^2$ can be transformed to $d\cos\theta_2^{\ B}$ through the relation:

$$\cos \Theta_{2}^{B} = \frac{1}{2 p_{1}^{B} g_{2}^{B}} \left\{ \Delta^{2} + m_{2}^{2} + M_{2}^{2} - 2 p_{20}^{B} g_{20}^{B} \right\}.$$

In this equation all terms except Δ^2 itself are functions of ω^2 alone. Hence $d\Delta^2 = 2p_1^{1B}q_2^{B} d\cos\theta_2^{B}$. Using the relation $F = W \cdot p_1^{B}$ we get:

$$\frac{d\sigma}{d\cos\theta_{1}^{B}} = \frac{G^{2}}{4\pi} \int_{l_{1}}^{l_{2}} d\omega^{2} \int_{l_{1}}^{l_{2}} d\omega^{2} \int_{l_{2}}^{l_{2}} \frac{\Delta^{2} + (m_{2} - M_{1})^{2}}{(\Delta^{2} + \mu^{2})^{2}} \sigma_{l}(\omega),$$

$$(m_{1} + m_{3})^{2}$$

where

$$g_2^B = P(W, m_2^2, \omega^2)$$

The center of mass energy distribution can be obtained from the relation:

In this case the integration over Δ^2 can be carried out analytically:

$$\frac{d\sigma}{dT_{2}^{B}} = \frac{d\sigma}{dg_{20}^{B}} = 2W \frac{d\sigma}{d\omega^{2}} = \frac{G^{2}}{4\pi W p_{1}^{B^{2}}} p_{1}^{B} \omega \sigma_{1}(\omega).$$

$$\cdot \left\{ \log \frac{\Delta_{\max}^{2}(\omega) + \mu^{2}}{\Delta_{\min}^{2}(\omega) + \mu^{2}} - \frac{\left[\mu^{2} - (M_{2} - m_{2})^{2}\right] \left[\Delta_{\max}^{2}(\omega) - \Delta_{\min}^{2}(\omega)\right]}{\left[\Delta_{\max}^{2}(\omega) + \mu^{2}\right] \left[\Delta_{\min}^{2}(\omega) + \mu^{2}\right]} \right\}.$$

The distribution of the invariant mass, ω , and its square, ω^2 , is obtained directly from the expression for the center of mass energy distribution.

For particle q_1 the situation is much more complicated since q_1 is involved in the upper vertex and the cross-section function, σ_1 . All of the information required is present in the expression for $\frac{d^2\sigma}{du^2dt}$. First the expressions linking this partial cross-section with the spectra of interest will be given, and then the evaluation of the partial cross-section will be discussed.

The spectrum of T₁^L is obtained from the relation:

$$T_1^L = \frac{1}{2M_2} \left\{ \bar{\xi}^2 + (M_2 - m_1)^2 \right\}$$
.

$$\frac{d\sigma}{dT_{1}^{2}} = 2M_{2}\frac{d\sigma}{d\bar{t}^{2}} = 2M_{2}\int_{-\infty}^{u_{max}^{2}(\bar{t}^{2})} du^{2}\frac{d^{2}\sigma}{du^{2}dt^{2}},$$

$$(m_{2}+m_{3})^{2}$$

where

$$u_{max}^{2}(\bar{t}^{2}) = W^{2} + m_{1}^{2} - \frac{W \rho_{20}^{8}}{M_{2}^{4}} \left(\bar{t}^{2} + m_{1}^{2} + M_{2}^{2}\right) + \frac{\rho_{1}^{8} W}{M_{2}^{2}} \left\{ \left[\bar{t}^{2} + (m_{1} - M_{2})^{2}\right] \left[\bar{t}^{2} + (m_{1} + M_{2})^{2}\right] \right\}^{\frac{1}{2}}.$$

The angular distribution of $q_{\boldsymbol{1}}$ in the center of mass is obtained from the expression:

$$\cos \theta_{i}^{\beta} = -\frac{1}{2 p_{i}^{\beta} \xi_{i}^{\beta}} \left\{ t^{2} + m_{i}^{2} + M_{i}^{2} - 2 p_{i0}^{\beta} \xi_{i0}^{\beta} \right\}$$

$$\frac{L \sigma}{d \cos \theta_{i}^{\beta}} = 2 p_{i}^{\beta} \int du^{2} \xi_{i}^{\beta} \frac{L^{2} \sigma}{du^{2} dt^{2}}.$$

giving

The center of mass energy distribution of $q_{\boldsymbol{1}}$ is obtained from the expression:

giving
$$\frac{d\sigma}{dT_{i}^{B}} = \frac{d\sigma}{dg_{i0}^{B}} = \frac{2W}{du^{2}} \frac{d\sigma}{du^{2}} = 2W \int_{t_{min}}^{t_{max}^{2}(u)} dt^{2} \frac{d^{2}\sigma}{du^{2}dt^{2}},$$

where

$$t_{\text{max}}^{2}(u) = 2g_{10}^{B} P_{10}^{B} - m_{1}^{2} - M_{1}^{2} + 2g_{1}^{B} P_{1}^{B}$$

$$t_{\text{min}}^{2}(u) = 2g_{10}^{B} P_{10}^{B} - m_{1}^{2} - M_{1}^{2} - 2g_{1}^{B} P_{1}^{B}.$$

Now to evaluate the partial cross-section $\frac{d^2\sigma}{du^idt^i}$ a similar procedure is followed as for $\frac{d^2\sigma}{dx^2du^i}$:

$$\frac{d^{3}g_{1}}{g_{10}} = g_{1}^{\beta} dg_{10}^{\beta} d\cos\theta_{1}^{\beta} d\phi_{1}^{\beta} = \frac{du^{2}dt^{2}}{2F},$$

$$\int \frac{d^3g_2 d^3g_3}{g_{20} g_{30}} \int_{0}^{4} (P_{\mathbf{F}} - P_{\mathbf{i}}) \longrightarrow \frac{g_3}{u} \int d\cos \theta_z^P d\phi_z^P ,$$

and the link between the integration variables and Δ^2 and ω^2 , upon which the integrand essentially depends, must be found. Δ^2 can be expressed as a function of u^2 , t^2 , and $\cos\theta_2^P$ through

For ω^2 , first one connects the angle ϵ_2^P to θ_2^P , and α^P through the trigonometric identity

where ϵ_2^P is the scattering angle of q_2 with respect to p_1 :

and α^{P} is the angle between p_{1} and p_{2} :

These relations can be solved for \triangle^2 and \triangle^2 , and finally ω^2 is obtained from the relation

$$\omega^2 = W^2 - m_2^2 - M_1^2 - M_2^2 - \Delta^2 - \Delta^2$$

Finally putting these quantities into the expression for the partial cross-section we get:

$$\frac{d^2\sigma}{du^2 dt^2} = \frac{1}{8\pi} \frac{G^2}{F^2} \frac{g_3^P}{u} \int_{-1}^{1} l \cos \theta_3^P \frac{\Delta^2 + (m_2 - M_2)^2}{(\Delta^2 + \mu^2)^2} .$$

$$\int_{0}^{2\pi} l \theta_2^P \omega^2 \frac{\rho_1^Q}{\ell_3^Q} \frac{d\sigma_1}{d\Omega} (\omega, \omega s \theta_1^Q) .$$

There are a similar set of equations for the diagram where the incident particle p_1 acts as the spectator and a meson from the cloud of p_1 scatters particle p_2 . They are obtained from the above formulas by interchanging $p_1 \leftrightarrow p_2$, which means also the interchange of barred quantities and unbarred ones, and $M_1 \leftrightarrow M_2$, $\theta_1^P \leftrightarrow \epsilon_1^P$, $\theta_2^Q \leftrightarrow \epsilon_2^Q$. The connection between physical quantities and invariants remains unchanged.

The program is broken into several subroutines, one major one to calculate each of the above mentioned spectra. By appropriate indices punched on one of the data cards, one may call upon any or all of the subroutines to calculate one or more spectra. That is, one may call for the spectra of T2 , T1 from the first diagram or also from the second diagram; four spectra in all. One may also ask for only the first spectrum. T2 L. In addition to the main subroutines there are a few smaller subroutines to calculate certain factors common to all of the equations. One of them $\frac{\Delta^2 + (M_1 - m_1)^2}{(\Delta^2 + M^2)^2}$, another calculates the partial calculates the factor $\frac{d^2\sigma}{du^2dt^2}$, another calculates the function $\frac{d\sigma}{d\Omega}(\omega,\omega^{50})$. cross-section Since these are separate subroutines, it is an easy matter to write different versions of them, as has been done for the partial cross-section σ . We have written one such version which inserts a Breit-Wigner resonance multiplied by an angular dependence factor, and also we have one which interpolates tables of the actual crosssections for the reaction $k + p_1 \rightarrow q_1 + q_3$ containing energy and angular dependence. The values used for this subroutine were obtained from published experimental data.

The integrations are done by Simpson's rule and the number of points in each level of integration is variable. This is done by specifying the number of points in each level by indices on one of the data cards.

REFERENCES

- 1. H. A. Bethe, F. de Hoffmann, <u>Mesons and Fields</u>, Vol. 2, Row, Peterson & Co. (1955).
- 2. A. H. Rosenfield, Phys. Rev. <u>96</u>, 1, 139, (1954). This work contains a review of the information available on pion production from N-N collisions at cyclotron energies.
- 3. A. P. Batson, B. B. Culwick, J. G. Hill, L. Riddiford, Proc. Roy. Soc. 251, 218, (1959).
- 4. G. B. Chadwick, G. B. Collins, C. E. Swartz, A. Roberts, S. DeBenedetti, N. C. Hien, P, J, Duke, Phys. Rev. Letters 4, 12, 611, (1960).
- E. Pickup, D. K. Robinson, E. O. Salant, Phys. Rev. Letters <u>7</u>,
 192, (1961). W. J. Fickinger, E. Pickup, D. K. Robinson,
 O. Salant, Phys. Rev. Letters <u>7</u>, 5, 196, (1961).
- 6. V. Barnes, D. V. Bugg, W. P. Dodd, J. B. Kinson, L. Riddeford, Phys. Rev. Letters 7, 7, 285, (1961).
- 7. G. Da Prato, Nuovo Cim. 22, 1, (1961).
- 8. W. A. Wallenmeyer, Phys. Rev. <u>105</u>, 3, 1058, (1957).
- 9. W. B. Fowler, R. P. Shutt, A. M. Thorndike, W. L. Whittemore, Phys. Rev. <u>95</u>, 4, 1026, (1954).
- 10. F. N. Holmquist, PhD Thesis, Univ. of Cal., Berkeley, UCRL-8559, (1958).
- 11. E. Fermi, Prog. Theor. Phys. (Japan) <u>5</u>, 570, (1950); Phys. Rev. <u>92</u>, 452, (1953); Phys. Rev. <u>93</u>, 1434, (1954); Phys. Rev. <u>81</u>, 683, (1951).
- 12. K. M. Watson, K. A. Brueckner, Phys. Rev. <u>83</u>, 1, 1, (1951);
 Watson, Phys. Rev. <u>86</u>, 6, 852, (1952);
 Brueckner and Watson, Phys. Rev. <u>86</u>, 6, 923, (1952);
 Watson, Phys. Rev. <u>88</u>, 5, 1163, (1952).
- 13. See reference 2 and M. Gell Mann, K. M. Watson, Ann. Rev. Nuclear Science 4, 219, (1954).
- 14. S. J. Lindenbaum, R. M. Sternheimer, Phys. Rev. <u>105</u>, 6, 1874, (1957);
 Phys. Rev. <u>106</u>, 5, 1107, (1957);
 Phys. Rev. <u>109</u>, 5, 1723, (1958);
 Phys. Rev. <u>123</u>, 1, 333, (1061);
 Phys. Rev. Letters <u>5</u>, 1, 24, (1960).

- See references 3, 4, 14, 17, 19, and I. Derado, N. Schmitz, Phys. Rev. <u>118</u>, 1, 309, (1960); V. P. Kenney, W. D. Shephard, C. D. Gall, Phys. Rev. <u>126</u>, 2, 736, (1962); E. L. Hart, R, I, Louttit, D. Leurs, T. W. Morris, W. J. Willis, S. S. Yamamoto, Phys. Rev. <u>126</u>, 2, 747, (1962); W. J. Fickinger, E. Pickup, D. K. Robinson, E. O. Salant, Phys. Rev. <u>125</u>, 6, 2082, (1962), E. Pickup, D. K. Robinson, E. O. Salant, Phys. Rev. <u>125</u>, 6, 2091, (1962).
- 16. E. M. Friedländer, Phys. Rev. Letters 5, 5, 212, (1960).
- 17. I. Derado, Nuovo Cim. 15, 5, 853, (1960).
- 18. G. F. Chew, F. E. Low, Phys. Rev. 113, 6, 1640, (1959).
- 19. F. Bonsignori, F. Selleri, Nuovo Cim. <u>15</u>, 3, 465, (1960).
- 20. F. Selleri, Phys. Rev. Letters <u>6</u>, 2, 64, (1960). E. Ferrari, F. Selleri, Phys. Rev. Letters <u>7</u>, 10, 387, (1961).
- 21. E. Ferrari, F. Selleri, CERN report 2385/TH.227 (1961); CERN report 2845/TH. 243 (1962).
- 22. J. Izuka, A. Klein, Phys. Rev. <u>123</u>, 2, 669, (1961); Prog. Theor. Phys. <u>25</u>, 1018, (1961).
- 23. S. D. Drell, K. Hiidak, Phys. Rev. Letters 7, 5, 199, (1961).
- 24. S. D. Drell, Rev. Mod. Phys. 33, 3, 458, (1961).
- 25. In reference 21 the second report contains an explicit derivation of the problem as well as formulae for the various cross-sections and spectra.
- 26. R. K. Adair, Rev. Mod. Phys. <u>33</u>, 3, 406, (1961).
- 27. H. J. Martin, L. B. Leipuner, W. Chinowsky, F. T. Shively, R. K. Adair, Phys. Rev. Letters 6, 6, 283, (1961).
- 28. For a description of the computer codes see the appendix.
- 29. A. R. Erwin, R. March, W. D. Walker, E. West, Phys. Rev. Letters 6, 11, 628, (1961).
- 30. C. D. Wood, PhD Thesis, Univ. of Cal., Berkeley, UCRL 9507, (1961).
- 31. L. K. Goodwin, R. W. Kenney, V. Perez-Mendez, Phys. Rev. Letters 3, 11, 522, (1959).

-1 116

.

